HAL open science

VMS finite element for MHD and reduced-MHD in Tokamak plasmas

B Nkonga, J Tarcisio-Costa, Jeaniffer Vides

To cite this version:

B Nkonga, J Tarcisio-Costa, Jeaniffer Vides. VMS finite element for MHD and reduced-MHD in Tokamak plasmas. [Research Report] RR-8892, Inria Sophia Antipolis; Université de Nice-Sophia Antipolis. 2016. hal-01294788

HAL Id: hal-01294788

https://inria.hal.science/hal-01294788v1

Submitted on 30 Mar 2016

HAL is a multi-disciplinary open access archive for the deposit and dissemination of scientific research documents, whether they are published or not. The documents may come from teaching and research institutions in France or abroad, or from public or private research centers.

L'archive ouverte pluridisciplinaire **HAL**, est destinée au dépôt et à la diffusion de documents scientifiques de niveau recherche, publiés ou non, émanant des établissements d'enseignement et de recherche français ou étrangers, des laboratoires publics ou privés.

VMS Finite Element for MHD and Reduced-MHD in Tokamak Plasmas

B. Nkonga, J. Tarcisio-Costa , J. Vides

RESEARCH REPORT
N° 8892
2016
Project-Team Castor

ISSN 0249-6399 ISRN INRIA/RR--8892--FR+ENG

VMS Finite Element for MHD and Reduced-MHD in Tokamak Plasmas

B. Nkonga*, J. Tarcisio-Costa *, J. Vides *

Project-Team Castor

Research Report n° 8892 — 2016 — 46 pages

Abstract: The understanding of magnetohydrodynamic (MHD) instabilities is quite essential for the optimization of magnetically confined plasmas, a subject raising increasing interest as tokamak reactor design advances and projects such as ITER (International Thermonuclear Experimental Reactor) develop. Given the need and importance of numerically simulating and studying these instabilities, in this paper we report our effort in developing a stabilized full MHD numerical model to study tokamak plasmas in the frame of the Variational Multi-Scale formulation (VMS). Special attention is given to the plasma equilibrium calculation in limiter and x-point configurations. Several properties of the internal kink instability for a circular geometry were studied, e.g., dependence of the growth rate and mode sizes on the Reynolds Magnetic number and magnetic reconnection. The test cases were compared to other results numerically obtained before, as well as analytical developments. The effects of the VMS stabilization were rigorously verified in order to ensure a numerical stability without supressing the physical instabilities. The validation of this model gives rise to the possibility of simulating Edge-localized modes instabilities in the frame of full MHD equations.

Key-words: Magnetohydrodynamics, Stabilized finite elements, Variational multi-scale stabilization, Implicit time integration, Magnetic vector potential, Internal kink mode, X-point plasmas

* Université de Nice-Sophia Antipolis, UMR CNRS 7351 & Inria Sophia Antipolis - Méditerranée, France

RESEARCH CENTRE
SOPHIA ANTIPOLIS – MÉDITERRANÉE

2004 route des Lucioles - BP 93
06902 Sophia Antipolis Cedex

Résumé : La compréhension des instabilités Magnétohydrodynamiques (MHD) est essentielle pour l'optimisation des plasmas de fusion par confinement magnétique. Ce sujet attire de plus en plus l'intérêt scientifique grâce au progrès des réacteurs tokamaks et le développement des projects tels que ITER (International thermonuclear reactor). Au vu de l'importance d'étudier et de simuler numériquement ces instabilités, dans ce papier nous reportons nos efforts pour développer un modèle numérique de la MHD complète avec stabilisation pour l'étude des plasmas de tokamak dans le cadre de la formulation variationnelle multi-échelles (VMS). Une attention spéciale est donnée au calcul de l'équilibre du plasma pour les configurations dites limiter et point-x. Plusieurs propriétés de l'instabilité de kink interne dans une géométrie circulaire ont été étudiées, par exemple, la dépendance du taux de croissance et de la taille des modes par rapport au nombre de Reynolds Magnétique et la re-connexion magnétique. Les cas-test ont été comparés à d'autres résultats numériques ainsi qu'à des développements analytiques. Les effets de la stabilisation VMS ont été rigoureusement vérifiés pour assurer une stabilité numérique sans supprimer les instabilités physiques. La validation de ce modèle ouvre le chemin pour la possibilité de simuler les instabilités appelées Edge-localized modes (ELMs) dans le contexte de la MHD complète.

Mots-clés : Magnétohydrodynamique, Éléments finis stabilisés, Stabilisation variationnelle multi-échelles, Intégration temporelle implicite, Potentiel vecteur megnétique, Kink interne, Plasmas avec point-X

1 Introduction

It is now commonly accepted that for flows dominated by convection, numerical schemes must take into account the effects of unresolved scales in order to insure stability of the numerical approach. In the context of compressible hydrodynamics, the pioneering work of von Neumann and Richtmyer[40] and its two-dimensional extension by Wilkins [43, 44], unresolved scale effects on large scales are formulated as artificial viscosity. Godunov[19] was the first to introduce an explicit evaluation of sub-scale effects on the resolved scales via the resolution of the so-called Riemann problems. However, these popular formulations are mainly associated to staggered and centered finite volumes (FV) as well as to Discontinous Galerkin (DG) formulations. Moreover, as Riemann problems are defined in the directions normal to the mesh faces, the associated numerical stabilization is highly dependent on the mesh topology. This can be very damaging for flows involving strongly anisotropic processes, as in the high temperature magnetized plasmas. In this context, the high-order Galerkin finite element method (FEM) can provide a useful framework for the numerical approximation as it gives rise to centered approximations of differential operators. This is suitable for elliptic like operators but can lead to unphysical behaviors when flows are dominated by the effect of the hyperbolic operators (convection). Indeed, the Galerkin method does not provide a mechanism for the control of sub-scales effects on the resolved scales, i.e., stabilization.

We are concerned by the numerical modeling of strongly magnetized plasmas in tokamaks geometries, particularly the Magnetohydrodynamic (MHD) instabilities at the edge of the plasma. We assume that the characteristic time scales of the simulations under concern, the interaction of the charged gas with the magnetic field, can be described by the compressible MHD equations. The most popular Galerkin finite element codes for simulation of MHD instabilities on the edge of the tokamak plasma are NIMROD[37], M3D-C1[17] and JOREK[13, 28]. The stabilization process in these codes is achieved either by the use of artificial viscosity or by the introduction of additional self-adjoint operators, sometimes presented as preconditioning, semi-implicit or implicit strategies [22, 32, 30]. The goal is to parabolize the MHD system through an appropriate decomposition of the hyperbolic operator.

The variational multi-scale (VMS) formulation[8, 25, 26] provides attractive guidelines for the development of stabilized schemes that take into account the hyperbolic nature of the considered systems. Within the VMS framework, stabilization of waves is achieved by an additional contribution in the weak formulation. This contribution mimics the effect of the unresolved scales over the resolved scales. The VMS strategy is residual-based and designed to achieve a numerical stability without compromising overall stability and accuracy. By this way, an upwinding process is introduced which leads to numerical diffusion essentially in the flow direction, so as to avoid crosswind diffusion effects for multidimensional flows over non-aligned meshes. The critical point of this strategy is the design of a scaling matrix used to adjust the numerical dissipation such as to preserve the order of accuracy of the Galerkin method. VMS-stabilization is very efficient when dealing with smooth solutions. Nevertheless, this is a linear process and, according to the Godunov's theorem, it can allow oscillatory approximations of discontinuities. Indeed, low-dissipation schemes might result in spurious Gibbs oscillations associated to spectral truncation in the wavenumber space. Thus, although discontinuity capturing is a nonlinear dissipation it is often used to enforce the total variation stability where the solution develops sharp gradients.

Another issue that must be taken into account is related to the solenoidal constraint on the magnetic field. In fact, the divergence free constraint is formulated strongly whereas Finite element methods are based on the weak formulation. In the present case, we will be concerned by MHD instabilities where the initial condition is usually the solution of the so-called Grad-Shafranov (GS) equation on the toroidal component of the potential vector (poloidal magnetic

flux). Therefore, if for the MHD system we use the potential vector formulation, the same variable will be interpolated for the GS equilibrium and the evolution of the perturbed system. However, the magnetic field is not uniquely defined in term of a magnetic vector potential and we need an additional constraint such as the Coulomb gauge. Moreover, the potential formulation can lead to systems with third order derivatives and it can be useful to design finite element functions with continuous gradients over elements (C^1-continuity).

In the present paper, the tokamak geometry (3D) is always the tensor product of a 2D poloidal domain and a periodic 1D toroidal domain i.e., a cylindrical one. Test and trial functions of the finite element strategy are the product of a function of the poloidal coordinates and a function of the toroidal coordinate (the toroidal angle). In the poloidal plane (2D domain) we consider isoparametric C^1-bicubic splines defined on a curved quadrangulation[13]. The bicubic splines have an isoparametric formulation and the elements in the physical space can be curved quadrangles with four degree of freedom per vertex and per physical variable. This strategy is very close to the Hermite approach but with more flexibility of the mesh structuration[13]. The degrees of freedom are associated to the mesh vertices so that we can use compressed numerical graph and block formulation to speed-up computations. In the toroidal direction we need periodical representation functions. Most of the computations are performed with sine-cosine expansions and the use of Hermite cubic splines is also an explored option for the poloidal interpolation.

In the current context, we will propose a VMS stabilization strategy specific for time evolving problems and based on time fluctuations. This approach has some similarities with the Taylor-Galerkin (TG) formulation [15, 16, 3] and can be simplified to recover the parabolizations that are often used for MHD simulations in tokamaks [22, 37, 17, 32, 30]. We will discuss the effect of the potential vector representation of the magnetic field on the weak formulation. The Coulomb gauge conditions as well as the boundary conditions are achieved by penalization, added as contributions to the weak formulation. The time step discretization is mainly the Crank-Nicolson scheme so that the global approximation is implicit and its resolution is achieved by a linearized approximation. The linearized system is solved by the Generalized Minimal RESidual (GMRES) iterative method, preconditioned by direct solvers based on PASTIX software [24] and applied to the sparse sub-systems describing self interaction of Fourier modes. In the context of the reduced MHD, the potential vector is oriented in the toroidal direction and can be defined by a single scalar. Therefore, simplified equations can be derived with the elimination of fast magnetoacoustic waves. In this simplified context, the VMS stabilization is associated to material and slow acoustic waves. These strategies have been included in a tool JOREK dedicated to simulations of MHD instabilities on the edge of tokamak plasmas. The proposed numerical strategy is applied to the simulation of the internal kink mode and the effect of the Bohm boundary conditions on a X-point configuration. The remainder of the paper is organized as follows. Section 2 presents the single fluid model for a magnetized plasma. The numerical approximations and VMS stabilization are the subject of the Section 3. Section 4 proposes simplified stabilizations when reduced MHD models are used. Numerical validations are presented in the section 5 and, finally, section 6 resumes the achievement of the paper and open future perspectives.

2 Single fluid MHD model for tokamak plasmas

The straightforward fluid model that can be derived from the Vlasov equation is obtained by retaining the first three velocity moments of the kinetic equation and the derivation can be performed under the assumption that the distribution function is close to the Maxwellian distribution. This assumption is reasonable when the plasma is dominated by Coulomb collisions

[7]. Unfortunately, most of the tokamak plasmas are strongly magnetized and weakly collisional. Therefore, fluid modeling is sometimes used by default, for its attractiveness in terms of computational resources needed, particularly, for long time simulations in large computational domains, such as simulations of magnetohydrodynamic (MHD) instabilities in tokamaks. In the scrape of layer (SOL) where "Edge-localized mode (ELMs) instabilities" take place, it is acceptable to apply fluid models for numerical computations. Additional assumptions are then used to justify the quasi neutrality and gyro-viscous cancellation. The resulting model is a single fluid system written here in conservative form:

$$\left\{\begin{array}{rcl} \partial_t \rho + \nabla\cdot(\boldsymbol{m}) &=& \nabla\cdot(\underline{\boldsymbol{D}}\nabla\rho)\,, \\ \partial_t \boldsymbol{m} + \nabla\cdot\left(\frac{\boldsymbol{m}\otimes\boldsymbol{m}}{\rho} - \mathbf{B}\otimes\mathbf{B}\right) + \nabla\left(p + \frac{\mathbf{B}\cdot\mathbf{B}}{2}\right) &=& \nabla\cdot\underline{\boldsymbol{\tau}}, \\ \partial_t \mathcal{E} + \nabla\cdot\left(\left(\mathcal{E} + p + \frac{\mathbf{B}\cdot\mathbf{B}}{2}\right)\frac{\boldsymbol{m}}{\rho} - \frac{\mathbf{B}\cdot\boldsymbol{m}}{\rho}\mathbf{B}\right) &=& \nabla\cdot(\boldsymbol{q}) + \nabla\cdot\left(\underline{\boldsymbol{\tau}}\frac{\boldsymbol{m}}{\rho}\right), \\ \partial_t \mathbf{B} + \nabla\cdot\left(\frac{\boldsymbol{m}\otimes\mathbf{B} - \mathbf{B}\otimes\boldsymbol{m}}{\rho}\right) &=& -\nabla\times(\mathbf{E} + \boldsymbol{v}\times\mathbf{B})\,, \end{array}\right. \tag{2.1}$$

where ρ is the density, $\boldsymbol{m} \equiv \rho\boldsymbol{v}$ is the momentum vector, $\mathcal{E}$ is the total energy (hydrodynamic+electromagnetic), $\mathbf{B}$ is the magnetic field vector, p is the hydrodynamic pressure and $\mathbf{E}$ is the electric field. The right-hand sides of the previous equations are related to transport processes: viscosity, conductivity, resistivity. The general closure relations for the transport terms can be found in [7]. The equations of state and the Ohm's law used are

$$\mathcal{E} = \rho\varepsilon + \frac{1}{2\rho}\boldsymbol{m}\cdot\boldsymbol{m} + \frac{1}{2}\mathbf{B}\cdot\mathbf{B}, \quad p = (\gamma-1)\,\rho\varepsilon = \rho T, \quad \mathbf{E} + \boldsymbol{v}\times\mathbf{B} = \underline{\boldsymbol{\eta}}\mathbf{J},$$

where ε is the internal energy, T the temperature, $\mathbf{J} \equiv \nabla\times\mathbf{B}$ the current vector, $\underline{\boldsymbol{\eta}}$ the resistivity (later assumed scalar for simplicity) and $\gamma = 5/3$ the ratio of specific heats. The model described by system (2.1) is essentially driven by the ideal-MHD sub-system found on the left-hand side. This is a conservative system associated to the conservative variables $\boldsymbol{w}$ and the flux tensor $\underline{\mathbf{f}}$

$$\boldsymbol{w} = \begin{pmatrix} \rho \\ \boldsymbol{m} \\ \mathcal{E} \\ \mathbf{B} \end{pmatrix}, \qquad \underline{\mathbf{f}} = \begin{pmatrix} \boldsymbol{m}^{\mathrm{T}} \\ \boldsymbol{v}\otimes\boldsymbol{m} + \mathrm{P}\mathbb{I} - \mathbf{B}\otimes\mathbf{B} \\ \mathcal{H}\boldsymbol{m}^{\mathrm{T}} - (\mathbf{B}\cdot\boldsymbol{v})\,\mathbf{B}^{\mathrm{T}} \\ \boldsymbol{v}\otimes\mathbf{B} - \mathbf{B}\otimes\boldsymbol{v} \end{pmatrix},$$

$\mathrm{P} = p + \frac{\mathbf{B}\cdot\mathbf{B}}{2}$ is the total pressure and $\mathcal{H} = \dfrac{\mathcal{E}+\mathrm{P}}{\rho}$ the enthalpy. The superscript $(.^{\mathrm{T}})$ is used for the transpose of a vector. The ideal-MHD system (when transport is set to zero) is

$$\frac{\partial\boldsymbol{w}}{\partial t} + \nabla\cdot\underline{\mathbf{f}} = 0. \tag{2.2}$$

It is useful to reformulate this system in quasi-linear form as

$$\frac{\partial\boldsymbol{w}}{\partial t} + \underline{\mathbf{L}}(\boldsymbol{w},\boldsymbol{\partial})\,\boldsymbol{w} = 0, \tag{2.3}$$

where the operator $\underline{\mathbf{L}}(\boldsymbol{w},\boldsymbol{\partial})$ is defined by

$$\underline{\mathbf{L}}(\boldsymbol{w},\boldsymbol{\partial}) = \left(\begin{array}{c|c|c|c} 0 & \boldsymbol{\partial}^{\mathrm{T}} & 0 & \mathbf{0}^{\mathrm{T}} \\ \hline -\frac{\boldsymbol{m}}{\rho^2}\boldsymbol{m}\cdot\boldsymbol{\partial} + \frac{\partial\mathrm{P}}{\partial\rho}\boldsymbol{\partial} & \frac{1}{\rho}\boldsymbol{m}\otimes\boldsymbol{\partial} + \frac{1}{\rho}\boldsymbol{m}\cdot\boldsymbol{\partial} + \left(\frac{\partial\mathrm{P}}{\partial\boldsymbol{m}}\otimes\boldsymbol{\partial}\right)^{\mathrm{T}} & \frac{\partial\mathrm{P}}{\partial\mathcal{E}}\boldsymbol{\partial} & \left(\mathbf{B}\otimes\boldsymbol{\partial}\right)^{\mathrm{T}} - \mathbf{B}\cdot\boldsymbol{\partial} + \left(\frac{\partial\mathrm{P}}{\partial\mathbf{B}}\otimes\boldsymbol{\partial}\right)^{\mathrm{T}} \\ \hline \frac{\partial\mathcal{H}}{\partial\rho}\boldsymbol{m}\cdot\boldsymbol{\partial} + \frac{\mathbf{B}\cdot\boldsymbol{m}}{\rho^2}\mathbf{B}\cdot\boldsymbol{\partial} & \left(\frac{\partial\mathcal{H}}{\partial\boldsymbol{m}}\right)^{\mathrm{T}}\boldsymbol{m}\cdot\boldsymbol{\partial} + \mathcal{H}\boldsymbol{\partial}^{\mathrm{T}} - \frac{\mathbf{B}^{\mathrm{T}}}{\rho}\mathbf{B}\cdot\boldsymbol{\partial} & \frac{\partial\mathcal{H}}{\partial\mathcal{E}}\boldsymbol{m}\cdot\boldsymbol{\partial} & \frac{\partial\mathcal{H}}{\partial\mathbf{B}}^{\mathrm{T}}\boldsymbol{m}\cdot\boldsymbol{\partial} - \frac{\mathbf{B}\cdot\boldsymbol{m}}{\rho}\boldsymbol{\partial}^{\mathrm{T}} - \frac{\boldsymbol{m}^{\mathrm{T}}\mathbf{B}\cdot\boldsymbol{\partial}}{\rho} \\ \hline -\frac{\mathbf{B}\boldsymbol{m}\cdot\boldsymbol{\partial} - \boldsymbol{m}\mathbf{B}\cdot\boldsymbol{\partial}}{\rho^2} & \frac{\mathbf{B}\otimes\boldsymbol{\partial} - \mathbf{B}\cdot\boldsymbol{\partial}}{\rho} & \mathbf{0} & \frac{\boldsymbol{m}\cdot\boldsymbol{\partial} - \boldsymbol{m}\boldsymbol{\partial}^{\mathrm{T}}}{\rho} \end{array}\right).$$

For any direction $\boldsymbol{n}$, $\underline{\mathbf{L}}(\boldsymbol{w},\boldsymbol{n})$ is a matrix with eigenvalues associated to advection $(\boldsymbol{v}\cdot\boldsymbol{n})$, to Alfven $(\boldsymbol{v}\cdot\boldsymbol{n}\pm c_a)$, to fast acoustic $(\boldsymbol{v}\cdot\boldsymbol{n}\pm c_f)$ and to slow acoustic $(\boldsymbol{v}\cdot\boldsymbol{n}\pm c_s)$ waves, where

$$c_a^2=\frac{(\mathbf{B}\cdot\boldsymbol{n})^2}{\rho},\quad c_f^2=\frac{1}{2}\left(c^2+\frac{\mathbf{B}\cdot\mathbf{B}}{\rho}+\sqrt{\left(c^2+\frac{\mathbf{B}\cdot\mathbf{B}}{\rho}\right)^2-4c^2\frac{(\mathbf{B}\cdot\boldsymbol{n})^2}{\rho}}\right),$$

$$c^2=\frac{\gamma p}{\rho},\quad c_s^2=\frac{1}{2}\left(c^2+\frac{\mathbf{B}\cdot\mathbf{B}}{\rho}-\sqrt{\left(c^2+\frac{\mathbf{B}\cdot\mathbf{B}}{\rho}\right)^2-4c^2\frac{(\mathbf{B}\cdot\boldsymbol{n})^2}{\rho}}\right).$$

Hence, the ideal-MHD is, in general, a weakly hyperbolic system. Therefore, any finite element approximation of this system needs additional treatment to control the spurious wave effects of the unresolved scales on the resolved ones [27, 18, 39, 11, 34].

3 VMS-Stabilization and numerical strategy.

We can use the residual to reformulate the system (2.1) as $\mathbf{R}(\boldsymbol{w})=0$, where the residual $\mathbf{R}(\boldsymbol{w})$ is defined as

$$\mathbf{R}(\boldsymbol{w}):=\frac{\partial\boldsymbol{w}}{\partial t}+\nabla\cdot\underline{\mathbf{f}}-\nabla\cdot\underline{\mathbf{g}},\tag{3.1}$$

with $\underline{\mathbf{g}}$ the tensor modeling the transport process. Therefore, the weak formulation for a space domain $\boldsymbol{\Omega}_{x,h}$, can be written as

$$\int_{\boldsymbol{\Omega}_{x,h}}\mathbf{R}(\boldsymbol{w})\cdot\boldsymbol{w}^\star=0,\quad\forall\boldsymbol{w}^\star\in\vec{\boldsymbol{\mathcal{W}}}_{\boldsymbol{h}}(\boldsymbol{\Omega}_{x,h}).\tag{3.2}$$

The construction of the finite element space $\vec{\boldsymbol{\mathcal{W}}}_{\boldsymbol{h}}(\boldsymbol{\Omega}_{x,h})$ will be investigated later. The simple formulation (3.2) is not satisfactory in the present context, for at least two reasons. First the MHD system is subjected to a divergence free constraint on the magnetic field and this is not directly included in the previous formulation, even if the construction of the approximation space can be achieved such as to include this constraint. The second reason is that the considered plasma flows are convection dominated and as the formulation (3.2) is in general not upwinded, it will develop spurious waves.

Potential vector formulation. One of the solutions for the first point above could be the construction of an appropriate finite element space. However, it is not the option explored here, the main reason being that, beyond the practical issues related to divergence and curl-conforming elements, simulations of MHD instabilities inside tokamaks start from a so called Grad-Shafranov equilibrium [21, 35] which is an equation for the magnetic flux. This variable is the toroidal component of the potential vector. Hence, it is natural to introduce a potential vector $\mathbf{A}$ and derive the magnetic field by the curl $\mathbf{B}=\nabla\times\mathbf{A}$ so that, in principle, there are no magnetic monopoles, in other words, so that $\nabla\cdot\mathbf{B}=0$ is satisfied. Note that the formulation of the magnetic field with the potential vector does not change if we add a gradient of any function to the potential. Indeed, the curl of a gradient is always zero i.e, the magnetic field is invariant under the so-called "Gauge transformation". Therefore, the potential vector is not uniquely defined and this is a tricky situation in computations subjected to numerical overflow. Indeed, according to the Helmholtz theorem, the uniqueness of the potential vector field will be achieved if both the curl and the divergence are fixed. The curl of the potential vector is the magnetic field, thus we also need to fix the divergence in order to enforce the uniqueness. The Coulomb gauge

condition simply sets the divergence to zero $\nabla \cdot \mathbf{A} = 0$. This condition is applied here under a penalized weak form (over the computational domain) defined with $(\nabla \cdot \mathbf{A}) \cdot (\nabla \cdot \mathbf{A}^\star)$. This penalty is activated when the approximated space for $\mathbf{A}$ is not divergence free. This approximation space is spanned by the test functions $\mathbf{A}^\star$.

VMS-Stabilization. The solution to the second problem related to the formulation (3.2) is to use one of the VMS-stabilization strategies proposed by Hughes and collaborators [26, 27, 33]. In this framework of the variational multiscale formulation, scales decompositions are used to derive a modified weak form including the contributions of the unresolved scales. Assuming that the main operator to be stabilized is $\underline{\mathbf{L}}(\boldsymbol{w}, \boldsymbol{\partial})$, the stabilized weak formulation can be simply written as

$$\int_{\boldsymbol{\Omega}_{x,h}} \mathbf{R}(\boldsymbol{w}) \cdot \boldsymbol{w}^\star + \int_{\boldsymbol{\Omega}_{x,h}} \boldsymbol{w}' \cdot \left(\underline{\mathbf{L}}^{\mathrm{T}}(\boldsymbol{w}, \boldsymbol{\partial})\, \boldsymbol{w}^\star\right) = 0, \quad \forall \boldsymbol{w}^\star \in \vec{\boldsymbol{\mathcal{W}}}_{\boldsymbol{h}}(\boldsymbol{\Omega}_{x,h}), \tag{3.3}$$

where $\boldsymbol{w}'$ is the vector of the sub-scales and $\underline{\mathbf{L}}^{\mathrm{T}}(\boldsymbol{w}, \boldsymbol{\partial})$ is the adjoint of $\underline{\mathbf{L}}(\boldsymbol{w}, \boldsymbol{\partial})$. Notice that the streamline-upwind/Petrov-Galerkin (SUPG) strategy uses the operator $\underline{\mathbf{L}}$ in the place where the VMS approach uses the adjoint.

$$\underline{\mathbf{L}}^{\mathrm{T}}(\boldsymbol{w}, \boldsymbol{\partial}) = \left(\begin{array}{c|c|c|c}
0 & -\frac{\boldsymbol{m}^{\mathrm{T}}}{\rho^2}\boldsymbol{m}\cdot\boldsymbol{\partial} + \frac{\partial \mathrm{P}}{\partial \rho}\boldsymbol{\partial}^{\mathrm{T}} & \frac{\partial \mathcal{H}}{\partial \rho}\boldsymbol{m}\cdot\boldsymbol{\partial} + \frac{\mathbf{B}\cdot\boldsymbol{m}}{\rho^2}\mathbf{B}\cdot\boldsymbol{\partial} & -\frac{\mathbf{B}^{\mathrm{T}}\boldsymbol{m}\cdot\boldsymbol{\partial} - \boldsymbol{m}^{\mathrm{T}}\mathbf{B}\cdot\boldsymbol{\partial}}{\rho^2} \\
\hline
\boldsymbol{\partial} & \begin{array}{r}\frac{1}{\rho}(\boldsymbol{m}\otimes\boldsymbol{\partial})^{\mathrm{T}} + \frac{1}{\rho}\boldsymbol{m}\cdot\boldsymbol{\partial} \\ + \frac{\partial \mathrm{P}}{\partial \boldsymbol{m}}\otimes\boldsymbol{\partial}\end{array} & \frac{\partial \mathcal{H}}{\partial \boldsymbol{m}}\boldsymbol{m}\cdot\boldsymbol{\partial} + \mathcal{H}\boldsymbol{\partial} - \frac{\mathbf{B}}{\rho}\mathbf{B}\cdot\boldsymbol{\partial} & \frac{(\mathbf{B}\otimes\boldsymbol{\partial})^{\mathrm{T}} - \mathbf{B}\cdot\boldsymbol{\partial}}{\rho} \\
\hline
0 & \frac{\partial \mathrm{P}}{\partial \mathcal{E}}\boldsymbol{\partial}^{\mathrm{T}} & \frac{\partial \mathcal{H}}{\partial \mathcal{E}}\boldsymbol{m}\cdot\boldsymbol{\partial} & \mathbf{0}^{\mathrm{T}} \\
\hline
\mathbf{0} & \frac{\partial \mathrm{P}}{\partial \mathbf{B}}\otimes\boldsymbol{\partial} + \mathbf{B}\otimes\boldsymbol{\partial} - \mathbf{B}\cdot\boldsymbol{\partial} & \frac{\partial \mathcal{H}}{\partial \mathbf{B}}\boldsymbol{m}\cdot\boldsymbol{\partial} - \frac{\mathbf{B}\cdot\boldsymbol{m}}{\rho}\boldsymbol{\partial} - \frac{\boldsymbol{m}\mathbf{B}\cdot\boldsymbol{\partial}}{\rho} & \frac{\boldsymbol{m}\cdot\boldsymbol{\partial} - (\boldsymbol{m}\otimes\boldsymbol{\partial})^{\mathrm{T}}}{\rho}
\end{array}\right).$$

Formally, the small scales problem gives $\boldsymbol{w}' = -\left(\underline{\mathbf{L}}(\boldsymbol{w}, \boldsymbol{\partial})\right)^{-1}\mathbf{R}(\boldsymbol{w})$ which is not always simple to invert and algebraic formulations are often used via the introduction of the "intrinsic time-scale" stabilization matrix $\underline{\boldsymbol{\mathcal{T}}}$. The applications under concern are MHD instabilities (instationary). Hence, we propose to use a modified algebraic closure where the subscales are related to the advection of time fluctuations of the state $\boldsymbol{w}$:

$$\boldsymbol{w}' \simeq \underline{\boldsymbol{\mathcal{T}}}\left(\underline{\mathbf{L}}(\boldsymbol{w}, \boldsymbol{\partial})\, \delta\boldsymbol{w}\right). \tag{3.4}$$

We will later make some connections between the stabilization associated to this closure and preconditioning strategies very often used in the fusion plasma community. A very simple analysis shows, for usual VMS approaches, that the matrix $\underline{\boldsymbol{\mathcal{T}}}$ satisfies the scaling estimation in matrix norm:

$$\|\underline{\mathbf{L}}(\boldsymbol{w}, \boldsymbol{\partial})\|_\infty \|\underline{\boldsymbol{\mathcal{T}}}\|_\infty \simeq 1,$$

so that we can set the stabilization matrix to $\underline{\boldsymbol{\mathcal{T}}} \simeq \left(\underline{\mathbf{L}}(\boldsymbol{w}, \boldsymbol{\partial})\right)^{-1}$. However, this is only a formal definition that is difficult to use in practice. This is why the derivation of the stabilization matrix $\underline{\boldsymbol{\mathcal{T}}}$ has been a subject of extensive research over the last decades.

Options for the stabilization matrix $\underline{\boldsymbol{\mathcal{T}}}$. Up to now, the definitions of $\underline{\boldsymbol{\mathcal{T}}}$ mostly rely on heuristic arguments. An optimal way to choose $\underline{\boldsymbol{\mathcal{T}}}$ is still an open question and problem dependent. For instance, when the one-dimensional advection-diffusion steady case is considered, the following definition of $\underline{\boldsymbol{\mathcal{T}}}$ yields a nodally exact solution [10]:

$$\underline{\boldsymbol{\mathcal{T}}} = \frac{h_e}{2||a||}\left(\coth Pe - \frac{1}{Pe}\right), \qquad Pe = \frac{||a||h_e}{2\kappa}, \tag{3.5}$$

where h_e is a measure of the local length scale, also known as "element length", a is the flow velocity, κ is the diffusivity and Pe the Péclet number. Many definitions of h_e can be used; in the literature, it is common to use the element length aligned with the flow velocity. By analogy with formula (3.5), when dealing with convection-dominated systems of equations and isoparametric finite elements, the stabilization tensor is defined as

$$\underline{\mathcal{T}} \equiv \underline{\mathcal{T}}_{ad} = \frac{\|\frac{\partial \boldsymbol{x}}{\partial \boldsymbol{\zeta}}\|_2}{\|\Lambda\|_\infty}\mathbb{I}, \tag{3.6}$$

where Λ is the diagonal matrix of the system's eigenvalues and $\boldsymbol{\zeta}$ the local parameter coordinates that scale as unity, so that $\|\frac{\partial \boldsymbol{x}}{\partial \boldsymbol{\zeta}}\|_2$ is a local length. This derivation assumes the isotropy of wave propagation and does not take into account eventual anisotropies of the grid for large aspect ratios. This choice affects both the smoothness of the results in regions containing large variations of the solution and the conditioning of the discrete system. To overcome this limitation, a recovery technique is proposed by [29] and [42].

A different definition of the $\underline{\mathcal{T}}$ parameter has been proposed by [38] to take into account eventual anisotropies related to the density gradient. In the MHD context, anisotropies are driven by the magnetic field; thus, sharing some similarities with the formulation [38], we propose the following estimation of the stabilization parameter

$$\underline{\mathcal{T}} \equiv \underline{\mathcal{T}}_{tz} = \left(\sum_{\boldsymbol{i}\in\vartheta(e)} c_f \left| \frac{\mathbf{B}\cdot\nabla\mathcal{N}_{\boldsymbol{i}}}{\|\mathbf{B}\|} \right| + |\boldsymbol{v}\cdot\nabla\mathcal{N}_{\boldsymbol{i}}| \right)^{-1} \mathbb{I}, \tag{3.7}$$

where c_f is the fast acoustic speed. More general strategies were proposed and used in the context of space-time GLS[4], SUPG formulations[36, 2, 5, 41] and the residual distribution scheme ([1]). These approaches use the fact that, for any nonzero vector $\boldsymbol{n}$, the matrix $\underline{\mathbf{L}}_\star(\boldsymbol{w},\boldsymbol{n})$ is diagonalizable: $\underline{\mathbf{L}}_\star(\boldsymbol{w},\boldsymbol{n}) \equiv \underline{\mathbb{P}\boldsymbol{\Lambda}\mathbb{P}}^{-1}$. Therefore, the stabilization matrix is estimated as

$$\underline{\mathcal{T}} \equiv \underline{\mathcal{T}}_{gls} = \left(\sum_{\boldsymbol{i}\in\vartheta(e)} \underline{\mathbb{P}}(\boldsymbol{w},\nabla\mathcal{N}_{\boldsymbol{i}})\,|\underline{\boldsymbol{\Lambda}}(\boldsymbol{w},\nabla\mathcal{N}_{\boldsymbol{i}})|\,\underline{\mathbb{P}}^{-1}(\boldsymbol{w},\nabla\mathcal{N}_{\boldsymbol{i}}) \right)^{-1}. \tag{3.8}$$

This option requires a set of matrix inversions at each time step. Unfortunately, the MHD system can produce a non-diagonalizable matrix, so that this option is generally not retained.

A more interesting way to consider the magnetic field anisotropy is to use the following decomposition

$$\underline{\mathbf{L}}^{\mathrm{T}}(\boldsymbol{w},\boldsymbol{\partial}) = \underline{\mathbf{L}}_{\mathbf{B}}^{\mathrm{T}}(\boldsymbol{w},\boldsymbol{\partial}) + \underline{\mathbf{L}}_\star^{\mathrm{T}}(\boldsymbol{w},\boldsymbol{\partial}),$$

where

$$\underline{\mathbf{L}}_{\mathbf{B}}^{\mathrm{T}}(\boldsymbol{w},\boldsymbol{\partial}) = \underline{\mathbf{L}}^{\mathrm{T}}\left(\boldsymbol{w}, \frac{\mathbf{BB}\cdot\boldsymbol{\partial}}{\mathbf{B}\cdot\mathbf{B}}\right) \quad \text{and} \quad \underline{\mathbf{L}}_\star^{\mathrm{T}}(\boldsymbol{w},\boldsymbol{\partial}) = \underline{\mathbf{L}}^{\mathrm{T}}\left(\boldsymbol{w}, \boldsymbol{\partial} - \frac{\mathbf{BB}\cdot\boldsymbol{\partial}}{\mathbf{B}\cdot\mathbf{B}}\right).$$

A similar decomposition is used for $\underline{\mathbf{L}}(\boldsymbol{w},\boldsymbol{\partial})$ and it is assumed that this is a decomposition in orthogonal spaces. Therefore, the stabilization is reformulated as

$$\begin{aligned}\int_{\boldsymbol{\Omega}_{x,h}} \underline{\mathcal{T}}\underline{\mathbf{L}}(\boldsymbol{w},\boldsymbol{\partial})\,\delta\boldsymbol{w}\cdot\underline{\mathbf{L}}^{\mathrm{T}}(\boldsymbol{w},\boldsymbol{\partial})\,\boldsymbol{w}^\star \quad \simeq \quad & \int_{\boldsymbol{\Omega}_{x,h}} \mathcal{T}_{\mathbf{B}}\underline{\mathbf{L}}_{\mathbf{B}}(\boldsymbol{w},\boldsymbol{\partial})\,\delta\boldsymbol{w}\cdot\underline{\mathbf{L}}_{\mathbf{B}}^{\mathrm{T}}(\boldsymbol{w},\boldsymbol{\partial})\,\boldsymbol{w}^\star \\ & + \int_{\boldsymbol{\Omega}_{x,h}} \mathcal{T}_\star\underline{\mathbf{L}}_\star(\boldsymbol{w},\boldsymbol{\partial})\,\delta\boldsymbol{w}\cdot\underline{\mathbf{L}}_\star^{\mathrm{T}}(\boldsymbol{w},\boldsymbol{\partial})\,\boldsymbol{w}^\star\end{aligned}, \tag{3.9}$$

havig $\mathcal{T}_{\mathbf{B}}$ and $\mathcal{T}_\star$ constructed as usual, although different strategies could be used, taking into account the global anisotropy of the magnetized plasmas.

Set of interpolated variables. In tokamak plasmas, we have to deal with a very low density and pressure in the SOL. In order to avoid critical issues during the inversion of the equation of state, interpolations are often applied to the following physical variables $\mathbf{Y}$:

$$\mathbf{Y} = \begin{pmatrix} \rho \\ \boldsymbol{v} \\ T \\ \mathbf{A} \end{pmatrix} \quad \text{so that} \quad \boldsymbol{w} = \begin{pmatrix} \rho \\ \boldsymbol{m} = \rho \boldsymbol{v} \\ \mathcal{E} = \frac{\rho T}{\gamma - 1} + \frac{1}{2}\rho \boldsymbol{v} \cdot \boldsymbol{v} + \frac{1}{2}\mathbf{B} \cdot \mathbf{B} \\ \mathbf{B} \end{pmatrix}.$$

Let us point out that even though the interpolation is applied to physical variables, we are still using the formulation derived from the conservative equations. Therefore, we need to reformulate derivatives of $\boldsymbol{w}$ in terms of the derivatives of $\mathbf{Y}$:

$$\boldsymbol{\partial w} = \underline{\mathbf{M}}\left(\mathbf{Y}\right) \underline{\mathbf{Rot}}\left(\boldsymbol{\partial} \mathbf{Y}\right), \tag{3.10}$$

where

$$\underline{\mathbf{M}}\left(\mathbf{Y}\right) = \left(\begin{array}{c|c|c|c} 1 & 0 & 0 & 0 \\ \hline \boldsymbol{v} & \rho \mathbb{I} & 0 & 0 \\ \hline \dfrac{T}{\gamma - 1} + \dfrac{\boldsymbol{v} \cdot \boldsymbol{v}}{2} & \rho \boldsymbol{v}^{\mathrm{T}} & \dfrac{\rho}{\gamma - 1} & \mathbf{B}^{\mathrm{T}} \\ \hline 0 & 0 & 0 & \mathbb{I} \end{array}\right) \quad \text{and} \quad \underline{\mathbf{Rot}}\left(\boldsymbol{\partial} \mathbf{Y}\right) = \begin{pmatrix} \boldsymbol{\partial} \rho \\ \boldsymbol{\partial v} \\ \boldsymbol{\partial} T \\ \nabla \times \mathbf{A} \end{pmatrix}.$$

When the numerical approximation uses $\mathbf{Y}$ for interpolation, the integrals should be reformulated according to the associated change of variable. The time derivative becomes

$$\begin{aligned} \int_{\boldsymbol{\Omega}_{x,h}} \frac{\partial \boldsymbol{w}}{\partial t} \cdot \boldsymbol{w}^{\star} &= \int_{\boldsymbol{\Omega}_{x,h}} \left(\underline{\mathbf{M}}\left(\mathbf{Y}\right) \underline{\mathbf{Rot}} \left(\frac{\partial \mathbf{Y}}{\partial t} \right) \right) \cdot \boldsymbol{w}^{\star} = \int_{\boldsymbol{\Omega}_{x,h}} \left(\underline{\mathbf{Rot}} \left(\underline{\mathbf{M}}\left(\mathbf{Y}\right) \frac{\partial \mathbf{Y}}{\partial t} \right) \right) \cdot \boldsymbol{w}^{\star} \\ &= \int_{\boldsymbol{\Omega}_{x,h}} \left(\underline{\mathbf{M}}\left(\mathbf{Y}\right) \frac{\partial \mathbf{Y}}{\partial t} \right) \cdot \underline{\mathbf{Rot}}\left(\boldsymbol{w}^{\star}\right) + \int_{\partial \boldsymbol{\Omega}_{x,h}} \underline{\mathbf{D}} \boldsymbol{n} \cdot \boldsymbol{w}^{\star} \\ &= \int_{\boldsymbol{\Omega}_{x,h}} \left(\underline{\mathbf{M}}\left(\mathbf{Y}\right) \frac{\partial \mathbf{Y}}{\partial t} \right) \cdot \widetilde{\boldsymbol{w}}^{\star} + \int_{\partial \boldsymbol{\Omega}_{x,h}} \left(\boldsymbol{n} \times \frac{\partial \mathbf{A}}{\partial t} \right) \cdot \mathbf{B}^{\star} \end{aligned},$$

where the test vector functions are defined as

$$\boldsymbol{w}^{\star} = \begin{pmatrix} \rho^{\star} \\ \boldsymbol{m}^{\star} \\ \mathcal{E}^{\star} \\ \mathbf{B}^{\star} \end{pmatrix} \quad \text{and} \quad \widetilde{\boldsymbol{w}}^{\star} = \begin{pmatrix} \rho^{\star} \\ \boldsymbol{m}^{\star} \\ \mathcal{E}^{\star} \\ \mathbf{J}^{\star} \end{pmatrix} \quad \text{with} \quad \mathbf{J}^{\star} = \nabla \times \mathbf{B}^{\star}.$$

Stabilized weak formulation. Integration by parts is performed on the residual integral and additional contributions are added to take into account the Dirichlet boundary conditions as penalty boundary integrals. Therefore, the VMS-stabilized finite element takes the following compact form:

$$\boxed{\begin{aligned} &\int_{\boldsymbol{\Omega}_{x,h}} \left(\underline{\mathbf{M}}\left(\mathbf{Y}\right) \frac{\partial \mathbf{Y}}{\partial t} \right) \cdot \widetilde{\boldsymbol{w}}^{\star} - \int_{\boldsymbol{\Omega}_{x,h}} \underline{\mathbf{F}} : \left(\boldsymbol{\partial} \odot \boldsymbol{w}^{\star}\right) + \int_{\boldsymbol{\Omega}_{x,h}} \underline{\mathbf{D}} : \left(\boldsymbol{\partial} \odot \boldsymbol{w}^{\star}\right) - \frac{1}{\varepsilon} \int_{\boldsymbol{\Omega}_{x,h}} \left(\nabla \cdot \mathbf{A}\right) \cdot \left(\nabla \cdot \mathbf{A}^{\star}\right) \\ &\quad + \int_{\partial \boldsymbol{\Omega}_{x,h}} \underline{\mathbf{F}} : \left(\boldsymbol{n} \odot \boldsymbol{w}^{\star}\right) - \int_{\partial \boldsymbol{\Omega}_{x,h}} \underline{\mathbf{D}} : \left(\boldsymbol{n} \odot \boldsymbol{w}^{\star}\right) - \frac{1}{\varepsilon} \int_{\partial \boldsymbol{\Omega}_{x,h}} \left(\boldsymbol{n} \times \partial_t \mathbf{A}\right) \cdot \mathbf{B}^{\star} + \frac{1}{\varepsilon} \int_{\partial \boldsymbol{\Omega}_{x,h}} \mathbf{S}\left(\boldsymbol{w}, \boldsymbol{w}_b, \boldsymbol{w}^{\star}\right) \\ &\qquad = - \int_{\boldsymbol{\Omega}_{x,h}} \left(\underline{\mathbf{L}}\left(\boldsymbol{w}, \boldsymbol{\partial}\right) \delta \boldsymbol{w} \right) \cdot \underline{\boldsymbol{\mathcal{T}}} \left(\underline{\mathbf{L}}^{\mathrm{T}}\left(\boldsymbol{w}, \boldsymbol{\partial}\right) \boldsymbol{w}^{\star} \right). \end{aligned}} \tag{3.11}$$

The operator $\odot$, acting between a vector (size d) and a state vector of size N_v, has as result a $N_v \times d$ tensor, where N_v is the total number of scalar variables (it is also the size of $\boldsymbol{w}$) and d the space dimension assumed to be also the dimension of considered vectors (as $\boldsymbol{v}$ and $\mathbf{B}$). The resulting tensors are defined as follows:

$$(\boldsymbol{\partial} \odot \boldsymbol{w}^\star) = \begin{pmatrix} \boldsymbol{\partial}\rho^\star \\ \boldsymbol{\partial} \otimes \boldsymbol{m}^\star \\ \boldsymbol{\partial}\mathcal{E}^\star \\ \boldsymbol{\partial} \times \mathbf{B}^\star \end{pmatrix}, \quad (\boldsymbol{n} \odot \boldsymbol{w}^\star) = \begin{pmatrix} \boldsymbol{n}\rho^\star \\ \boldsymbol{n} \otimes \boldsymbol{m}^\star \\ \boldsymbol{n}\mathcal{E}^\star \\ \boldsymbol{n} \times \mathbf{B}^\star \end{pmatrix},$$

with

$$\boldsymbol{\partial} \otimes \boldsymbol{m} = \begin{pmatrix} \boldsymbol{\partial}_1\boldsymbol{m}_1 & \boldsymbol{\partial}_1\boldsymbol{m}_2 & \boldsymbol{\partial}_1\boldsymbol{m}_3 \\ \boldsymbol{\partial}_2\boldsymbol{m}_1 & \boldsymbol{\partial}_2\boldsymbol{m}_2 & \boldsymbol{\partial}_2\boldsymbol{m}_3 \\ \boldsymbol{\partial}_3\boldsymbol{m}_1 & \boldsymbol{\partial}_3\boldsymbol{m}_2 & \boldsymbol{\partial}_3\boldsymbol{m}_3 \end{pmatrix}.$$

Also note that

$$(\boldsymbol{m} \otimes \boldsymbol{\partial})^{\mathrm{T}} = \begin{pmatrix} \boldsymbol{m}_1\boldsymbol{\partial}_1 & \boldsymbol{m}_2\boldsymbol{\partial}_1 & \boldsymbol{m}_3\boldsymbol{\partial}_1 \\ \boldsymbol{m}_1\boldsymbol{\partial}_2 & \boldsymbol{m}_2\boldsymbol{\partial}_2 & \boldsymbol{m}_3\boldsymbol{\partial}_2 \\ \boldsymbol{m}_1\boldsymbol{\partial}_3 & \boldsymbol{m}_2\boldsymbol{\partial}_3 & \boldsymbol{m}_3\boldsymbol{\partial}_3 \end{pmatrix},$$

then

$$(\boldsymbol{m} \otimes \boldsymbol{\partial})^{\mathrm{T}} \boldsymbol{m}^\star = \begin{pmatrix} \boldsymbol{m}_1\boldsymbol{\partial}_1\boldsymbol{m}^\star{}_1 + \boldsymbol{m}_2\boldsymbol{\partial}_1\boldsymbol{m}^\star{}_2 + \boldsymbol{m}_3\boldsymbol{\partial}_1\boldsymbol{m}^\star{}_3 \\ \boldsymbol{m}_1\boldsymbol{\partial}_2\boldsymbol{m}^\star{}_1 + \boldsymbol{m}_2\boldsymbol{\partial}_2\boldsymbol{m}^\star{}_2 + \boldsymbol{m}_3\boldsymbol{\partial}_2\boldsymbol{m}^\star{}_3 \\ \boldsymbol{m}_1\boldsymbol{\partial}_3\boldsymbol{m}^\star{}_1 + \boldsymbol{m}_2\boldsymbol{\partial}_3\boldsymbol{m}^\star{}_2 + \boldsymbol{m}_3\boldsymbol{\partial}_3\boldsymbol{m}^\star{}_3 \end{pmatrix} = (\boldsymbol{\partial}\boldsymbol{m}^\star)\,\boldsymbol{m}.$$

The hyperbolic (convection) flux tensor $\underline{\mathbf{F}}$ and the elliptic (diffusion) flux tensor $\underline{\mathbf{D}}$ have the shape size of $N_v \times d$. The contribution having $\partial_t\mathbf{A}$ is associated to the integration by parts in the time derivative integral, when the magnetic field $\mathbf{B}$ is formulated as the curl of the potential vector $\mathbf{A}$. These tensors are written as follows

$$\underline{\mathbf{F}} = \begin{pmatrix} \rho\boldsymbol{v} \\ \rho\boldsymbol{v} \otimes \boldsymbol{v} + \mathrm{P}\mathbb{I} - \mathbf{B} \otimes \mathbf{B} \\ \rho\mathcal{H}\boldsymbol{v} - \mathbf{B} \cdot \boldsymbol{v}\mathbf{B} \\ -\boldsymbol{v} \times \mathbf{B} \end{pmatrix}, \quad \underline{\mathbf{D}} = \begin{pmatrix} \underline{\boldsymbol{D}}\boldsymbol{\partial}\rho' \\ \underline{\boldsymbol{\tau}} \\ \underline{\boldsymbol{\tau}}\boldsymbol{v} \\ -(\mathbf{E} + \boldsymbol{v} \times \mathbf{B}) \end{pmatrix}.$$

Dirichlet boundary conditions are considered as penalty defined with boundary integrals. The vector $\mathbf{S}$ to be integrated is a function of the local state $\boldsymbol{w}$ and the state to be enforced $\boldsymbol{w}_b$. In the current context, this vector is defined as:

$$\mathbf{S}\left(\boldsymbol{w}, \boldsymbol{w}_b, \boldsymbol{w}^\star\right) = \begin{pmatrix} (\rho - \rho_b)\,\rho^\star\boldsymbol{\mathcal{X}}\left(\partial\boldsymbol{\Omega}^{\rho}_{x,h}\right) \\ \rho\left(\boldsymbol{v} - \boldsymbol{v}_b\right) \cdot \boldsymbol{m}^\star\boldsymbol{\mathcal{X}}\left(\partial\boldsymbol{\Omega}^{\boldsymbol{v}}_{x,h}\right) + (\rho\boldsymbol{v} - \boldsymbol{m}_b) \cdot \boldsymbol{m}^\star\boldsymbol{\mathcal{X}}\left(\partial\boldsymbol{\Omega}^{\boldsymbol{m}}_{x,h}\right) \\ \rho\left(T - T_b\right)\mathcal{E}^\star\boldsymbol{\mathcal{X}}\left(\partial\boldsymbol{\Omega}^{T}_{x,h}\right) + (p - p_b)\,\mathcal{E}^\star\boldsymbol{\mathcal{X}}\left(\partial\boldsymbol{\Omega}^{p}_{x,h}\right) \\ (\mathbf{A} - \mathbf{A}_b) \cdot \mathbf{J}^\star\boldsymbol{\mathcal{X}}\left(\partial\boldsymbol{\Omega}^{\mathbf{A}}_{x,h}\right) + (\mathbf{B} - \mathbf{B}_b) \cdot \mathbf{B}^\star\boldsymbol{\mathcal{X}}\left(\partial\boldsymbol{\Omega}^{\mathbf{B}}_{x,h}\right) \end{pmatrix},$$

where, for any subset $\boldsymbol{\mathcal{Y}}$ of the boundary $\partial\boldsymbol{\Omega}_{x,h}$, $\boldsymbol{\mathcal{X}}\left(\boldsymbol{\mathcal{Y}}\right)$ is the characteristic function of $\boldsymbol{\mathcal{Y}}$. It is also assumed that the boundaries do not overlap so that, for example, the pressure and the temperature are always penalized over different subsets.

The stabilization is associated to the vectors $\underline{\mathbf{L}}\left(\boldsymbol{w}, \boldsymbol{\partial}\right)\delta\boldsymbol{w}$, $\underline{\mathbf{L}}^{\mathrm{T}}\left(\boldsymbol{w}, \boldsymbol{\partial}\right)\boldsymbol{w}^\star$ and the scaling tensor $\underline{\boldsymbol{\mathcal{T}}}$. For any direction $\boldsymbol{n}$, $\underline{\mathbf{L}}\left(\boldsymbol{w}, \boldsymbol{n}\right)$ is an exact or approximated Jacobian of $\underline{\mathbf{F}}\boldsymbol{n}$ with respect to $\boldsymbol{w}$.

When the exact Jacobian is used, we have

$$\underline{\mathbf{L}}\left(\boldsymbol{w},\boldsymbol{\partial}\right)\delta\boldsymbol{w} = \left(\begin{array}{c} \boldsymbol{\partial}\cdot\delta\boldsymbol{m} \\ \hline -\boldsymbol{v}\boldsymbol{v}\cdot\boldsymbol{\partial}\delta\rho + \frac{\partial \mathrm{P}}{\partial\rho}\boldsymbol{\partial}\delta\rho + \boldsymbol{v}\boldsymbol{\partial}\cdot\left(\delta\boldsymbol{m}\right) + \boldsymbol{v}\cdot\boldsymbol{\partial}\delta\boldsymbol{m} + \left(\boldsymbol{\partial}\delta\boldsymbol{m}\right)\frac{\partial \mathrm{P}}{\partial\boldsymbol{m}} \\ + \frac{\partial \mathrm{P}}{\partial\mathcal{E}}\boldsymbol{\partial}\delta\mathcal{E} + \left(\boldsymbol{\partial}\delta\mathbf{B}\right)\frac{\partial \mathrm{P}}{\partial\mathbf{B}} + \left(\boldsymbol{\partial}\delta\mathbf{B}\right)\mathbf{B} - \mathbf{B}\cdot\boldsymbol{\partial}\delta\mathbf{B} \\ \hline \frac{\partial\mathcal{H}}{\partial\rho}\boldsymbol{m}\cdot\boldsymbol{\partial}\delta\rho + \frac{\mathbf{B}\cdot\boldsymbol{m}}{\rho^2}\mathbf{B}\cdot\boldsymbol{\partial}\delta\rho + \left(\frac{\partial\mathcal{H}}{\partial\boldsymbol{m}}\right)^{\mathrm{T}}\boldsymbol{m}\cdot\boldsymbol{\partial}\delta\boldsymbol{m} + \mathcal{H}\boldsymbol{\partial}\cdot\delta\boldsymbol{m} - \frac{\mathbf{B}^{\mathrm{T}}}{\rho}\mathbf{B}\cdot\boldsymbol{\partial}\delta\boldsymbol{m} \\ + \frac{\partial\mathcal{H}}{\partial\mathcal{E}}\boldsymbol{m}\cdot\boldsymbol{\partial}\delta\mathcal{E} + \frac{\partial\mathcal{H}}{\partial\mathbf{B}}^{\mathrm{T}}\boldsymbol{m}\cdot\boldsymbol{\partial}\delta\mathbf{B} - \frac{\mathbf{B}\cdot\boldsymbol{m}}{\rho}\boldsymbol{\partial}\cdot\delta\mathbf{B} - \frac{\boldsymbol{m}^{\mathrm{T}}\mathbf{B}\cdot\boldsymbol{\partial}\delta\mathbf{B}}{\rho} \\ \hline -\frac{\mathbf{B}\boldsymbol{m}\cdot\boldsymbol{\partial}\delta\rho - \boldsymbol{m}\mathbf{B}\cdot\boldsymbol{\partial}\delta\rho}{\rho^2} + \frac{\mathbf{B}\boldsymbol{\partial}\cdot\delta\boldsymbol{m} - \mathbf{B}\cdot\boldsymbol{\partial}\delta\boldsymbol{m}}{\rho} + \frac{\boldsymbol{m}\cdot\boldsymbol{\partial}\delta\mathbf{B} - \left(\boldsymbol{\partial}\delta\mathbf{B}\right)\boldsymbol{m}}{\rho} \end{array}\right)$$

and

$$\underline{\mathbf{L}}^{\mathrm{T}}\left(\boldsymbol{w},\boldsymbol{\partial}\right)\boldsymbol{w}^{\star} = \left(\begin{array}{c} -\frac{\boldsymbol{m}^{\mathrm{T}}}{\rho^2}\boldsymbol{m}\cdot\boldsymbol{\partial}\boldsymbol{m}^{\star} + \frac{\partial \mathrm{P}}{\partial\rho}\boldsymbol{\partial}\cdot\boldsymbol{m}^{\star} + \frac{\partial\mathcal{H}}{\partial\rho}\boldsymbol{m}\cdot\boldsymbol{\partial}\mathcal{E}^{\star} + \frac{\mathbf{B}\cdot\boldsymbol{m}}{\rho^2}\mathbf{B}\cdot\boldsymbol{\partial}\mathcal{E}^{\star} - \frac{\mathbf{B}^{\mathrm{T}}\boldsymbol{m}\cdot\boldsymbol{\partial}\mathbf{B}^{\star} - \boldsymbol{m}^{\mathrm{T}}\mathbf{B}\cdot\boldsymbol{\partial}\mathbf{B}^{\star}}{\rho^2} \\ \hline \boldsymbol{\partial}\rho^{\star} + \left(\boldsymbol{\partial}\boldsymbol{m}^{\star}\right)\boldsymbol{v} + \boldsymbol{v}\cdot\boldsymbol{\partial}\boldsymbol{m}^{\star} + \frac{\partial \mathrm{P}}{\partial\boldsymbol{m}}\boldsymbol{\partial}\cdot\boldsymbol{m}^{\star} \\ + \frac{\partial\mathcal{H}}{\partial\boldsymbol{m}}\boldsymbol{m}\cdot\boldsymbol{\partial}\mathcal{E}^{\star} + \mathcal{H}\boldsymbol{\partial}\mathcal{E}^{\star} - \frac{\mathbf{B}}{\rho}\mathbf{B}\cdot\boldsymbol{\partial}\mathcal{E}^{\star} + \frac{\left(\boldsymbol{\partial}\mathbf{B}^{\star}\right)\mathbf{B} - \mathbf{B}\cdot\boldsymbol{\partial}\mathbf{B}^{\star}}{\rho} \\ \hline \frac{\partial \mathrm{P}}{\partial\mathcal{E}}\boldsymbol{\partial}\cdot\boldsymbol{m}^{\star} + \frac{\partial\mathcal{H}}{\partial\mathcal{E}}\boldsymbol{m}\cdot\boldsymbol{\partial}\mathcal{E}^{\star} \\ \hline \frac{\partial \mathrm{P}}{\partial\mathbf{B}}\boldsymbol{\partial}\cdot\boldsymbol{m}^{\star} + \mathbf{B}\left(\boldsymbol{\partial}\cdot\boldsymbol{m}^{\star}\right) - \mathbf{B}\cdot\boldsymbol{\partial}\boldsymbol{m}^{\star} \\ + \frac{\partial\mathcal{H}}{\partial\mathbf{B}}\boldsymbol{m}\cdot\boldsymbol{\partial}\mathcal{E}^{\star} - \frac{\mathbf{B}\cdot\boldsymbol{m}}{\rho}\boldsymbol{\partial}\mathcal{E}^{\star} - \frac{\boldsymbol{m}\mathbf{B}\cdot\boldsymbol{\partial}\mathcal{E}^{\star}}{\rho} + \frac{\boldsymbol{m}\cdot\boldsymbol{\partial}\mathbf{B}^{\star} - \left(\boldsymbol{\partial}\mathbf{B}^{\star}\right)\boldsymbol{m}}{\rho} \end{array}\right).$$

In practice, as we are using an interpolation of the primitive variables $\mathbf{Y}$, the previous vector $\underline{\mathbf{L}}\left(\boldsymbol{w},\boldsymbol{\partial}\right)\delta\boldsymbol{w}$ is reformulated in order to get out an explicit dependency to $\delta\mathbf{Y}$.

Finite element approximated space. Going back to the system (3.11), we now need to derive an approximated space for the test functions. First of all, let us consider a scalar function defined over a domain $\boldsymbol{\Omega}_x$. This function will be then interpolated in an approximated finite element space $\boldsymbol{\mathcal{V}}_h \equiv \boldsymbol{\mathcal{V}}_h\left(\boldsymbol{\Omega}_{x,h}\right)$ spanned by the test functions $\mathcal{N}_{\boldsymbol{i}}$. As we will focus on toroidal geometries with cylindrical symmetry the approximated space is obtained as a tensor product of a 2D and a 1D function space:

$$\boldsymbol{\mathcal{V}}_h\left(\boldsymbol{\Omega}_{x,h}\right) \equiv \boldsymbol{\mathcal{V}}_h\left(\boldsymbol{\Omega}_{2\mathrm{D}}\right) \times \boldsymbol{\mathcal{V}}_h\left([0,2\pi[\right).$$

At this point, it is useful to introduce the cylindrical coordinates $\left(\mathrm{R},\phi,\mathrm{Z}\right)$ that contain the poloidal coordinate $\boldsymbol{\xi} = \left(\mathrm{R},\mathrm{Z}\right)^{\mathrm{T}}$ with $\boldsymbol{\xi} \in \boldsymbol{\Omega}_{2\mathrm{D}}$ and the toroidal coordinate $\phi \in [0,2\pi[$. There is a nonsingular mapping between the Cartesian coordinate $\boldsymbol{x}$ and the cylindrical coordinates: $\boldsymbol{x} \equiv \boldsymbol{x}\left(\mathrm{R},\phi,\mathrm{Z}\right) \equiv \boldsymbol{x}\left(\boldsymbol{\xi},\phi\right)$. Therefore, according to the mapping $\boldsymbol{x}\left(\boldsymbol{\xi},\phi\right)$, volume and surface integrals are reformulated as

$$\int_{\boldsymbol{\Omega}_x}\left(\cdots\right)d\boldsymbol{x} = \int_0^{2\pi}d\phi\int_{\boldsymbol{\Omega}_{2\mathrm{D}}}\left(\cdots\right)\mathrm{R}d\boldsymbol{\xi} \quad \text{and} \quad \int_{\partial\boldsymbol{\Omega}_x}\left(\cdots\right)d\mathrm{S}_x = \int_0^{2\pi}d\phi\int_{\partial\boldsymbol{\Omega}_{2\mathrm{D}}}\left(\cdots\right)\mathrm{R}d\mathrm{S}_{\boldsymbol{\xi}}, \tag{3.12}$$

where R is the Jacobian of the mapping. For applications to tokamak geometries, the position $\mathrm{R} = 0$ is almost always out of the domain $\boldsymbol{\Omega}_x$ and we do not have to face any problem of singularity. Then it is desirable and even advantageous to express the interpolation functions according to cylindrical variables $\left(\boldsymbol{\xi},\mathrm{Z}\right)$. The representing of vectors $\left(\boldsymbol{v},\boldsymbol{m},\mathbf{B},\mathbf{A},\boldsymbol{m}^{\star},\mathbf{A}^{\star},\mathbf{B}^{\star}\cdots\right)$ is also related to the three unit directions vectors $\left(\widehat{\mathbf{R}},\widehat{\boldsymbol{\phi}},\widehat{\mathbf{Z}}\right)$ (orthogonal). For example

$$\boldsymbol{m}^{\star}\left(\boldsymbol{\xi},\phi\right) := \boldsymbol{m}^{\star}_{\mathrm{R}}\left(\boldsymbol{\xi},\phi\right)\widehat{\mathbf{R}} + \boldsymbol{m}^{\star}_{\phi}\left(\boldsymbol{\xi},\phi\right)\widehat{\boldsymbol{\phi}} + \boldsymbol{m}^{\star}_{\mathrm{Z}}\left(\boldsymbol{\xi},\phi\right)\widehat{\mathbf{Z}}.$$

The tricky point is that the vectors $\widehat{\mathbf{R}}$ and $\widehat{\boldsymbol{\phi}}$ are also functions of the plane polar coordinates $\left(\mathrm{R},\phi\right)$. We can formally describe the space for representing vectors as

$$\vec{\boldsymbol{\mathcal{V}}}_{\boldsymbol{h}}\left(\boldsymbol{\Omega}_{x,h}\right) := \boldsymbol{\mathcal{V}}_h\left(\boldsymbol{\Omega}_{x,h}\right)\widehat{\mathbf{R}}\left(\mathrm{R},\phi\right)\bigoplus\boldsymbol{\mathcal{V}}_h\left(\boldsymbol{\Omega}_{x,h}\right)\widehat{\boldsymbol{\phi}}\left(\mathrm{R},\phi\right)\bigoplus\boldsymbol{\mathcal{V}}_h\left(\boldsymbol{\Omega}_{x,h}\right)\widehat{\mathbf{Z}}.$$

However, for the potential vector, the approximation space is slightly different. Indeed, in the context of MHD instabilities, the initial condition is computed as the solution of the Grad-Shafranov equation which is a nonlinear elliptic equation for the toroidal component ψ of the vector potential, associated to the vector $\nabla\phi$ that is not unitary: $\nabla\phi\frac{1}{\mathrm{R}}\widehat{\boldsymbol{\phi}}$. Thus, in order to avoid numerical perturbations related to the projection in a normalized basis, the vector variable $\mathbf{A}$ (only this variable and not the associated test function), is represented in the space

$$\vec{\boldsymbol{\mathcal{V}}}_{\boldsymbol{h}}\left(\boldsymbol{\Omega}_{x,h}\right) := \boldsymbol{\mathcal{V}}_h\left(\boldsymbol{\Omega}_{x,h}\right)\widehat{\mathbf{R}}\left(\mathrm{R},\phi\right)\bigoplus\boldsymbol{\mathcal{V}}_h\left(\boldsymbol{\Omega}_{x,h}\right)\frac{\widehat{\boldsymbol{\phi}}\left(\mathrm{R},\phi\right)}{\mathrm{R}}\bigoplus\boldsymbol{\mathcal{V}}_h\left(\boldsymbol{\Omega}_{x,h}\right)\widehat{\mathbf{Z}}.$$

Therefore

$$\mathbf{A}\left(t,\boldsymbol{\xi},\phi\right) := \mathbf{A}_{\mathrm{R}}\left(t,\boldsymbol{\xi},\phi\right)\widehat{\mathbf{R}} + \psi\left(t,\boldsymbol{\xi},\phi\right)\nabla\phi + \mathbf{A}_{\mathrm{Z}}\left(t,\boldsymbol{\xi},\phi\right)\widehat{\mathbf{Z}},$$

with $\psi\left(t,\boldsymbol{\xi},\phi\right) = \mathrm{R}\mathbf{A}_{\phi}\left(t,\boldsymbol{\xi},\phi\right)$. The dependence on polar coordinates (for $\widehat{\mathbf{R}}$ and $\widehat{\boldsymbol{\phi}}$ or $\nabla\phi$) must be taken into account when estimating the gradients of vectors (for example $\boldsymbol{\partial m}^{\star}$). We will use the following explicit relations for the gradient of $\widehat{\mathbf{R}}$ and $\widehat{\boldsymbol{\phi}}$:

$$\boldsymbol{\partial}\widehat{\mathbf{R}} = \frac{1}{\mathrm{R}}\widehat{\boldsymbol{\phi}}\otimes\widehat{\boldsymbol{\phi}} \quad \text{and} \quad \boldsymbol{\partial}\widehat{\boldsymbol{\phi}} = -\frac{1}{\mathrm{R}}\widehat{\mathbf{R}}\otimes\widehat{\boldsymbol{\phi}}.$$

Then, for any vector $\boldsymbol{Y} = \boldsymbol{Y}_{\mathrm{R}}\widehat{\mathbf{R}} + \boldsymbol{Y}_{\phi}\widehat{\boldsymbol{\phi}} + \boldsymbol{Y}_{\mathrm{Z}}\widehat{\mathbf{Z}}$, the gradient is given by

$$\boldsymbol{\partial Y} = \widehat{\mathbf{R}}\otimes\boldsymbol{\partial Y}_{\mathrm{R}} + \widehat{\boldsymbol{\phi}}\otimes\boldsymbol{\partial Y}_{\phi} + \widehat{\mathbf{Z}}\otimes\boldsymbol{\partial Y}_{\mathrm{Z}} + \frac{\boldsymbol{Y}_{\mathrm{R}}}{\mathrm{R}}\widehat{\boldsymbol{\phi}}\otimes\widehat{\boldsymbol{\phi}} - \frac{\boldsymbol{Y}_{\phi}}{\mathrm{R}}\widehat{\mathbf{R}}\otimes\widehat{\boldsymbol{\phi}},$$

where each component $\boldsymbol{\partial Y}_m$ is also defined in the cylindrical basis:

$$\boldsymbol{\partial Y}_m = \widehat{\mathbf{R}}\partial_{\mathrm{R}}\boldsymbol{Y}_m + \widehat{\boldsymbol{\phi}}\frac{1}{\mathrm{R}}\partial_{\phi}\boldsymbol{Y}_m + \widehat{\mathbf{Z}}\partial_{\mathrm{Z}}\boldsymbol{Y}_m.$$

The components $\boldsymbol{Y}_m$ and of vector functions belong to the finite element space $\boldsymbol{\mathcal{V}}_h\left(\boldsymbol{\Omega}_{x,h}\right)$. This space, for a scalar function and in the context of cylindrical geometries, is formulated as a tensor product of poloidal (2D) and toroidal functions(1D). The approximated poloidal space is spanned by functions $\psi_{i_{2\mathrm{D}}}$ and the approximated toroidal space is spanned by functions $\mathrm{C}_{i_{\phi}}\left(\phi\right)$ where $i_{2\mathrm{D}} = 1,\cdots,N_{i_{2\mathrm{D}}}$ and $i_{\phi} = 1,\cdots,N_{itor}$:

$$\boldsymbol{\mathcal{V}}_h\left(\boldsymbol{\Omega}_{2\mathrm{D}}\right) \equiv \mathrm{SPAN}\left(\psi_{i_{2\mathrm{D}}}\left(\boldsymbol{\xi}\right)\right) \quad \text{and} \quad \boldsymbol{\mathcal{V}}_h\left([0,2\pi[\right) \equiv \mathrm{SPAN}\left(\mathrm{C}_{i_{\phi}}\left(\phi\right)\right).$$

$N_{i_{2\mathrm{D}}}$ and N_{itor} are the dimensions of the poloidal and the toroidal spaces, respectively. We will consider for $\psi_{i_{2\mathrm{D}}}$ the 2D Beziers finite element construction, proposed in [13] over quadrangular meshes. This is an isoparametric construction that globally enforces the C1 continuity of test functions in the physical space. Moreover, there are four degrees of freedom associated to each vertex of the mesh and this makes easy the construction of the compressed graph that is used to speed-up the resolution of the numerical scheme. According to its periodic nature, the toroidal space is decomposed in the Fourier space spanned by the cosine and sine functions. This is also a hierarchical basis and this helps to design efficient preconditioning. The drawback is that all the modes are coupled and the linearized discrete system is dense in the toroidal direction. Nevertheless, this strategy is attractive for research of MHD instabilities in tokamaks.

The global approximation space is then defined as follows

$$\boldsymbol{\mathcal{V}}_h\left(\boldsymbol{\Omega}_{x,h}\right) = \mathrm{SPAN}\left(\mathcal{N}_{\boldsymbol{i}}\left(\boldsymbol{\xi},\phi\right) = \psi_{i_{2\mathrm{D}}}\left(\boldsymbol{\xi}\right)\mathrm{C}_{i_{\phi}}\left(\phi\right)\right)$$

where $\boldsymbol{i} \equiv \boldsymbol{i}\left(i_{2\mathrm{D}},i_{\phi}\right) = 1,\cdots,N_{i_{2\mathrm{D}}}N_{i_{\phi}}$.

In the present paper, the variables $\mathbf{Y}$ and the test functions $\boldsymbol{w}^\star$ and $\widetilde{\boldsymbol{w}}^\star$ belong to the same space $\vec{\boldsymbol{\mathcal{W}}}_{\boldsymbol{h}}(\boldsymbol{\Omega}_{x,h})$:

$$\vec{\boldsymbol{\mathcal{W}}}_{\boldsymbol{h}}(\boldsymbol{\Omega}_{x,h}) := \boldsymbol{\mathcal{V}}_h(\boldsymbol{\Omega}_{x,h}) \times \vec{\boldsymbol{\mathcal{V}}}_{\boldsymbol{h}}(\boldsymbol{\Omega}_{x,h}) \times \boldsymbol{\mathcal{V}}_h(\boldsymbol{\Omega}_{x,h}) \times \vec{\boldsymbol{\mathcal{V}}}_{\boldsymbol{h}}(\boldsymbol{\Omega}_{x,h}). \tag{3.13}$$

This space is spanned by the vector test functions

$$\begin{aligned}
\boldsymbol{w}^\star_{\rho,\boldsymbol{i}} &= \begin{pmatrix} \mathcal{N}_{\boldsymbol{i}} \\ 0 \\ 0 \\ 0 \end{pmatrix}, \quad \boldsymbol{w}^\star_{\boldsymbol{v}_{\mathrm{R}},\boldsymbol{i}} = \begin{pmatrix} 0 \\ \mathcal{N}_{\boldsymbol{i}}\widehat{\mathbf{R}} \\ 0 \\ 0 \end{pmatrix}, \boldsymbol{w}^\star_{\boldsymbol{v}_{\phi},\boldsymbol{i}} = \begin{pmatrix} 0 \\ \mathcal{N}_{\boldsymbol{i}}\widehat{\boldsymbol{\phi}} \\ 0 \\ 0 \end{pmatrix}, \boldsymbol{w}^\star_{\boldsymbol{v}_{\mathrm{Z}},\boldsymbol{i}} = \begin{pmatrix} 0 \\ \mathcal{N}_{\boldsymbol{i}}\widehat{\mathbf{Z}} \\ 0 \\ 0 \end{pmatrix}, \\
\boldsymbol{w}^\star_{\mathcal{E},\boldsymbol{i}} &= \begin{pmatrix} 0 \\ 0 \\ \mathcal{N}_{\boldsymbol{i}} \\ 0 \end{pmatrix}, \quad \boldsymbol{w}^\star_{\mathbf{A}_{\mathrm{R}},\boldsymbol{i}} = \begin{pmatrix} 0 \\ 0 \\ 0 \\ \mathcal{N}_{\boldsymbol{i}}\widehat{\mathbf{R}} \end{pmatrix}, \boldsymbol{w}^\star_{\mathbf{A}_{\phi},\boldsymbol{i}} = \begin{pmatrix} 0 \\ 0 \\ 0 \\ \mathcal{N}_{\boldsymbol{i}}\widehat{\boldsymbol{\phi}} \end{pmatrix}, \boldsymbol{w}^\star_{\mathbf{A}_{\mathrm{Z}},\boldsymbol{i}} = \begin{pmatrix} 0 \\ 0 \\ 0 \\ \mathcal{N}_{\boldsymbol{i}}\widehat{\mathbf{Z}} \end{pmatrix},
\end{aligned} \tag{3.14}$$

with $\mathcal{N}_{\boldsymbol{i}} \in \boldsymbol{\mathcal{V}}_h(\boldsymbol{\Omega}_{x,h})$. Interpolation of the primitive variable $\mathbf{Y}(t,\boldsymbol{\xi},\phi)$ can be formulated as

$$\mathbf{Y}(t,\boldsymbol{\xi},\phi) = \sum_{\boldsymbol{j}=1}^{N_{i_{2\mathrm{D}}} N_{i_\phi}} \mathbf{Y}_{\boldsymbol{j}}(t)\,\mathcal{N}_{\boldsymbol{j}}(\boldsymbol{\xi},\phi), \tag{3.15}$$

where $\mathbf{Y}_{\boldsymbol{j}}(t)$ is the unknown vector associated to the test function $\mathcal{N}_{\boldsymbol{j}}(\boldsymbol{\xi},\phi)$

$$\mathbf{Y}_{\boldsymbol{j}}(t) = \begin{pmatrix} \rho_{\boldsymbol{j}}(t) \\ \boldsymbol{v}_{\mathrm{R},\boldsymbol{j}}(t)\,\widehat{\mathbf{R}} + \boldsymbol{v}_{\phi,\boldsymbol{j}}(t)\,\widehat{\boldsymbol{\phi}} + \boldsymbol{v}_{\mathrm{Z},\boldsymbol{j}}(t)\,\widehat{\mathbf{Z}} \\ T_{\boldsymbol{j}}(t) \\ \mathbf{A}_{\mathrm{R},\boldsymbol{j}}(t)\,\widehat{\mathbf{R}} + \psi_{\boldsymbol{j}}(t)\,\nabla\phi + \mathbf{A}_{\mathrm{Z},\boldsymbol{j}}(t)\,\widehat{\mathbf{Z}} \end{pmatrix}.$$

The presentation will be simpler if the vector is identified to its components

$$\mathbf{Y}_{\boldsymbol{j}} \equiv (\rho_{\boldsymbol{j}},\ \boldsymbol{v}_{\mathrm{R},\boldsymbol{j}},\ \boldsymbol{v}_{\phi,\boldsymbol{j}},\ \boldsymbol{v}_{\mathrm{Z},\boldsymbol{j}},\ T_{\boldsymbol{j}},\ \mathbf{A}_{\mathrm{R},\boldsymbol{j}},\ \psi_{\boldsymbol{j}},\ \mathbf{A}_{\mathrm{Z},\boldsymbol{j}})^{\mathrm{T}}.$$

Semi-discrete system. The evolution of $\mathbf{Y}_{\boldsymbol{j}}$ is obtained through projections formulated in equation (3.11), according to the vector test functions defined in (3.14). The system of discrete equations is written as

$$\begin{aligned}
\sum_{\boldsymbol{j}} \int_{\boldsymbol{\Omega}_{x,h}} \underline{\mathbf{M}}_{\boldsymbol{ij}}(\underline{\mathbf{Y}}) \frac{\partial \mathbf{Y}_{\boldsymbol{j}}}{\partial t} - \int_{\boldsymbol{\Omega}_{x,h}} \boldsymbol{\Phi}^{\mathbf{F}}_{\boldsymbol{i}}(\underline{\mathbf{Y}}) + \int_{\boldsymbol{\Omega}_{x,h}} \boldsymbol{\Phi}^{\mathbf{D}}_{\boldsymbol{i}}(\underline{\mathbf{Y}}) + \int_{\boldsymbol{\Omega}_{x,h}} \boldsymbol{\Phi}^{\mathbf{F},\mathrm{R}\phi}_{\boldsymbol{i}}(\underline{\mathbf{Y}}) - \int_{\boldsymbol{\Omega}_{x,h}} \boldsymbol{\Phi}^{\mathbf{D},\mathrm{R}\phi}_{\boldsymbol{i}}(\underline{\mathbf{Y}}) + \frac{1}{\varepsilon}\int_{\boldsymbol{\Omega}_{x,h}} \boldsymbol{\Phi}^{\mathbf{A}}_{\boldsymbol{i}}(\underline{\mathbf{Y}}) \\
+ \int_{\partial\boldsymbol{\Omega}_{x,h}} \boldsymbol{\Psi}^{\mathbf{F}}_{\boldsymbol{i}}(\underline{\mathbf{Y}}) - \int_{\partial\boldsymbol{\Omega}_{x,h}} \boldsymbol{\Psi}^{\mathbf{D}}_{\boldsymbol{i}}(\underline{\mathbf{Y}}) + \frac{1}{\varepsilon}\int_{\partial\boldsymbol{\Omega}_{x,h}} \boldsymbol{\Psi}^{\partial_t\mathbf{A}}_{\boldsymbol{i}}(\underline{\mathbf{Y}}) + \frac{1}{\varepsilon}\int_{\partial\boldsymbol{\Omega}_{x,h}} \boldsymbol{\Psi}^{\mathbf{S}}_{\boldsymbol{i}}(\underline{\mathbf{Y}}) = -\int_{\boldsymbol{\Omega}_{x,h}} \boldsymbol{\Phi}^{\mathrm{VMS}}_{\boldsymbol{i}}(\overline{\underline{\mathbf{Y}}}, \delta\underline{\mathbf{Y}}),
\end{aligned} \tag{3.16}$$

where the non-integrated mass matrix $\underline{\mathbf{M}}_{\boldsymbol{ij}}(\underline{\mathbf{Y}}) = \mathcal{N}_{\boldsymbol{i}}\mathcal{N}_{\boldsymbol{j}}\underline{\mathbf{M}}(\underline{\mathbf{Y}})$ is not diagonal and varies with the interpolated variable $\mathbf{Y}$. The large vector $\underline{\mathbf{Y}}$ contains all the unknowns vectors $\mathbf{Y}_{\boldsymbol{j}}$ defining the interpolation. The fluxes are

$$\boldsymbol{\Phi}^{\mathbf{F}}_{\boldsymbol{i}}(\underline{\mathbf{Y}}) = \begin{pmatrix} \rho(\boldsymbol{v}\cdot\nabla\mathcal{N}_{\boldsymbol{i}}) \\ \rho\boldsymbol{v}(\boldsymbol{v}\cdot\nabla\mathcal{N}_{\boldsymbol{i}}) + \mathrm{P}\nabla\mathcal{N}_{\boldsymbol{i}} - \mathbf{B}(\mathbf{B}\cdot\nabla\mathcal{N}_{\boldsymbol{i}}) \\ \rho\mathcal{H}(\boldsymbol{v}\cdot\nabla\mathcal{N}_{\boldsymbol{i}}) - \mathbf{B}\cdot\boldsymbol{v}(\mathbf{B}\cdot\nabla\mathcal{N}_{\boldsymbol{i}}) \\ -(\boldsymbol{v}\times\mathbf{B})\mathcal{N}_{\boldsymbol{i}} \end{pmatrix}, \quad \boldsymbol{\Phi}^{\mathbf{D}}_{\boldsymbol{i}}(\underline{\mathbf{Y}}) = \begin{pmatrix} (\underline{\boldsymbol{D}}\boldsymbol{\partial}\rho')\cdot\nabla\mathcal{N}_{\boldsymbol{i}} \\ \underline{\boldsymbol{\tau}}\nabla\mathcal{N}_{\boldsymbol{i}} \\ (\underline{\boldsymbol{\tau}}\boldsymbol{v})\cdot\nabla\mathcal{N}_{\boldsymbol{i}} \\ -(\mathbf{E}+\boldsymbol{v}\times\mathbf{B})\mathcal{N}_{\boldsymbol{i}} \end{pmatrix}.$$

For resistive MHD we have $\mathbf{E} + \boldsymbol{v} \times \mathbf{B} = \underline{\boldsymbol{\eta}}\mathbf{J} = \underline{\boldsymbol{\eta}}\nabla \times \mathbf{B}$. Then, as $\mathbf{B} = \nabla \times \mathbf{A}$ with $\mathbf{A}$ the interpolated variable, the computation of $\mathbf{J}$ involves second order derivatives. This can be avoided by using integration by parts with an additional contribution at the boundary. The contribution associated to $\boldsymbol{\Phi}^{\mathbf{F}}_{\boldsymbol{i}}$ and $\boldsymbol{\Phi}^{\mathbf{D}}_{\boldsymbol{i}}$ does not take into account the fact that $\widehat{\mathbf{R}}$ and $\widehat{\boldsymbol{\phi}}$ vary in the polar plane. The spatial variation of $\widehat{\mathbf{R}}$ and $\widehat{\boldsymbol{\phi}}$ contributes to the fluxes $\boldsymbol{\Phi}^{\mathbf{F},\mathrm{R}\phi}_{\boldsymbol{i}}$ and $\boldsymbol{\Phi}^{\mathbf{D},\mathrm{R}\phi}_{\boldsymbol{i}}$:

$$\boldsymbol{\Phi}^{\mathbf{F},\mathrm{R}\phi}_{\boldsymbol{i}}(\underline{\mathbf{Y}}) = \frac{\mathcal{N}_{\boldsymbol{i}}}{\mathrm{R}} \begin{pmatrix} 0 \\ \left(\rho \boldsymbol{v}_{\phi}^2 + \mathrm{P} - \mathbf{B}_{\phi}^2\right)\widehat{\mathbf{R}} - \left(\rho \boldsymbol{v}_{\mathrm{R}} \boldsymbol{v}_{\phi} - \mathbf{B}_{\mathrm{R}}\mathbf{B}_{\phi}\right)\widehat{\boldsymbol{\phi}} \\ 0 \\ 0 \end{pmatrix},$$

$$\boldsymbol{\Phi}^{\mathbf{D},\mathrm{R}\phi}_{\boldsymbol{i}}(\underline{\mathbf{Y}}) = \frac{\mathcal{N}_{\boldsymbol{i}}}{\mathrm{R}} \begin{pmatrix} 0 \\ \left(\underline{\boldsymbol{\tau}} : \left(\widehat{\boldsymbol{\phi}} \otimes \widehat{\boldsymbol{\phi}}\right)\right)\widehat{\mathbf{R}} - \left(\underline{\boldsymbol{\tau}} : \left(\widehat{\mathbf{R}} \otimes \widehat{\boldsymbol{\phi}}\right)\right)\widehat{\boldsymbol{\phi}} \\ 0 \\ 0 \end{pmatrix}.$$

Enforcing the Coulomb gauge condition by penalization, when the approximation space for the vector potential is not divergence free, leads to

$$\boldsymbol{\Phi}^{\mathbf{A}}_{\boldsymbol{i}}(\underline{\mathbf{Y}}) = \begin{pmatrix} 0 \\ 0 \\ 0 \\ \nabla \cdot \mathbf{A}\left(\left(\partial_{\mathrm{R}}\mathcal{N}_{\boldsymbol{i}} + \frac{\mathcal{N}_{\boldsymbol{i}}}{\mathrm{R}}\right)\widehat{\mathbf{R}} + \frac{\partial_{\phi}\mathcal{N}_{\boldsymbol{i}}}{\mathrm{R}}\widehat{\boldsymbol{\phi}} + \partial_{\mathrm{Z}}\mathcal{N}_{\boldsymbol{i}}\widehat{\mathbf{Z}}\right) \end{pmatrix},$$

where we have used the relations $\nabla \cdot \widehat{\mathbf{R}} = \frac{1}{\mathrm{R}}$ and $\nabla \cdot \widehat{\boldsymbol{\phi}} = 0$. In order to get simple formulations for the boundary fluxes, the fluxes $\boldsymbol{\Phi}^{\mathbf{F}}_{\boldsymbol{i}}(\underline{\mathbf{Y}})$ and $\boldsymbol{\Phi}^{\mathbf{D}}_{\boldsymbol{i}}(\underline{\mathbf{Y}})$ are reformulated as functions of the state $\underline{\mathbf{Y}}$, the gradient vector $\nabla\mathcal{N}_{\boldsymbol{i}}$ and the scalar $\mathcal{N}_{\boldsymbol{i}}$

$$\boldsymbol{\Phi}^{\mathbf{F}}_{\boldsymbol{i}}(\underline{\mathbf{Y}}) = \boldsymbol{\Phi}^{\mathbf{F}}(\underline{\mathbf{Y}}, \nabla\mathcal{N}_{\boldsymbol{i}}, \mathcal{N}_{\boldsymbol{i}}) \quad \text{and} \quad \boldsymbol{\Phi}^{\mathbf{D}}_{\boldsymbol{i}}(\underline{\mathbf{Y}}) = \boldsymbol{\Phi}^{\mathbf{D}}(\underline{\mathbf{Y}}, \nabla\mathcal{N}_{\boldsymbol{i}}, \mathcal{N}_{\boldsymbol{i}}).$$

Therefore, the associated boundary fluxes use the same functions where the gradient of the test function is replaced by a vector times the test function, which translates to

$$\boldsymbol{\Psi}^{\mathbf{F}}_{\boldsymbol{i}}(\underline{\mathbf{Y}}) = \boldsymbol{\Phi}^{\mathbf{F}}(\underline{\mathbf{Y}}, \mathcal{N}_{\boldsymbol{i}}\boldsymbol{n}, \mathcal{N}_{\boldsymbol{i}}) \quad \text{and} \quad \boldsymbol{\Psi}^{\mathbf{D}}_{\boldsymbol{i}}(\underline{\mathbf{Y}}) = \boldsymbol{\Phi}^{\mathbf{D}}(\underline{\mathbf{Y}}, \mathcal{N}_{\boldsymbol{i}}\boldsymbol{n}, \mathcal{N}_{\boldsymbol{i}}),$$

$\boldsymbol{n}$ being the outward unit normal at the boundary. The penalized Dirichlet conditions are associated to the boundary integral on $\boldsymbol{\Psi}^{\mathbf{S}}_{\boldsymbol{i}}$, where

$$\boldsymbol{\Psi}^{\mathbf{S}}_{\boldsymbol{i}} = \begin{pmatrix} (\rho - \rho_b)\mathcal{N}_{\boldsymbol{i}}\boldsymbol{\mathcal{X}}\left(\partial\boldsymbol{\Omega}^{\rho}_{x,h}\right) \\ \rho(\boldsymbol{v} - \boldsymbol{v}_b)\mathcal{N}_{\boldsymbol{i}}\boldsymbol{\mathcal{X}}\left(\partial\boldsymbol{\Omega}^{\boldsymbol{v}}_{x,h}\right) + (\rho\boldsymbol{v} - \boldsymbol{m}_b)\mathcal{N}_{\boldsymbol{i}}\boldsymbol{\mathcal{X}}\left(\partial\boldsymbol{\Omega}^{\boldsymbol{m}}_{x,h}\right) \\ \rho(T - T_b)\mathcal{N}_{\boldsymbol{i}}\boldsymbol{\mathcal{X}}\left(\partial\boldsymbol{\Omega}^{T}_{x,h}\right) + (p - p_b)\mathcal{N}_{\boldsymbol{i}}\boldsymbol{\mathcal{X}}\left(\partial\boldsymbol{\Omega}^{p}_{x,h}\right) \\ (\mathbf{A} - \mathbf{A}_b)\mathcal{N}_{\boldsymbol{i}}\boldsymbol{\mathcal{X}}\left(\partial\boldsymbol{\Omega}^{\mathbf{A}}_{x,h}\right) + (\mathbf{B} - \mathbf{B}_b)\mathcal{N}_{\boldsymbol{i}}\boldsymbol{\mathcal{X}}\left(\partial\boldsymbol{\Omega}^{\mathbf{B}}_{x,h}\right) \end{pmatrix}.$$

The formulation with potential vector produces a boundary contribution associated to the time derivative of $\mathbf{A}$. When the degree of freedom associated to the index $\boldsymbol{i}$ is on the boundary we have

$$\boldsymbol{\Psi}^{\partial_t\mathbf{A}}_{\boldsymbol{i}}(\underline{\mathbf{Y}}) = \begin{pmatrix} 0 \\ 0 \\ 0 \\ \boldsymbol{n} \cdot \left(\partial_t\mathbf{A} \times \widehat{\mathbf{R}}\right)\mathcal{N}_{\boldsymbol{i}}\widehat{\mathbf{R}} + \boldsymbol{n} \cdot \left(\partial_t\mathbf{A} \times \widehat{\boldsymbol{\phi}}\right)\mathcal{N}_{\boldsymbol{i}}\widehat{\boldsymbol{\phi}} + \boldsymbol{n} \cdot \left(\partial_t\mathbf{A} \times \widehat{\mathbf{Z}}\right)\mathcal{N}_{\boldsymbol{i}}\widehat{\mathbf{Z}} \end{pmatrix}.$$

Finally, the stabilization is defined as

$$\boldsymbol{\Phi}_{\boldsymbol{i}}^{\text{VMS}}\left(\overline{\underline{\mathbf{Y}}},\delta\underline{\mathbf{Y}}\right)=\left(\begin{array}{c}\underline{\mathbf{L}}\left(\overline{\boldsymbol{w}},\boldsymbol{\partial}\right)\delta\boldsymbol{w}\cdot\underline{\mathbf{L}}^{\mathrm{T}}\left(\overline{\boldsymbol{w}},\boldsymbol{\partial}\right)\boldsymbol{w}_{\rho,\boldsymbol{i}}^{\star}\\ \hline \left(\underline{\mathbf{L}}\left(\overline{\boldsymbol{w}},\boldsymbol{\partial}\right)\delta\boldsymbol{w}\cdot\underline{\mathbf{L}}^{\mathrm{T}}\left(\overline{\boldsymbol{w}},\boldsymbol{\partial}\right)\boldsymbol{w}_{\boldsymbol{v}_{\mathrm{R}},\boldsymbol{i}}^{\star}\right)\widehat{\mathbf{R}}+\left(\underline{\mathbf{L}}\left(\overline{\boldsymbol{w}},\boldsymbol{\partial}\right)\delta\boldsymbol{w}\cdot\underline{\mathbf{L}}^{\mathrm{T}}\left(\overline{\boldsymbol{w}},\boldsymbol{\partial}\right)\boldsymbol{w}_{\boldsymbol{v}_{\phi},\boldsymbol{i}}^{\star}\right)\widehat{\boldsymbol{\phi}}\\ +\left(\underline{\mathbf{L}}\left(\overline{\boldsymbol{w}},\boldsymbol{\partial}\right)\delta\boldsymbol{w}\cdot\underline{\mathbf{L}}^{\mathrm{T}}\left(\overline{\boldsymbol{w}},\boldsymbol{\partial}\right)\boldsymbol{w}_{\boldsymbol{v}_{\mathrm{Z}},\boldsymbol{i}}^{\star}\right)\widehat{\mathbf{Z}}\\ \hline \underline{\mathbf{L}}\left(\overline{\boldsymbol{w}},\boldsymbol{\partial}\right)\delta\boldsymbol{w}\cdot\underline{\mathbf{L}}^{\mathrm{T}}\left(\overline{\boldsymbol{w}},\boldsymbol{\partial}\right)\boldsymbol{w}_{\mathcal{E},\boldsymbol{i}}^{\star}\\ \hline \left(\underline{\mathbf{L}}\left(\overline{\boldsymbol{w}},\boldsymbol{\partial}\right)\delta\boldsymbol{w}\cdot\underline{\mathbf{L}}^{\mathrm{T}}\left(\overline{\boldsymbol{w}},\boldsymbol{\partial}\right)\boldsymbol{w}_{\mathbf{A}_{\mathrm{R}},\boldsymbol{i}}^{\star}\right)\widehat{\mathbf{R}}+\left(\underline{\mathbf{L}}\left(\overline{\boldsymbol{w}},\boldsymbol{\partial}\right)\delta\boldsymbol{w}\cdot\underline{\mathbf{L}}^{\mathrm{T}}\left(\overline{\boldsymbol{w}},\boldsymbol{\partial}\right)\boldsymbol{w}_{\mathbf{A}_{\phi},\boldsymbol{i}}^{\star}\right)\widehat{\boldsymbol{\phi}}\\ +\left(\underline{\mathbf{L}}\left(\overline{\boldsymbol{w}},\boldsymbol{\partial}\right)\delta\boldsymbol{w}\cdot\underline{\mathbf{L}}^{\mathrm{T}}\left(\overline{\boldsymbol{w}},\boldsymbol{\partial}\right)\boldsymbol{w}_{\mathbf{A}_{\mathrm{Z}},\boldsymbol{i}}^{\star}\right)\widehat{\mathbf{Z}}\end{array}\right),$$

where the fluctuation approximated by the variation in the current time step and the fluctuation $\delta\boldsymbol{w}$ linked to $\delta\underline{\mathbf{Y}}$ by the matrix $\underline{\mathbf{M}}\left(\overline{\underline{\mathbf{Y}}}\right)$ evaluated at the beginning of the time step are

$$\delta\underline{\mathbf{Y}}\simeq\underline{\mathbf{Y}}^{n+1}-\underline{\mathbf{Y}}^{n}\quad\text{and}\quad\delta\boldsymbol{w}\simeq\underline{\mathbf{M}}\left(\overline{\underline{\mathbf{Y}}}\right)\delta\underline{\mathbf{Y}}.\tag{3.17}$$

Let us recall that we have used the following approximation of the residual $\mathbf{R}\left(\boldsymbol{w}\right)\simeq\underline{\mathbf{L}}\left(\overline{\boldsymbol{w}},\boldsymbol{\partial}\right)\delta\boldsymbol{w}$.

Discretization in the poloidal plane. The poloidal discretization is achieved by a 2D finite element basis. We will use the 2D Bezier finite element basis, proposed in [13], defined on the square with the local coordinates $\boldsymbol{\zeta}=(\mathrm{s},\mathrm{T})$. Then, a nonlinear transformation is used to map the square to any curved element of the physical space. For a given element $\boldsymbol{e}$ the transformation is defined as

$$\left\{\begin{array}{lcl}\mathrm{R}_{\boldsymbol{e}}\left(\boldsymbol{\zeta}\right) & = & \displaystyle\sum_{j_{2\mathrm{D}}\in\vartheta(\boldsymbol{e})}\mathrm{R}_{j_{2\mathrm{D}}}\widehat{\psi}_{m_{\boldsymbol{e}}(j_{2\mathrm{D}})}\left(\boldsymbol{\zeta}\right)\\ \mathrm{Z}_{\boldsymbol{e}}\left(\boldsymbol{\zeta}\right) & = & \displaystyle\sum_{j_{2\mathrm{D}}\in\vartheta(\boldsymbol{e})}\mathrm{Z}_{j_{2\mathrm{D}}}\widehat{\psi}_{m_{\boldsymbol{e}}(j_{2\mathrm{D}})}\left(\boldsymbol{\zeta}\right)\end{array}\right..$$

The parameters $\mathrm{R}_{j_{2\mathrm{D}}}$ and $\mathrm{Z}_{j_{2\mathrm{D}}}$ of this interpolation are inputs of the MHD computation. They are designed by the meshing process to ensure that the transformation is nonsingular (injection) and that the mapped element in the physical space can be curved. This allows the mesh to be aligned either with the curved boundary or the flux surfaces given by the initial equilibrium. The function $m_{\boldsymbol{e}}(j_{2\mathrm{D}})$ changes the global numbering $(j_{2\mathrm{D}})$ to a local numbering in the set $\left\{1,\cdots,\widehat{N}_{dof}\right\}$ where $\widehat{N}_{dof}$ is the number of unknowns associated to the reference element. In the present context of the bi-cubic interpolation over square, we have $\widehat{N}_{dof}=16$. However, contrary to the classical cubic Bezier, the unknowns of the current basis are located at the vertices of the square such as to ensure the C^1 continuity when crossing the edges of physical elements. This localization of the unknowns also allows the derivation of the compressed numerical graph, useful for computational efficiency.

Time stepping. The presentation of the time integrator will be easier with the introduction of the following block matrix $\underline{\mathbb{A}}^{\delta t}$, a block stabilization vector $\underline{\mathbf{VMS}}$ and a block right-hand side $\underline{\mathbf{RHS}}$, with their corresponding components:

$$\underline{\mathbb{A}}_{\boldsymbol{ij}}^{\delta t}\left(\underline{\mathbf{Y}}\right)=\int_{\boldsymbol{\Omega}_{x,h}}\underline{\mathbf{M}}_{\boldsymbol{ij}}\left(\underline{\mathbf{Y}}\right),\qquad\underline{\mathbf{VMS}}_{\boldsymbol{i}}\left(\overline{\underline{\mathbf{Y}}},\delta\underline{\mathbf{Y}}\right)=\int_{\boldsymbol{\Omega}_{x,h}}\boldsymbol{\Phi}_{\boldsymbol{i}}^{\text{VMS}}\left(\overline{\underline{\mathbf{Y}}},\delta\underline{\mathbf{Y}}\right)$$

and

$$\begin{aligned}\underline{\mathbf{RHS}}_{\boldsymbol{i}}\left(\underline{\mathbf{Y}}\right)\;=\;&\int_{\boldsymbol{\Omega}_{x,h}}\boldsymbol{\Phi}_{\boldsymbol{i}}^{\mathbf{F}}\left(\underline{\mathbf{Y}}\right)-\int_{\boldsymbol{\Omega}_{x,h}}\boldsymbol{\Phi}_{\boldsymbol{i}}^{\mathbf{D}}\left(\underline{\mathbf{Y}}\right)-\int_{\boldsymbol{\Omega}_{x,h}}\boldsymbol{\Phi}_{\boldsymbol{i}}^{\mathbf{F},\mathrm{R}\phi}\left(\underline{\mathbf{Y}}\right)+\int_{\boldsymbol{\Omega}_{x,h}}\boldsymbol{\Phi}_{\boldsymbol{i}}^{\mathbf{D},\mathrm{R}\phi}\left(\underline{\mathbf{Y}}\right)-\frac{1}{\varepsilon}\int_{\boldsymbol{\Omega}_{x,h}}\boldsymbol{\Phi}_{\boldsymbol{i}}^{\mathbf{A}}\left(\underline{\mathbf{Y}}\right)\\ &-\int_{\partial\boldsymbol{\Omega}_{x,h}}\boldsymbol{\Psi}_{\boldsymbol{i}}^{\mathbf{F}}\left(\underline{\mathbf{Y}}\right)+\int_{\partial\boldsymbol{\Omega}_{x,h}}\boldsymbol{\Psi}_{\boldsymbol{i}}^{\mathbf{D}}\left(\underline{\mathbf{Y}}\right)-\frac{1}{\varepsilon}\int_{\partial\boldsymbol{\Omega}_{x,h}}\boldsymbol{\Psi}_{\boldsymbol{i}}^{\partial_t\mathbf{A}}\left(\underline{\mathbf{Y}}\right)-\frac{1}{\varepsilon}\int_{\partial\boldsymbol{\Omega}_{x,h}}\boldsymbol{\Psi}_{\boldsymbol{i}}^{\mathbf{S}}\left(\underline{\mathbf{Y}}\right)\end{aligned}$$

. The equation (3.16) is then a nonlinear system that can be written as

$$\underline{\mathbb{A}}^{\delta t}\left(\underline{\mathbf{Y}}\right)\frac{\partial \underline{\mathbf{Y}}}{\partial t}+\underline{\mathbf{VMS}}\left(\overline{\underline{\mathbf{Y}}},\delta\underline{\mathbf{Y}}\right)=\underline{\mathbf{RHS}}\left(\underline{\mathbf{Y}}\right). \tag{3.18}$$

According to the stabilization process used, the fluctuation $\delta\underline{\mathbf{Y}}$ can be formulated in terms of the time derivative $\frac{\partial \underline{\mathbf{Y}}}{\partial t}$. Therefore, the one-step and two-step schemes can be written in the following general form

$$\begin{aligned}(1+\beta)\frac{\underline{\mathbb{A}}^{\delta t}\left(\underline{\mathbf{Y}}^{n+1}\right)\underline{\mathbf{Y}}^{n+1}-\underline{\mathbb{A}}^{\delta t}\left(\underline{\mathbf{Y}}^{n}\right)\underline{\mathbf{Y}}^{n}}{\delta t}&+\underline{\mathbf{VMS}}\left(\underline{\mathbf{Y}}^{n},\delta\underline{\mathbf{Y}}\right)-\theta\underline{\mathbf{RHS}}\left(\underline{\mathbf{Y}}^{n}+\delta\underline{\mathbf{Y}}\right)\\ =-\beta\frac{\underline{\mathbb{A}}^{\delta t}\left(\underline{\mathbf{Y}}^{n}\right)\underline{\mathbf{Y}}^{n}-\underline{\mathbb{A}}^{\delta t}\left(\underline{\mathbf{Y}}^{n-1}\right)\underline{\mathbf{Y}}^{n-1}}{\delta t^{n}}&+\left(1-\theta+\zeta\right)\underline{\mathbf{RHS}}\left(\underline{\mathbf{Y}}^{n}\right)-\zeta\underline{\mathbf{RHS}}\left(\underline{\mathbf{Y}}^{n-1}\right),\end{aligned} \tag{3.19}$$

where $\delta t=t^{n+1}-t^{n}$ and $\delta t^{n}=t^{n}-t^{n-1}$ are respectively the current and the previous time steps, $\delta\underline{\mathbf{Y}}\equiv\underline{\mathbf{Y}}^{n+1}-\underline{\mathbf{Y}}^{n}$ and $\delta\underline{\mathbf{Y}}^{n}\equiv\underline{\mathbf{Y}}^{n}-\underline{\mathbf{Y}}^{n-1}$ the fluctuations during, respectively, the current and the previous time steps, respectively. The above scheme includes the θ-schemes for $\beta=\zeta=0$. The θ-schemes are for $\theta=0$ the forward Euler, $\theta=1$ the backward Euler and $\theta=1/2$ the Crank-Nicholson scheme. Different combinations can be used to recover some second order temporal schemes (one- and two-step) that are A-stables. Note that, the proposed VMS-stabilization is related to the Taylor-Galerkin formulation and always contains an implicit contribution. Therefore, the forward Euler approximation is no more an explicit scheme. We can say that it is an implicit stabilization of the forward Euler scheme. In the community of magnetically confined plasma, "implicit schemes" are often used for implicit VMS-stabilization [30]; consequently, there is confusion between implicit VMS-stabilization and implicit scheme for the other contributions. For instance, the well known "Semi-implicit" schemes (see [30]) are Euler forward schemes where it is assumed that only fluctuations of the velocity are important for the stabilization. Moreover, we use in the equation (3.19) the approximation $\underline{\mathbb{A}}^{\delta t}\left(\underline{\mathbf{Y}}^{n+1}\right)\simeq\underline{\mathbb{A}}^{\delta t}\left(\underline{\mathbf{Y}}^{n}\right)$. Then

$$\underline{\mathbf{M}}_{\rho,\rho}\frac{\delta\underline{\boldsymbol{\rho}}}{\delta t}+\widetilde{\underline{\mathbf{VMS}}}^{\rho}\left(\underline{\mathbf{Y}}^{n},\delta\boldsymbol{v}\right)=\underline{\mathbf{RHS}}^{\rho}\left(\underline{\mathbf{Y}}^{n}\right), \tag{3.20}$$

$$\underline{\mathbf{M}}^{n}_{\boldsymbol{v},\rho}\frac{\delta\underline{\boldsymbol{\rho}}}{\delta t}+\underline{\mathbf{M}}^{n}_{\boldsymbol{v},\boldsymbol{v}}\frac{\delta\underline{\boldsymbol{v}}}{\delta t}+\widetilde{\underline{\mathbf{VMS}}}^{\boldsymbol{m}}\left(\underline{\mathbf{Y}}^{n},\delta\boldsymbol{v}\right)=\underline{\mathbf{RHS}}^{\boldsymbol{m}}\left(\underline{\mathbf{Y}}^{n}\right), \tag{3.21}$$

$$\underline{\mathbf{M}}^{n}_{T,\rho}\frac{\delta\underline{\boldsymbol{\rho}}}{\delta t}+\underline{\mathbf{M}}^{n}_{T,\boldsymbol{v}}\frac{\delta\underline{\boldsymbol{v}}}{\delta t}+\underline{\mathbf{M}}^{n}_{T,T}\frac{\delta\underline{\boldsymbol{T}}}{\delta t}+\underline{\mathbf{M}}^{n}_{T,\mathbf{A}}\frac{\delta\underline{\mathbf{A}}}{\delta t}+\widetilde{\underline{\mathbf{VMS}}}^{\mathcal{E}}\left(\underline{\mathbf{Y}}^{n},\delta\boldsymbol{v}\right)=\underline{\mathbf{RHS}}^{\mathcal{E}}\left(\underline{\mathbf{Y}}^{n}\right), \tag{3.22}$$

$$\underline{\mathbf{M}}_{\mathbf{A},\mathbf{A}}\frac{\delta\underline{\mathbf{A}}}{\delta t}+\widetilde{\underline{\mathbf{VMS}}}^{\mathbf{A}}\left(\underline{\mathbf{Y}}^{n},\delta\boldsymbol{v}\right)=\underline{\mathbf{RHS}}^{\mathbf{A}}\left(\underline{\mathbf{Y}}^{n}\right), \tag{3.23}$$

where the $\underline{\mathbf{M}}_{\cdot,\cdot}$ are sub-matrices of the mass matrix $\underline{\mathbb{A}}^{\delta t}\left(\underline{\mathbf{Y}}^{n}\right)$. A superscript is used to point out the dependency to $\underline{\mathbf{Y}}^{n}$. The first two equations are decoupled from the remaining equations. This is a sub-system of size $4N_{i_{2\mathrm{D}}}N_{i_{\phi}}$, for the density and the velocity fluctuations. It is half the size of the global system. Further assumptions can be used to neglect the influence of density fluctuations on the velocity fluctuation and obtain, for $\delta\underline{\boldsymbol{v}}$, a reduced system of size $3N_{i_{2\mathrm{D}}}N_{i_{\phi}}$. When $\delta\underline{\boldsymbol{v}}$ is updated, the remaining equations can be solved individually. The resolution is simpler if $\delta\underline{\boldsymbol{\rho}}$ and $\delta\underline{\mathbf{A}}$ are updated before $\delta\underline{\boldsymbol{T}}$. When only the fluctuation of the velocity is considered we have

$$\underline{\mathbf{L}}\left(\boldsymbol{w},\boldsymbol{\partial}\right)\delta\boldsymbol{w}\simeq\begin{pmatrix}\rho\boldsymbol{\partial}\cdot\delta\boldsymbol{v}\\ \hline \boldsymbol{m}\boldsymbol{\partial}\cdot\delta\boldsymbol{v}+\boldsymbol{m}\cdot\boldsymbol{\partial}\delta\boldsymbol{v}+\frac{\rho}{1-\gamma}\left(\boldsymbol{\partial}\delta\boldsymbol{v}\right)\boldsymbol{v}\\ \hline \rho\left(1-\gamma\right)\left(\boldsymbol{v}\otimes\boldsymbol{v}\right):\boldsymbol{\partial}\delta\boldsymbol{v}+\rho\mathcal{H}\boldsymbol{\partial}\cdot\delta\boldsymbol{v}+\left(\mathbf{B}\otimes\mathbf{B}\right):\boldsymbol{\partial}\delta\boldsymbol{v}\\ \hline \mathbf{B}\boldsymbol{\partial}\cdot\delta\boldsymbol{v}-\mathbf{B}\cdot\boldsymbol{\partial}\delta\boldsymbol{v}\end{pmatrix}$$

and

$$\underline{\mathbf{L}}^{\mathrm{T}}(\boldsymbol{w},\boldsymbol{\partial})\,\boldsymbol{w}_{\boldsymbol{m}}^{\star}=\left(\begin{array}{c}-(\boldsymbol{v}\otimes\boldsymbol{v}):\boldsymbol{\partial}\boldsymbol{m}^{\star}+\frac{(\gamma-1)\boldsymbol{v}\cdot\boldsymbol{v}}{2}\boldsymbol{\partial}\cdot\boldsymbol{m}^{\star}\\ \hline (\boldsymbol{\partial}\boldsymbol{m}^{\star})\,\boldsymbol{v}+\boldsymbol{v}\cdot\boldsymbol{\partial}\boldsymbol{m}^{\star}-(\gamma-1)\,\boldsymbol{v}\boldsymbol{\partial}\cdot\boldsymbol{m}^{\star}\\ \hline (\gamma-1)\,\boldsymbol{\partial}\cdot\boldsymbol{m}^{\star}\\ \hline (2-\gamma)\,\mathbf{B}\boldsymbol{\partial}\cdot\boldsymbol{m}^{\star}-(\boldsymbol{\partial}\boldsymbol{m}^{\star})\,\mathbf{B}-\mathbf{B}\cdot\boldsymbol{\partial}\boldsymbol{m}^{\star}\end{array}\right),\quad \underline{\mathbf{L}}^{\mathrm{T}}(\boldsymbol{w},\boldsymbol{\partial})\,\boldsymbol{w}_{\rho}^{\star}=\left(\begin{array}{c}O\\ \boldsymbol{\partial}\rho^{\star}\\ 0\\ 0\end{array}\right).$$

In the sequel, we consider further simplifications by retaining only contributions that are in divergence form. This can be viewed as retaining only some compressibility effects (acoustic waves) for stabilization. Then, the VMS stabilization associated to the momentum equation becomes

$$\underline{\mathbf{L}}(\boldsymbol{w},\boldsymbol{\partial})\,\delta\boldsymbol{w}\cdot\underline{\mathbf{L}}^{\mathrm{T}}(\boldsymbol{w},\boldsymbol{\partial})\,\boldsymbol{w}_{\boldsymbol{m}}^{\star}\simeq(\gamma-1)\left(\rho\frac{\boldsymbol{v}\cdot\boldsymbol{v}}{2}-\rho\boldsymbol{v}\cdot\boldsymbol{v}+\rho\mathcal{H}+\frac{2-\gamma}{\gamma-1}\mathbf{B}\cdot\mathbf{B}\right)(\boldsymbol{\partial}\cdot\delta\boldsymbol{v})\,(\boldsymbol{\partial}\cdot\boldsymbol{m}^{\star}).$$

Thus, as $\mathcal{H}=\frac{\gamma\mathrm{P}}{\rho(\gamma-1)}+\frac{\boldsymbol{v}\cdot\boldsymbol{v}}{2}-\frac{2-2\gamma}{2\rho(\gamma-1)}\mathbf{B}\cdot\mathbf{B}=\frac{\gamma p}{\rho(\gamma-1)}+\frac{\boldsymbol{v}\cdot\boldsymbol{v}}{2}+\frac{(\gamma-1)\mathbf{B}\cdot\mathbf{B}}{\rho(\gamma-1)}$, we obtain

$$\underline{\mathbf{L}}(\boldsymbol{w},\boldsymbol{\partial})\,\delta\boldsymbol{w}\cdot\underline{\mathbf{L}}^{\mathrm{T}}(\boldsymbol{w},\boldsymbol{\partial})\,\boldsymbol{w}_{\boldsymbol{m}}^{\star}\simeq(\gamma p+\mathbf{B}\cdot\mathbf{B})\,(\boldsymbol{\partial}\cdot\delta\boldsymbol{v})\,(\boldsymbol{\partial}\cdot\boldsymbol{m}^{\star}),\tag{3.24}$$

when divided by the density, we recover the weak form of the so called "Ideal MHD operator" $\mathcal{G}(\boldsymbol{w},\boldsymbol{\partial})$:

$$\mathcal{G}(\boldsymbol{w},\boldsymbol{\partial})=\boldsymbol{\partial}\left(\frac{\gamma p}{\rho}\boldsymbol{\partial}^{\mathrm{T}}\right)+(\mathbf{B}\otimes\boldsymbol{\partial})^{\mathrm{T}}\left(\frac{1}{\rho}\mathbf{B}\otimes\boldsymbol{\partial}\right).$$

However, when the time stepping uses $\theta\neq 0$, the system is fully coupled and there is no numerical advantage to use, in this case, reduced stabilization, except for the numerical implementation. In the general case with $\theta\neq 0$, the numerical scheme (3.19) is a nonlinear system that defined the fluctuation $\delta\underline{\mathbf{Y}}$. The nonlinear dependency is associated to $\underline{\mathbf{RHS}}\,(\underline{\mathbf{Y}}^{n}+\delta\underline{\mathbf{Y}})$. Indeed, the contribution associated to the time derivative and the VMS-stabilization are, by construction, linear. In any case, we need to compute block matrices $\underline{\mathbb{A}}^{\mathrm{VMS}}$ and $\underline{\mathbb{A}}^{\mathrm{RHS}}$ that are approximated Jacobians of $\underline{\mathbf{VMS}}$ and $\underline{\mathbf{RHS}}$ such that

$$\underline{\mathbf{VMS}}\,(\overline{\underline{\mathbf{Y}}},\delta\underline{\mathbf{Y}})=\underline{\mathbb{A}}^{\mathrm{VMS}}(\overline{\underline{\mathbf{Y}}})\delta\underline{\mathbf{Y}}\quad\text{and}\quad\underline{\mathbf{RHS}}\,(\overline{\underline{\mathbf{Y}}}+\delta\underline{\mathbf{Y}})\simeq\underline{\mathbf{RHS}}\,(\overline{\underline{\mathbf{Y}}})+\underline{\mathbb{A}}^{\mathrm{RHS}}(\overline{\underline{\mathbf{Y}}})\delta\underline{\mathbf{Y}}.$$

These matrices will be used during the Newton iterations to obtain the solution of the nonlinear equation. In many situations, the Newton step can be reduced to a single iteration. The single Newton iteration gives the linearized implicit schemes, written as

$$\underline{\mathbb{A}}\,(\underline{\mathbf{Y}}^{n},\overline{\underline{\mathbf{Y}}})\,\delta\underline{\mathbf{Y}}=-\beta\frac{\underline{\mathbb{A}}^{\delta t}(\underline{\mathbf{Y}}^{n})\,\underline{\mathbf{Y}}^{n}-\underline{\mathbb{A}}^{\delta t}\left(\underline{\mathbf{Y}}^{n-1}\right)\underline{\mathbf{Y}}^{n-1}}{\delta t^{n}}+(1-\theta+\zeta)\,\underline{\mathbf{RHS}}\,(\underline{\mathbf{Y}}^{n})-\zeta\underline{\mathbf{RHS}}\left(\underline{\mathbf{Y}}^{n-1}\right),\tag{3.25}$$

where the global matrix is defined as

$$\underline{\mathbb{A}}\,(\underline{\mathbf{Y}}^{n},\overline{\underline{\mathbf{Y}}})=\frac{1+\beta}{\delta t}\underline{\mathbb{A}}^{\delta t}(\underline{\mathbf{Y}}^{n})+\underline{\mathbb{A}}^{\mathrm{VMS}}(\underline{\mathbf{Y}}^{n})-\theta\,\underline{\mathbb{A}}^{\mathrm{RHS}}(\underline{\mathbf{Y}}^{n}).$$

Evaluation of integrals by quadrature. Once more, as the target applications are tokamak geometries, all the integrals to be evaluated in the equation (3.16) will be achieved according to the cylindrical transformation (3.12) and the parametric mapping. For any function $\boldsymbol{Y}$, the integral over the computational domain is approximated as a sum of integrals over poloidal elements and the local mapping used. The 2D integrals are evaluated by the Gauss quadrature.

When Fourier modes are used as basis functions in the toroidal direction, the toroidal integrals are evaluated by a Riemann sum with equidistant toroidal angles ϕ_{g_ϕ}.

$$\begin{aligned}\int_0^{2\pi}\sum_{\boldsymbol{e}_{2\mathrm{D}}}\int_{\boldsymbol{e}_{2\mathrm{D}}}\mathrm{R}\boldsymbol{Y}\left(\boldsymbol{\xi},\phi\right)d\boldsymbol{\xi}d\phi &= \int_0^{2\pi}\sum_{\boldsymbol{e}_{2\mathrm{D}}}\int_{-1}^{1}\int_{-1}^{1}\mathrm{R}\left(\boldsymbol{\zeta}\right)\boldsymbol{Y}\left(\boldsymbol{\xi}\left(\boldsymbol{\zeta}\right),\phi\right)\mathcal{J}_{\boldsymbol{e}_{2\mathrm{D}}}\left(\boldsymbol{\zeta}\right)d\boldsymbol{\zeta}d\phi\\ &\simeq \sum_{g_\phi=1}^{N_{g_\phi}}\frac{2\pi}{N_{g_\phi}}\sum_{\boldsymbol{e}_{2\mathrm{D}}}\sum_{g_{\mathrm{S}}=1}^{N_{g_{\mathrm{S}}}}\sum_{g_{\mathrm{T}}=1}^{N_{g_{\mathrm{S}}}}\omega_{g_{\mathrm{S}}}\omega_{g_{\mathrm{T}}}\mathrm{R}\left(\boldsymbol{\zeta}_{g_{2\mathrm{D}}}\right)\mathcal{J}_{\boldsymbol{e}_{2\mathrm{D}}}\left(\boldsymbol{\zeta}_{g_{2\mathrm{D}}}\right)\boldsymbol{Y}\left(\boldsymbol{\zeta}_{g_{2\mathrm{D}}},\phi_{g_\phi}\right),\end{aligned}$$

where $\omega_{g_{\mathrm{S}}}$ and $\omega_{g_{\mathrm{T}}}$ are Gauss weights and $\boldsymbol{\zeta}_{g_{2\mathrm{D}}}$ the associated sampling points. To make the equations a little less dense, we have used the equivalence $\boldsymbol{Y}\left(\boldsymbol{\zeta}_{g_{2\mathrm{D}}},\phi_{g_\phi}\right)\equiv\boldsymbol{Y}\left(\boldsymbol{\xi}\left(\boldsymbol{\zeta}_{g_{2\mathrm{D}}}\right),\phi_{g_\phi}\right)$. The Jacobian of the mapping $\mathcal{J}_{\boldsymbol{e}_{2\mathrm{D}}}\left(\boldsymbol{\zeta}\right)$ is obtained with the local derivatives:

$$\mathcal{J}_{\boldsymbol{e}_{2\mathrm{D}}}\left(\boldsymbol{\zeta}\right)=\partial_{\mathrm{S}}\mathrm{R}\partial_{\mathrm{T}}\mathrm{Z}-\partial_{\mathrm{T}}\mathrm{R}\partial_{\mathrm{S}}\mathrm{Z}.$$

When the modal decomposition is applied to the toroidal direction, we can always reformulate the functions to be integrated as follows:

$$\boldsymbol{Y}\left(\boldsymbol{\zeta},\phi\right)=\sum_{k=0}^{N_k}\boldsymbol{Y}_k^c\left(\boldsymbol{\zeta}\right)\cos\left(k\phi\right)+\sum_{k=0}^{N_k}\boldsymbol{Y}_k^s\left(\boldsymbol{\zeta}\right)\sin\left(k\phi\right).$$

This decomposition derives from the fact that the test functions are constructed as a toroidal function times a poloidal function. This property is preserved after the different spatial derivations. Therefore, we can speed-up the evaluation of integrals by the use of the fast Fourier transform (FFT). Indeed, in the context of modal decomposition, we can write the previous approximation as

$$\int_0^{2\pi}\sum_{\boldsymbol{e}_{2\mathrm{D}}}\int_{\boldsymbol{e}_{2\mathrm{D}}}\mathrm{R}\boldsymbol{Y}\left(\boldsymbol{\xi},\phi\right)d\boldsymbol{\xi}d\phi = \sum_{g_\phi=1}^{N_{g_\phi}}\frac{2\pi}{N_{g_\phi}}\sum_{k=0}^{N_k}\left\langle\boldsymbol{Y}_k^c\right\rangle_{2\mathrm{D}}\cos\left(k\phi\right)+\sum_{g_\phi=1}^{N_{g_\phi}}\frac{2\pi}{N_{g_\phi}}\sum_{k=1}^{N_k}\left\langle\boldsymbol{Y}_k^s\right\rangle_{2\mathrm{D}}\sin\left(k\phi\right),$$

where $\left\langle\boldsymbol{Y}_k\right\rangle_{2\mathrm{D}}$ is the numerical integral, of the function $\boldsymbol{Y}_k\left(\boldsymbol{\xi}\right)$, in the 2D poloidal plane. For example, for the function $\boldsymbol{Y}_k^c\left(\boldsymbol{\xi}\right)$, we have

$$\left\langle\boldsymbol{Y}_k^c\right\rangle_{2\mathrm{D}}=\sum_{\boldsymbol{e}_{2\mathrm{D}}}\sum_{g_{\mathrm{S}}=1}^{N_{g_{\mathrm{S}}}}\sum_{g_{\mathrm{T}}=1}^{N_{g_{\mathrm{S}}}}\omega_{g_{\mathrm{S}}}\omega_{g_{\mathrm{T}}}\mathrm{R}\left(\boldsymbol{\zeta}_{g_{2\mathrm{D}}}\right)\mathcal{J}_{\boldsymbol{e}_{2\mathrm{D}}}\left(\boldsymbol{\zeta}_{g_{2\mathrm{D}}}\right)\boldsymbol{Y}_k^c\left(\boldsymbol{\zeta}_{g_{2\mathrm{D}}}\right).$$

A similar decomposition holds for $\left\langle\boldsymbol{Y}_k^s\right\rangle_{2\mathrm{D}}$. This assembling based on FFT is carried out for the computation of the right-hand side (explicit) as well as for the computation of the global matrix. We just use, in the previous relations, the vector $\boldsymbol{Y}$ by the appropriated tensor.

Finally

$$\begin{aligned}\int_0^{2\pi}\int_{\boldsymbol{\Omega}_{2\mathrm{D}}}\mathrm{R}\boldsymbol{Y}\left(\boldsymbol{\xi},\phi\right)d\boldsymbol{\xi}d\phi &= \sum_{\boldsymbol{e}_\phi}\delta\phi_{\boldsymbol{e}_\phi}\int_{\widehat{\boldsymbol{e}_\phi}}\sum_{\boldsymbol{e}_{2\mathrm{D}}}\int_{\widehat{\boldsymbol{e}_{2\mathrm{D}}}}\mathrm{R}\left(\boldsymbol{\zeta}\right)\boldsymbol{Y}\left(\boldsymbol{\xi}\left(\boldsymbol{\zeta}\right),\phi\right)\mathcal{J}_{\boldsymbol{e}_{2\mathrm{D}}}\left(\boldsymbol{\zeta}\right)d\boldsymbol{\zeta}d\phi\\ &\simeq \sum_{\boldsymbol{e}_\phi}\sum_{g_\phi=1}^{N_{g_\phi}}\delta\phi_{\boldsymbol{e}_\phi}\omega_{g_\phi}\sum_{\boldsymbol{e}_{2\mathrm{D}}}\sum_{g_{2\mathrm{D}}=1}^{N_{g_{2\mathrm{D}}}}\omega_{g_{2\mathrm{D}}}\mathrm{R}\left(\boldsymbol{\zeta}_{g_{2\mathrm{D}}}\right)\mathcal{J}_{\boldsymbol{e}_{2\mathrm{D}}}\left(\boldsymbol{\zeta}_{g_{2\mathrm{D}}}\right)\boldsymbol{Y}\left(\boldsymbol{\zeta}_{g_{2\mathrm{D}}},\phi_{g_\phi}\right),\end{aligned}$$

where $\omega_{g_{\mathrm{S}}}$ and $\omega_{g_{\mathrm{T}}}$ are Gauss weights and $\boldsymbol{\zeta}_{g_{2\mathrm{D}}}$ the associated sampling points.

Boundary integrals can be associated to normal fluxes or Dirichlet penalty. In the first case we need an estimation of the normal in the physical space. According to the nonlinear mapping, this normal can vary at the boundary associated to a 2D mesh element. Such a boundary can be parametrized either by the reference coordinate S or T. More explicitly, when the boundary is parametrized with the reference coordinate S, we have

$$\mathrm{R}_{\ell_{2\mathrm{D}}}(\mathrm{S}) = \sum_{\boldsymbol{j}\in\vartheta(\ell_{2\mathrm{D}})} \mathrm{R}_{\boldsymbol{j}}\mathcal{N}_{\boldsymbol{j}}(\mathrm{S},\mathrm{T}^{\star}) \quad \text{and} \quad \mathrm{Z}_{\ell_{2\mathrm{D}}}(\mathrm{S}) = \sum_{\boldsymbol{j}\in\vartheta(\ell_{2\mathrm{D}})} \mathrm{Z}_{\boldsymbol{j}}\mathcal{N}_{\boldsymbol{j}}(\mathrm{S},\mathrm{T}^{\star}),$$

where $\ell_{2\mathrm{D}} = \partial\boldsymbol{e}_{2\mathrm{D}} \cap \partial\boldsymbol{\Omega}_{2\mathrm{D}} \neq \emptyset$, is used for any curved edge at the physical boundary associated to the 2D element $\boldsymbol{e}_{2\mathrm{D}}$. The parametrization is, in this case, associated to $\mathrm{T} = \mathrm{T}^{\star}$ where $\mathrm{T}^{\star}$ is either zero or one. Any infinitesimal length $d\ell$ of the physical boundary, will be written as

$$d\ell = \sqrt{(d\mathrm{R}(\mathrm{S}))^2 + (d\mathrm{Z}(\mathrm{S}))^2} = \left(\sqrt{(\partial_{\mathrm{S}}\mathrm{R})^2 + (\partial_{\mathrm{S}}\mathrm{Z})^2}\right) d\mathrm{S}.$$

Then the Jacobian of the boundary transformation is $\mathcal{J}_{\ell}(\mathrm{S}) = \sqrt{(\partial_{\mathrm{S}}\mathrm{R})^2 + (\partial_{\mathrm{S}}\mathrm{Z})^2}$. Therefore, for any function $\boldsymbol{\Psi}$, the boundary integral is written as

$$\begin{aligned}\int_{\partial\boldsymbol{\Omega}_{x,h}} \boldsymbol{\Psi}(\mathbf{Y}) &= \int_0^{2\pi} \mathrm{R}d\phi \int_{\partial\boldsymbol{\Omega}_{2\mathrm{D}}} \boldsymbol{\Psi}(\mathbf{Y})\, d\ell = \int_0^{2\pi} d\phi \sum_{\ell_{2\mathrm{D}}} \int_0^1 \mathrm{R}_{\ell_{2\mathrm{D}}}(\mathrm{S})\, \mathcal{J}_{\ell_{2\mathrm{D}}}(\mathrm{S})\, \boldsymbol{\Psi}(\mathbf{Y})\, d\mathrm{S} \\ &\simeq \sum_{g_{\phi}=1}^{N_{g_{\phi}}} \frac{2\pi}{N_{g_{\phi}}} \sum_{\ell_{2\mathrm{D}}} \sum_{g_{\mathrm{S}}=1}^{N_{g_{\mathrm{S}}}} \omega_{g_{\mathrm{S}}} \mathrm{R}_{\ell_{2\mathrm{D}}}(\mathrm{S}_{g_{\mathrm{S}}})\, \mathcal{J}_{\ell_{2\mathrm{D}}}(\mathrm{S}_{g_{\mathrm{S}}})\, \boldsymbol{\Psi}(\mathbf{Y}(\mathrm{S}_{g_{\mathrm{S}}})).\end{aligned} \tag{3.26}$$

Most of the integrals to be computed are linear functions of the outward normal $\boldsymbol{n}$. In the case of a local boundary parametrized by S, the associated poloidal coordinate is given by

$$\boldsymbol{\xi}(\mathrm{S}) = \mathrm{R}_{\ell_{2\mathrm{D}}}(\mathrm{S})\,\widehat{\mathbf{R}} + \mathrm{Z}_{\ell_{2\mathrm{D}}}(\mathrm{S})\,\widehat{\mathbf{Z}}. \tag{3.27}$$

Then the tangent vector $\partial_{\mathrm{S}}\boldsymbol{\xi}$ and the unit normal $\boldsymbol{n}$ are orthogonal. Thus,

$$\boldsymbol{n} = \boldsymbol{n}_{\mathrm{R}}\widehat{\mathbf{R}} + \boldsymbol{n}_{\mathrm{Z}}\widehat{\mathbf{Z}} = \pm\frac{\partial_{\mathrm{S}}\mathrm{Z}_{\ell_{2\mathrm{D}}}\widehat{\mathbf{R}} - \partial_{\mathrm{S}}\mathrm{R}_{\ell_{2\mathrm{D}}}\widehat{\mathbf{Z}}}{\mathcal{J}_{\ell}} = \frac{1}{\mathcal{J}_{\ell}}\widetilde{\boldsymbol{n}}.$$

The sign of this normal is fixed by the orientation of the reference axis used for the boundary mapping. For instance, the sign is positive when the boundary, mapped with the reference coordinate S, corresponds to $\mathrm{T}^{\star} = 0$; it is negative for $\mathrm{T}^{\star} = 1$. Therefore, any surface integral that is linear to the outward normal can be reformulated as

$$\begin{aligned}\int_{\partial\boldsymbol{\Omega}_{x,h}} (\underline{\mathbf{L}}(\underline{\mathbf{Y}})\,\boldsymbol{n}) &= \int_0^{2\pi} d\phi \sum_{\ell_{2\mathrm{D}}} \int_0^1 \mathrm{R}_{\ell_{2\mathrm{D}}}(\mathrm{S})\, \mathcal{J}_{\ell_{2\mathrm{D}}}(\mathrm{S})\, (\underline{\mathbf{L}}(\underline{\mathbf{Y}})\,\boldsymbol{n})\, d\mathrm{S} \\ &= \sum_{g_{\phi}=1}^{N_{g_{\phi}}} \frac{2\pi}{N_{g_{\phi}}} \sum_{\ell_{2\mathrm{D}}} \sum_{g_{\mathrm{S}}=1}^{N_{g_{\mathrm{S}}}} \omega_{g_{\mathrm{S}}} \mathrm{R}(\mathrm{S}_{g_{\mathrm{S}}})\, (\underline{\mathbf{L}}(\underline{\mathbf{Y}}(\mathrm{S}_{g_{\mathrm{S}}}))\,\widetilde{\boldsymbol{n}}(\mathrm{S}_{g_{\mathrm{S}}})).\end{aligned} \tag{3.28}$$

Similar formulas hold when the parametrization is defined with the reference coordinate T.

4 VMS-Stabilization for Reduced MHD

In the context of tokamak plasmas, some plasma flow regimes can be accurately approximated by reduced equations. Ordering of the scaling parameters is used to define such a regime [31]. In

these regimes, we can assume the following profiles for the magnetic field and the velocity field:

$$\left\{\begin{array}{lcl} \mathbf{B} & = & F\nabla\phi + \nabla\psi\times\nabla\phi, \\ \boldsymbol{v} & = & \vartheta\mathbf{B} + \mathrm{R}^2\nabla\phi\times\nabla\mathrm{U}, \end{array}\right.$$

where $\frac{F}{\mathrm{R}}$ and $\frac{\psi}{\mathrm{R}}$ are toroidal components of the magnetic field and the flux, respectively. The function $F(\boldsymbol{\xi})$ is an input of the model consistent with the initial Grad-Shafranov equilibrium, so that the magnetic field is always divergence-free. $\mathrm{U}(t,\boldsymbol{\xi},\phi)$ is the electric potential and $\vartheta|\mathbf{B}|$ the parallel velocity. These projections also have the effect of separating the compressible and the incompressible waves and reduce the spectral pollution. The consequence is the elimination of fast waves in the direction perpendicular to the magnetic field [31].

A projection of the induction equation is obtained by applying the operator $\mathbf{B}\cdot(\nabla\times)^{-1}$ and a single scalar equation is obtained. This equation gives the evolution of the magnetic flux $\psi(t,\boldsymbol{\xi},\phi)$. According to the assumed ordering, this projection introduces a gradient of the electrical potential. The resulting scalar equation writes as

$$\partial_t\psi + \boldsymbol{v}_\perp\cdot\nabla\psi = \mathbf{K}_\psi(\boldsymbol{\partial},\cdot), \tag{4.1}$$

where $\boldsymbol{v}_\perp = \mathrm{R}^2\nabla\phi\times\nabla\mathrm{U}$ is the velocity component orthogonal to the magnetic field.

For the momentum equation, two projections are achieved. The first projection uses the operator $\mathbf{B}\cdot(\nabla\times)$ to get out an equation for the vorticity $\omega = \nabla\cdot(\boldsymbol{\nabla}_\perp\mathrm{U})$. As $\nabla\times\nabla\equiv 0$, this projection will cancel the gradient of the total pressure $\mathrm{P} = p + \frac{\mathbf{B}\cdot\mathbf{B}}{2}$. The second projection is parallel to the magnetic field $\mathbf{B}$. This projection later assumes that the magnetic field is principally toroidal to obtain a simplified evolution of the normalized parallel velocity ϑ. The Lorentz force is in the kernel (null space) of this projection, parallel to the magnetic field. The equations obtained are

$$\partial_t\omega + \boldsymbol{v}_\perp\cdot\nabla\omega = \mathbf{K}_\omega(\boldsymbol{\partial},\cdot), \tag{4.2}$$

$$\partial_t\vartheta + \boldsymbol{v}\cdot\nabla\vartheta + \frac{\mathbf{B}\cdot\nabla p}{\rho\mathbf{B}\cdot\mathbf{B}} = \mathbf{K}_\vartheta(\boldsymbol{\partial},\cdot). \tag{4.3}$$

The equation of energy is written in the pressure formulation and, as the density equation, written according to the assumed velocity profile:

$$\partial_t\rho + \boldsymbol{v}\cdot\nabla\rho + \rho\mathbf{B}\cdot\nabla\vartheta = \mathbf{K}_\rho(\boldsymbol{\partial},\cdot), \tag{4.4}$$

$$\partial_t p + \boldsymbol{v}\cdot\nabla p + \gamma p\mathbf{B}\cdot\nabla\vartheta = \mathbf{K}_p(\boldsymbol{\partial},\cdot). \tag{4.5}$$

We have introduced a vector operator $\mathbf{K}(\boldsymbol{\partial},\cdot)$ whose components are $\mathbf{K}_\psi(\boldsymbol{\partial},\cdot)$, $\mathbf{K}_\omega(\boldsymbol{\partial},\cdot)$, $\mathbf{K}_\vartheta(\boldsymbol{\partial},\cdot)$, $\mathbf{K}_\rho(\boldsymbol{\partial},\cdot)$ and $\mathbf{K}_p(\boldsymbol{\partial},\cdot)$. The definition of the operator $\mathbf{K}(\boldsymbol{\partial},\cdot)$ depends on the details of the scaling. It can contain first order derivatives associated to diamagnetic effects but in general derivatives therein are of higher order. The derivation of $\mathbf{K}(\boldsymbol{\partial},\cdot)$ should also be guided by the fact that it is useful to have an energy balance associated to the reduced model [31, 14]. The reduced model, in compact form, can be written in a quasi-linear form

$$\frac{\partial\mathbf{W}}{\partial t} + \widetilde{\underline{\mathbf{L}}}(\mathbf{W},\boldsymbol{\partial})\,\mathbf{W} = \mathbf{K}(\boldsymbol{\partial},\cdot), \tag{4.6}$$

where $\mathbf{W}$ are the reduced variables

$$\mathbf{W} = \begin{pmatrix} \rho \\ p \\ \vartheta \\ \omega \\ \psi \end{pmatrix}, \quad \widetilde{\underline{\mathbf{L}}}(\mathbf{W},\boldsymbol{\partial}) = \begin{pmatrix} \boldsymbol{v}\cdot\boldsymbol{\partial} & 0 & \rho\mathbf{B}\cdot\boldsymbol{\partial} & 0 & 0 \\ 0 & \boldsymbol{v}\cdot\boldsymbol{\partial} & \gamma p\mathbf{B}\cdot\boldsymbol{\partial} & 0 & 0 \\ 0 & \frac{\mathbf{B}\cdot\boldsymbol{\partial}}{\rho\|\mathbf{B}\|^2} & \boldsymbol{v}\cdot\boldsymbol{\partial} & 0 & 0 \\ 0 & 0 & 0 & \boldsymbol{v}_\perp\cdot\boldsymbol{\partial} & 0 \\ 0 & 0 & 0 & 0 & \boldsymbol{v}_\perp\cdot\boldsymbol{\partial} \end{pmatrix}.$$

Without loss of generality, we assume for the stabilization process that the system is essentially driven by the left-hand side and the contribution of $\mathbf{K}(\boldsymbol{\partial},\cdot)$ is lower order scale.

For any direction $\boldsymbol{n}$, the matrix $\widetilde{\underline{\mathbf{L}}}(\mathbf{W},\boldsymbol{n})$ is diagonalizable and the eigenvalues are

$$\boldsymbol{v}\cdot\boldsymbol{n},\quad \boldsymbol{v}_\perp\cdot\boldsymbol{n},\quad \boldsymbol{v}\cdot\boldsymbol{n}-\frac{|\mathbf{B}\cdot\boldsymbol{n}|}{\|\mathbf{B}\|}c\quad\text{and}\quad \boldsymbol{v}\cdot\boldsymbol{n}+\frac{|\mathbf{B}\cdot\boldsymbol{n}|}{\|\mathbf{B}\|}c,$$

where $c^2=\frac{\gamma p}{\rho}$ is the acoustic sound speed which is purely hydrodynamic, without any magnetic field contribution. Moreover, acoustic waves do not propagate in the direction orthogonal to the magnetic field (transverse direction). The operator $\boldsymbol{v}\cdot\boldsymbol{\partial}$ can be decomposed as normal and transverse derivatives that are weakly coupled. Consequently, we also derive a decomposition of the differential operator $\widetilde{\underline{\mathbf{L}}}(\mathbf{W},\boldsymbol{\partial})$

$$\boldsymbol{v}\cdot\boldsymbol{\partial}=\vartheta\mathbf{B}\cdot\boldsymbol{\partial}+\boldsymbol{v}_\perp\cdot\boldsymbol{\partial}\quad\text{and}\quad \widetilde{\underline{\mathbf{L}}}(\mathbf{W},\boldsymbol{\partial})=\widetilde{\underline{\mathbf{L}}}_{\mathbf{B}}(\mathbf{W},\boldsymbol{\partial})+\mathbb{I}\boldsymbol{v}_\perp\cdot\boldsymbol{\partial}. \tag{4.7}$$

Therefore, the associated VMS-stabilized weak form writes as

$$\begin{aligned}\int_{\boldsymbol{\Omega}_{x,h}}\frac{\partial\mathbf{W}}{\partial t}\cdot\mathbf{W}^\star+\int_{\boldsymbol{\Omega}_{x,h}}\left(\widetilde{\underline{\mathbf{L}}}(\mathbf{W},\boldsymbol{\partial})\mathbf{W}\right)\cdot\mathbf{W}^\star+\int_{\boldsymbol{\Omega}_{x,h}}\mathbf{K}(\boldsymbol{\partial},\mathbf{W})\cdot\mathbf{W}^\star+\frac{1}{\varepsilon}\int_{\partial\boldsymbol{\Omega}_{x,h}}\mathbf{S}(\mathbf{W},\mathbf{W}_b,\mathbf{W}^\star)\\ =-\int_{\boldsymbol{\Omega}_{x,h}}\left(\widetilde{\underline{\mathbf{L}}}_{\mathbf{B}}(\mathbf{W},\boldsymbol{\partial})\delta\mathbf{W}\right)\cdot\underline{\boldsymbol{\mathcal{T}}}_{\mathbf{B}}\left(\widetilde{\underline{\mathbf{L}}}_{\mathbf{B}}^{\mathrm{T}}(\mathbf{W},\boldsymbol{\partial})\mathbf{W}^\star\right)-\int_{\boldsymbol{\Omega}_{x,h}}\left(\boldsymbol{v}_\perp\cdot\boldsymbol{\partial}\delta\mathbf{W}\right)\cdot\left(\underline{\boldsymbol{\mathcal{T}}}_\star\boldsymbol{v}_\perp\cdot\boldsymbol{\partial}\mathbf{W}^\star\right),\end{aligned} \tag{4.8}$$

where $\mathbf{S}(\mathbf{W},\mathbf{W}_b,\mathbf{W}^\star)$ is the contribution associated to the penalty of Dirichlet boundary conditions. The computation of $\underline{\boldsymbol{\mathcal{T}}}_{\mathbf{B}}$ and $\underline{\boldsymbol{\mathcal{T}}}_\star$ will use similar strategies as for the full MHD model adapted to the wave structure of the Reduced MHD.

5 Numerical Validations

Grad-Shafranov equilibrium. In order to compute MHD instabilities in tokamak geometries, we very often start with an initial condition that is a solution of the static MHD equilibrium without flow $\boldsymbol{v}=0$. At this equilibrium, we can use a reduced axisymmetric magnetic field such that the ideal MHD equations reduce to

$$\nabla p=\mathbf{J}\times\mathbf{B}\quad\text{with}\quad \mathbf{J}=\nabla\times\mathbf{B}\quad\text{and}\quad \mathbf{B}=F\nabla\phi+\nabla\psi\times\nabla\phi. \tag{5.1}$$

The poloidal current flux is a function of the poloidal coordinates - $F(\boldsymbol{\xi})$ - such that the reduced magnetic field, in the previous equation, is always divergence free $\nabla\cdot\mathbf{B}=0$. Indeed, by construction of the cylindrical coordinates, we have $\nabla\cdot\nabla\phi=0$ and it is easy to see that the poloidal component $(\nabla\psi\times\nabla\phi)$ of the magnetic field is also divergence free. The projection of the equilibrium forces in the magnetic direction gives $\mathbf{B}\cdot\nabla p=0$ and, for axisymmetric solutions, we have $\nabla\phi\cdot\nabla p=0$, so that $(\nabla\psi\times\nabla\phi)\cdot\nabla p=0$. We finally obtain that the pressure is a function of the magnetic flux. Similarly, with the projection in the current field direction it can be found that the total poloidal current flux is also a function of the magnetic flux. Then, using these results, the projection onto the toroidal direction gives an elliptic equation, very often nonlinear, made famous by Grad[21] and Shafranov[35]

$$-\Delta^\star\psi=F(\psi)\frac{dF}{d\psi}(\psi)+\mathrm{R}^2\frac{dp}{d\psi}(\psi), \tag{5.2}$$

where $\Delta^\star\psi=\mathrm{R}^2\nabla\cdot\left(\frac{1}{\mathrm{R}^2}\nabla\psi\right)$. The given functions $F(\psi)$ and $p(\psi)$ are, at this point, completely arbitrary and should be defined from additional considerations associated to the device under

concern. When $F(\psi)$ and $p(\psi)$ are nonlinear, there is no theoretical guarantee of the existence and/or uniqueness of the previous equation, even when equipped with Dirichlet boundary conditions. When the parametrization functions are designed by a fitting over experimental data, our hope is that, at least, there exists a solution of (**??**). The fitting assumes polynomial profile for the density, the temperature and for $\widetilde{G}(\psi) = (F(\psi))^2$ the square of the poloidal current flux:

$$\left\{\begin{array}{rcl} \widetilde{\rho}(\psi,\psi_\star,\psi_\times) & \simeq & \widetilde{\rho}^{(0)}\left(1+\sum_{\mathrm{s}=1}^{\mathrm{s}_p}\widetilde{\rho}^{(\mathrm{s})}\left(\overline{\psi}\right)^{\mathrm{s}}\right), \\ \widetilde{T}(\psi,\psi_\star,\psi_\times) & \simeq & \widetilde{T}^{(0)}\left(1+\sum_{\mathrm{s}=1}^{\mathrm{s}_p}\widetilde{T}^{(\mathrm{s})}\left(\overline{\psi}\right)^{\mathrm{s}}\right), \\ \widetilde{G}(\psi,\psi_\star,\psi_\times) & \simeq & \widetilde{G}^{(0)}+2(\psi_\times-\psi_\star)\sum_{\mathrm{s}=1}^{\mathrm{s}_f}\widetilde{G}^{(\mathrm{s})}\dfrac{\left(\overline{\psi}\right)^{\mathrm{s}}}{\mathrm{s}}, \end{array}\right. \tag{5.3}$$

where $p^{(\mathrm{s})}$, $\widetilde{T}^{(\mathrm{s})}$ and $\widetilde{G}^{(\mathrm{s})}$ are fitting parameters. The profile of $\widetilde{G}$ is defined in order to have a simpler formula for the function that is usually fitted: $F\dfrac{dF}{d\psi}$. The normalized flux $\overline{\psi}$ is defined as

$$\overline{\psi} \equiv \overline{\psi}(\psi) = \frac{\psi-\psi_\star}{\psi_\times-\psi_\star}, \tag{5.4}$$

$\psi_\star$ and $\psi_\times$ are either given constants or nonlinear functions defining the flux values at the magnetic axis $\psi_\star \equiv \psi_\star(\psi)$ and at a specific flux surface $\psi_\times \equiv \psi_\times(\psi)$. This specific flux surface can be a separatix (divertor configuration), the last surface or the first open surface (limiter configuration). From the profile of $\widetilde{G}(\psi)$ and the equation of state $p = \rho T$, we can obtain the following estimations

$$\left\{\begin{array}{rcl} \dfrac{dp}{d\psi}(\psi) & \simeq & \widetilde{T}\dfrac{d\widetilde{\rho}}{d\psi}+\widetilde{\rho}\dfrac{d\widetilde{T}}{d\psi} \simeq \dfrac{1}{\psi_\times-\psi_\star}\left(\widetilde{T}\dfrac{\partial\widetilde{\rho}}{\partial\overline{\psi}}+\widetilde{\rho}\dfrac{\partial\widetilde{T}}{\partial\overline{\psi}}\right), \\ F(\psi)\dfrac{dF}{d\psi}(\psi) & \simeq & \dfrac{1}{2}\dfrac{\partial\widetilde{G}}{\partial\psi} \simeq \dfrac{1}{2(\psi_\times-\psi_\star)}\dfrac{\partial\widetilde{G}}{\partial\overline{\psi}} = \sum_{\mathrm{s}=1}^{\mathrm{s}_f}\widetilde{G}^{(\mathrm{s})}\left(\overline{\psi}\right)^{\mathrm{s}-1}, \end{array}\right. \tag{5.5}$$

where the partial derivative $\frac{\partial}{\partial\overline{\psi}}$ is for fixed $\psi_\star$ and $\psi_\times$.

The Galerkin finite element method is used to approximate the Grad-Shafranov equation. The nonlinear system is solved by Picard iterations, by inverting the following linear system for ψ^{k+1}:

$$\int_{\mathbf{\Omega}_{2\mathrm{D}}}\frac{1}{\mathrm{R}}\nabla\psi^{(k+1)}\cdot\nabla\psi^\star d\mathrm{R}d\mathrm{Z} = \int_{\mathbf{\Omega}_{2\mathrm{D}}}\frac{1}{\mathrm{R}}\left(F\left(\psi^{(k)}\right)\frac{dF}{d\psi}\left(\psi^k\right)+\mathrm{R}^2\frac{dp}{d\psi}\left(\psi^{(k)}\right)\right)\psi^\star d\mathrm{R}d\mathrm{Z}, \tag{5.6}$$

with homogeneous Dirichlet boundary conditions. Eventually, $\psi_\star^{(k+1)} \equiv \psi_\star\left(\psi^{(k+1)}\right)$ and $\psi_\times^{(k+1)} \equiv \psi_\times\left(\psi^{(k+1)}\right)$ are computed at each step. When the Picard iterations converge, always the case in our applications, an approximated solution ψ^{eq} of the nonlinear system (5.2) is obtained. In order to simplify the relation with the reduced MHD, it is useful to define the magnetic field with a modified magnetic potential, abusively denoted by $\mathbf{A}$:

$$\mathbf{B} = F^{\mathrm{eq}}\nabla\phi + \nabla\times\mathbf{A} \quad \text{where} \quad F^{\mathrm{eq}} = \sqrt{\widetilde{G}\left(\psi^{\mathrm{eq}},\psi_\star^{\mathrm{eq}},\psi_\times^{\mathrm{eq}}\right)}. \tag{5.7}$$

As F^{eq} and $\nabla\phi$ are fixed in time, the equation for the new potential is the same as previously. Therefore, the unperturbed initial data are:

$$\rho^{\mathrm{eq}} = \widetilde{\rho}\left(\psi^{\mathrm{eq}},\psi_\star^{\mathrm{eq}},\psi_\times^{\mathrm{eq}}\right), \quad \boldsymbol{v}^{\mathrm{eq}} = 0, \quad p^{\mathrm{eq}} = \rho^{\mathrm{eq}}T^{\mathrm{eq}} \quad \text{and} \quad \mathbf{A}^{\mathrm{eq}} = \psi^{\mathrm{eq}}\nabla\phi, \tag{5.8}$$

where $T^{\mathrm{eq}} = \widetilde{T}\left(\psi^{\mathrm{eq}}, \psi_{\star}^{\mathrm{eq}}, \psi_{\times}^{\mathrm{eq}}\right)$.

Internal disruption : kink mode. The kink instability occurs in a current carrying plasma when the current exceeds a critical value and it is due to the non-uniformity of the current. Even though this is mainly a current driven instability, the pressure also plays a role. It was shown that if the pressure is sufficiently low the plasma is stable and if it exceeds a threshold value it becomes unstable (see [9]). This instability can be compared to the twisting of a rubber string, if the twisting exceeds a threshold, the rubber string develops helical deformation. In a Tokamak, the twisting of the magnetic field is provided by the poloidal magnetic field produced by the current and similar plasma deformations occur. The internal kink instability is localized at the magnetic mode rational surfaces (i.e, magnetic flux surfaces that are closed). This characteristic is given by the safety factor q which determines the number of toroidal turns (m) of a field line for each poloidal turn (n). The internal disruption (also called sawtooth instability) has a poloidal mode number $m = 1$ and a toroidal mode number $n = 1$ and therefore resonant with the magnetic flux topology at q = 1.

We consider a low-β plasma (where the magnetic pressure is larger than the hydrodynamic pressure) at a toroidal symetric equilibrium. The Grad-Shafravov equilibrium is obtained with the following inputs

$\psi_{\star} = -0.4792, \qquad \psi_{\times} = 0$			
$\mathrm{s}_p = 1$	$\widetilde{\rho}^{(0)} = 1$	$\widetilde{\rho}^{(1)} = -\frac{9}{10}$	
$\mathrm{s}_p = 1$	$\widetilde{T}^{(0)} = \frac{\beta_{\star}}{2} = 2\,10^{-3}$	$\widetilde{T}^{(1)} = -\frac{8}{10}$	
$\mathrm{s}_f = 2$	$\widetilde{G}^{(0)} = 100$	$\widetilde{G}^{(1)} = -2$	$\widetilde{G}^{(2)} = 2$

This equilibrium is computed by a cubic bezier isoparametric finite element on a polar quadrangular mesh with a geometrical singularity at the center (figure 1). The equilibrium profiles of density and magnetic flux are plotted in the Figure 2. The resonant surface (q = 1) is associated to the magnetic flux surface $\psi = -0.229$. Starting from the numerical equilibrium (figure 2) a perturbation of the toroidal velocity is introduced (figure 3). Therefore, the initial data, for the simulation of the kink mode, is given by

$$\rho\left(t=0, \boldsymbol{\xi}, \phi\right) = \rho^{\mathrm{eq}}\left(\boldsymbol{\xi}\right), \qquad p^{\mathrm{eq}}\left(t=0, \boldsymbol{\xi}, \phi\right) = p^{\mathrm{eq}}\left(\boldsymbol{\xi}\right), \qquad \mathbf{A}\left(t=0, \boldsymbol{\xi}, \phi\right) = \mathbf{A}^{\mathrm{eq}}\left(\boldsymbol{\xi}\right)$$

and

$$\boldsymbol{v}^{\mathrm{eq}} = 10^{-12} \sin\left(\phi\right) \widehat{\boldsymbol{\phi}}, \tag{5.9}$$

with $\mathbf{B}\left(t, \boldsymbol{\xi}, \phi\right) = F^{\mathrm{eq}}\left(\boldsymbol{\xi}\right) \nabla\phi + \nabla \times \mathbf{A}\left(t, \boldsymbol{\xi}, \phi\right)$

The simulation was then ran taking into account three toroidal Fourier Harmonics. It can be seen in Figure 4 that during the linear growth of the instability the velocity profile develops a thin layer structure around the resonant surface q = 1 ($\psi \approx -0.229$) which is characteristic of the internal kink instability. This structure is very fine and its width is related to the Reynolds Magnetic number S. For smaller S the width is larger, becoming finer and finer as S grows (refer to Figure 5). For $S = 10^5$ (left) it is around 1.10^{-1} wide, while for $S = 10^8$ (right) it is approximately 3.10^{-2}.

To test the effects of the numerical stabilization, two test-cases were taken into consideration. In the first one, only a uniform numerical viscosity of 10^{-5} was applied in the whole domain to play the stabilizing role, while for the second one the VMS-Stabilization was implemented. It can be clearly seen in Figure 6 that only the presence of a numerical viscosity (right) is not enough to stabilize the scheme. The velocity profile obtained (top right) for the Fourier mode $\cos(\phi)$ is very noisy and contains several oscillations compared to the one obtained with the VMS

formulation (top left). For the density profile the scenario is even worse. Without the numerical stabilization it is almost impossible to see the formation of the expected profile and the result is mainlt composed of noise (bottom-right). With the VMS, on the other hand, the profile is clear (bottom-left) containing only some oscillations on the border of the profile. This is due to the fact that the stabilization operator used for this test case is a simplified version of the most general operator $\underline{\mathbf{L}}$.

From now on, only test cases with the VMS-Stabilization are taken into account. The objective of the study was to analyze the dynamics of the internal kink mode considering two different configurations: a semi-linear one in which the Fourier mode cos(0) is assumed to be constant and is then forced to be equal to its equilibrium value during the entire simulation, and a nonlinear one, in which all modes are set to run and evolve freely. Figure 7 shows the evolution of the z-component of the velocity (top) and the ϕ component of the potential vector (bottom) for the first two Fourier modes - cos(0) and cos(ϕ). For the semi-linear modeling all the components of the velocity in the mode cos(0) are set to be zero and that is the reason why it is not shown in the semi-log plot (up left). It can be seen however that assuming a constant value for this mode is not a bad approximation because it stays almost constant during the evolution for the non-linear case. This is even more apparent for ψ (bottom-left) for which the value stays really constant even if it is set to run freely. The figures on the right show that the dynamics of the other modes can be divided into three parts: an oscillatory one in which the profiles shown before (Figures 4,5 and 6) are still forming; and, a linear phase in which the growth rate stays constant, followed by a second oscillatory phase. Nonetheless, only the beginning of this last one is seen before the divergence of the simulation. This is probably related to the large time-step used, although it is reasonable for the linear growth phase it is too large for a non-linear regime. Also, it can be related to the simplified form of the stabilization. During this phase the convective phenomena arising in the simulation start to become important and then an extended version of the current stabilization must be implemented.

All the results shown were obtained for a Reynolds Magnetic number $S = 10^8$. However, as the kink instability is driven mainly by a current, the resistivity and hence the Reynolds Magnetic number ($S \equiv VL/\eta$, in which V is the typical velocity of the flow, L is the typical length scale and η is the resistivity) must play an important role. As it was said before, the width of the kink structure formed around the resonant surface will become finer as S grows. Nevertheless, it is not the only resistive effect observed. The growth rate of the instability will also change (see Figure 8). The resistive kink behavior is expected to have a growth rate $\gamma \propto S^{-\frac{1}{3}}$ and it was obtained for both - semi and non-linear - configurations for most of the values of S considered. The non-linear simulations however became very unstable for small ($S < 10^3$) and very high ($S > 10^9$) values of the magnetic number. Also, (figure 8) shows the transition from the resistive kink behavior to a more slowly growing tearing $\gamma \propto S^{-\frac{3}{5}}$ behavior at high values of S.

Equilibrium for X-point geometry The main goal of the test cases with divertor geometry is the simulation of the Edge localized modes (ELMs) instability. For this, one must first obtain a steady or at least a quasi-steady kinetic equilibrium and then, after, launch the Fourier harmonic perturbations. To obtain the quasi-steady state one should run a simulation with only the $n = 0$ Fourier harmonic. The goal of this first test case is only to study this quasi-static equilibrium.

For this, we have run a simulation with the following parameters

$$\begin{aligned} \rho &= 1 - 0.2375\psi_n, \\ T &= 1.2 \times 10^{-1} - 7.9867 \times 10^{-2}\psi_n, \\ FF' &= 4.8(1 - \psi_n), \end{aligned}$$

The Magnetic Reynolds number used is $S = 10^7$ and the timestep was fixed to $\delta t = 1$.

Figure 6 shows the 3D configuration and a poloidal cut of the magnetic field lines the density and velocity profiles after one timestep. In Figure 18 the red line represents the separatrix, i.e. the last closed flux surface of the configuration. The velocity is expressed in terms of the Mach number (ratio between the velocity and the sound speed in the medium). It is better to use this representation because for the divertor configuration, Bohm boundary conditions must be implemented since there may be contact between the plasma and a material wall. These conditions are related to the fact that when a material wall gets in contact with the plasma, which is the case for the divertor plates, a sheath region appears near the wall. The particles entering these regions must a have a velocity superior to the sound speed.

The sound speed is imposed on the divertor plates and need some time (in a sonic time-scale) to diffuse into the plasma. However, we can note from Figure 18, that it has considerably diffused after ten timesteps. Figure 19 shows in more detail the velocity profile as well the direction of the velocity field.

The simulation was let to run up to $t \approx 220$ and the resulting profiles are shown in Figure 20. It can be clearly seen that the density and the velocity have diffused. In fact, there is a density flow that is created following the separatrix up to the divertors in which it is evacuated. This loss is compensated by particles sources added to the continuity equation. As before, more details of the velocity field around the divertors can be seen in Figure 21. It is a reasonable velocity field considering that it is perfectly aligned with the magnetic field and the diffusion of the Mach condition can be clearly seen.

For this test case, a quasi-steady state has not been fully achieved, however it can be seen in Figure 22 that the kinetic energy growth rate has decreased as the time passed, which means that we are not far from reaching a steady state in which it might be constant.

6 Conclusions and perspectives

We have developed a stabilized finite element strategy for numerical approximation of compressible MHD equations. The divergence free of the magnetic field is achieved under a potential vector formulation. The finite element is designed to ensure global C^1 smoothness of interpolation functions. Moreover, boundary conditions were implemented as penalty line integrals over the edge of the domain.

Some numerical studies were performed in order to validate the model, starting with the plasma equilibrium. It was done taking into account the Grad-Shafranov equation without flow ($\boldsymbol{v} = 0$), to which the pressure and magnetic field profiles were given as input parameters. These profiles were chosen to correspond to an experimental profile typically obtained in tokamaks. This equilibrium was successfully calculated and it gives the initial plasma configuration that will be perturbed for the study of the MHD instabilities.

The internal kink instability was reproduced by adding a perturbation to the velocity after having the established equilibrium. As expected, the formation of a thin layer around the resonant surface for the toroidal mode ($m = 1$) was observed. A dependence of this mode width on the magnetic Reynolds number S was also verified. Since kink modes are current driven instabilities and having in mind that S is related to the resistivity, this result comes as expected. It is important to remark that, without the VMS stabilization implemented, these results could not be obtained. In fact, the fast acoustic waves, whose are intrinsic to the full MHD model, have a destabilizing effect. Moreover, as the flows here are dominated by convection, the unresolved scales can grow to affect the resolved ones. During the kink simulations it was shown that if the stabilization is not taken into account, the numerical noise will overcome the physical phenomena and the results obtained are composed mostly of noise.

Another important characteristic that helps in the identification of the internal kink instability is its growth rate which is related to S. It has been verified here that the stabilization does not affect it, restraining its effects to the numerical level and not killing physical perturbations. The dependence on the magnetic Reynolds number obtained agrees with results obtained with the linear MHD code PHOENIX [20, 6] and also with results obtained by Hastiel et al. [23]. For $S < 10^4$ the mode width becomes comparable to the machine size and the scaling is lost entirely. For higher S, a transition is observed and the growth rate shifts from $S^{-\frac{1}{3}}$ to $S^{-\frac{3}{5}}$ which has been also observed by [23] and analytically described by Coppi et al [12] and extended by Bussac et al [9]. In fact, the second growth rate obtained is a characteristic of another MHD disruption known as tearing modes. Finally, the reconnection of the magnetic flux surfaces has been also observed, validating one more characteristic of the internal kink disruption.

After successfully validating the model for a plasma in the circular configuration, the study was extended for x-point plasmas. The model used was exactly the same and the main differences were the geometry of the problem and the boundary conditions. For circular cases, it is assumed that there is no contact between the plasma and the walls of the device. This assumption cannot be extended to x-point plasmas because the open magnetic field lines will transport particles to the targets located at the basis of the device, called divertors. Thus, at these boundaries the velocity component that is parallel to the magnetic field is set to the local sound speed in the outgoing direction. These conditions generate a great flow near the divertors, such that, before triggering an instability, a second quasi-steady equilibrium in which the parallel and poloidal flows would be well established, must be reached. For this, the axisymmetric equilibrium (obtained with Grad-Shafranov) was let to evolve without any harmonics until the kinetic energy stayed constant. The results obtained with the model are reasonable since the velocity field is well aligned with the magnetic field lines and the kinetic energy has a growth rate that is lowering, indicating that a quasi-steady state is near.

The stabilized full MHD model implemented and validated here opens up a scenario for more powerful and detailed simulations for tokamak plasmas, specially in the context of ITER for which a better understanding of the physics inside the device will be needed. The goal now is to use this model to better describe the Edge-localized modes. In recent years a large number of detailed measurements of these modes has become available allowing the validations of numerical simulations.

References

[1] R. Abgrall. Essentially non-oscillatory Residual Distribution schemes for hyperbolic problems . *Journal of Computational Physics*, 214:773–808, 2006.

[2] A. B. H. Ali and A. Soulaimani. An unstructured finite elements method for solving the compressible RANS equations and the Spalart-Allmaras turbulence model. *Computer Methods in Applied Mechanics and Engineering*, 199:2261–2272, July 2010.

[3] D. Ambrosi and L. Quartapelle. A taylor-galerkin method for simulating nonlinear dispersive water waves. *Journal of Computational Physics*, 146(2):546 – 569, 1998.

[4] T. J. Barth and D. C. Jespersen. The design and application of upwind schemes on unstructured meshes . *AIAA paper 89-0355, 27th AIAA Aerospace Sciences Meeting, Reno, Nevada (USA)*, 1989.

[5] M. Billaud, G. Gallice, and B. Nkonga. A simple stabilized finite element method for solving two phase compressible-incompressible interface flows. *Computer Methods in Applied Mechanics and Engineering*, 200(9-12):1272–1290, 2011.

[6] J. W. S. Blokland, B. van der Holst, R. Keppens, and J. P. Goedbloed. Phoenix: Mhd spectral for rotating laboratory and gravitating astrophysical plasmas. *J. Comp. Phys.*, 226:509–533, 2007.

[7] S. I. Braginskii. Transport processes in a plasma. *Reviews of Plasma Physics*, 1:205, 1965.

[8] A. Brooks and T. Hughes. Streamline upwind/Petrov-Galerkin formulations for convection dominated flows with particular emphasis on the incompressible Navier-Stokes equations . *Computer Methods in Applied Mechanics and Engineering*, 32:199–259, 1982.

[9] M. Bussac, R. Pellat, D. Edery, and J. Soule. Internal kink modes in toroidal plasmas with circular cross sections. *Phys. Rev. Lett.*, 35:1638, 1975.

[10] I. Christie, D. Griffiths, A. R. Mitchell, and O. Zienkiewicz. Finite element methods for second order differential equations with significant first derivatives . *Internat. J. Numer. Methods Engrg.*, 10:1389–1396, 1976.

[11] R. Codina and N. Hernàndez Silva. Stabilized finite element approximation of the stationary magneto-hydrodynamics equations. *Computational Mechanics*, 38:344–355, 2006.

[12] B. Coppi, R. Galvao, R. Pellat, M. N. Rosenbluth, and P. H. Rutherford. -. *Sov. J. Plasma Phys.*, 2(533), 1976.

[13] O. Czarny and G. Huysmans. Bézier surfaces and finite elements for MHD simulations. *Journal of Computational Physics*, 227(16):7423–7445, 2008.

[14] B. Desprès and R. Sart. Reduced resistive mhd in tokamaks with general density. *ESAIM: Mathematical Modelling and Numerical Analysis*, 46:1081–1106, 9 2012.

[15] J. Donea, S. Giuliani, H. Laval, and L. Quartapelle. Time-accurate solution of advection-diffusion problems by finite elements. *Computer Methods in Applied Mechanics and Engineering*, 45(1-3):123 – 145, 1984.

[16] J. Donea, L. Quartapelle, and V. Selmin. An analysis of time discretization in the finite element solution of hyperbolic problems. *Journal of Computational Physics*, 70(2):463 – 499, 1987.

[17] N. Ferraro and S. Jardin. Calculations of two-fluid magnetohydrodynamic axisymmetric steady-states. *Journal of Computational Physics*, 228(20):7742 – 7770, 2009.

[18] T.-P. Fries and H. G. Matthies. A Review of Petrov-Galerkin Stabilization Approaches and an Extension to Meshfree Methods . *Scientific Computing*, 2004.

[19] S. Godunov, A. Zabrodine, M. Ivanov, A. Kraiko, and G. Prokopov. *Résolution numérique des problèmes multidimensionnels de la dynamique des gaz*. Mir, 1979.

[20] J. P. Goedbloed, A. J. C. Belien, B. van der Holst, and R. Keppens. Unstable continuous spectra of transonic axisymmetric plasmas. *Phys. Plasmas*, 11:28–54, 2004.

[21] H. Grad and H. Rubin. Hydromagnetic equilibria and force-free fields. *Journal of Nuclear Energy (1954)*, 7(3-4):284–285, 1958.

[22] D. S. Harned and W. Kerner. Semi-implicit method for three-dimensional compressible magnetohydrodynamic simulation. *Journal of Computational Physics*, 60(1):62 – 75, 1985.

[23] R. J. Hastie, T. C. Hender, B. A. Carreras, L. A. Charlton, and J. A. Holmes. Stability of ideal and resistive internal kink modes in toroidal geometry. *Physics of Fluids*, 30(6):1756–1766, 1987.

[24] P. Hénon, P. Ramet, and J. Roman. Pastix: a high-performance parallel direct solver for sparse symmetric positive definite systems. *Parallel Computing*, 28(2):301 – 321, 2002.

[25] T. Hughes, M. Mallet, and A. Mizukami. A new finite element formulation for computational fluid dynamics : II. Beyond SUPG . *Computer Methods in Applied Mechanics and Engineering*, 54:341–355, 1986.

[26] T. Hughes, G. Scovazzi, and T. Tezduyar. Stabilized Methods for Compressible Flows. *Journal of Scientific Computing*, 43:343–368, 2010.

[27] T. J. R. Hughes, G. Scovazzi, and L. P. Franca. *Multiscale and Stabilized Methods*, chapter . John Wiley & Sons, Ltd, 2004.

[28] G. Huysmans. ELMs: MHD instabilities at the transport barrier. *Plasma Physics and Controlled Fusion*, 47(12B):B165–B178, 2005.

[29] K. Jansen, S. Collis, C. Whiting, and F. Shaki. A better consistency for low-order stabilized finite element methods . *Computer Methods in Applied Mechanics and Engineering*, 174:153–170, 1999.

[30] S. Jardin. Review of implicit methods for the magnetohydrodynamic description of magnetically confined plasmas. *Journal of Computational Physics*, 231(3):822 – 838, 2012.

[31] S. Kruger, C. Hegna, and J. Callen. Generalized reduced magnetohydrodynamic equations. *Physics of Plasmas*, 5, 12 1998.

[32] H. Lutjens and J.-F. Luciani. Xtor-2f: A fully implicit newton-krylov solver applied to nonlinear 3d extended mhd in tokamaks. *Journal of Computational Physics*, 229(21):8130 – 8143, 2010.

[33] A. Mizukami and T. Hughes. A Petrov-Galerkin finite element method for convection-dominated flows: an accurate upwinding technique for satisfying the maximum principle . *Comput. Methods Appl. Mech. Engrg.*, 50:181–193, 1985.

[34] J. Rice and R. Schnipke. A monotone streamline upwind finite element method for convection-dominated flows . *Comput. Methods Appl. Mech. Engrg.*, 48:313–327, 1985.

[35] V. Shafranov. On magnetohydrondynamical equilibrium configurations. *Sov. Phys. JETP-USSR*, 1958.

[36] A. Soulaimani and M. Fortin. Finite element solution of compressible viscous flows using conservative variables . *Computer Methods in Applied Mechanics and Engineering*, 118:319–350, 1994.

[37] C. Sovinec, A. Glasser, T. Gianakon, D. Barnes, R. Nebel, S. Kruger, D. Schnack, S. Plimpton, A. Tarditi, M. Chu, and the NIMROD Team. Nonlinear magnetohydrodynamics simulation using high-order finite elements. *Journal of Computational Physics*, 195(1):355 – 386, 2004.

[38] T. Tezduyar and M. Senga. Stabilization and shock-capturing parameters in SUPG formulation of compressible flows . *Comput Meth Appl Mech Eng*, 195:1621–1632, 2006.

[39] J. P. Trelles and S. M. Modirkhazeni. Variational multiscale method for nonequilibrium plasma flows. *Computer Methods in Applied Mechanics and Engineering*, 282(0):87 – 131, 2014.

[40] J. von Neumann and R. D. Richtmyer. A method for the numerical calculations of hydrodynamical shocks. *J. Appl. Phys.*, 21:232–238, 1950.

[41] C. Wervaecke, H. Beaugendre, and B. Nkonga. A fully coupled rans spalart-allmaras supg-formulation for turbulent compressible flows on stretched-unstructured grids. *Computer Methods in Applied Mechanics and Engineering*, 233-236:109–122, 2012.

[42] C. Whiting, K. Jansen, and S. Dey. Hierarchical basis for stabilized finite element methods for compressible flows. *Computer Methods in Applied Mechanics and Engineering*, 192:5167–5185, 2003.

[43] M. L. Wilkins. Calculation of elastic plastic flow. *Methods in Computationnal Physics*, 3, 1964.

[44] M. L. Wilkins. Use of artificial viscosity in multidimensionnal fluid dynamic calculations. *J. Comput. Phys.*, 36:381–403, 1980.

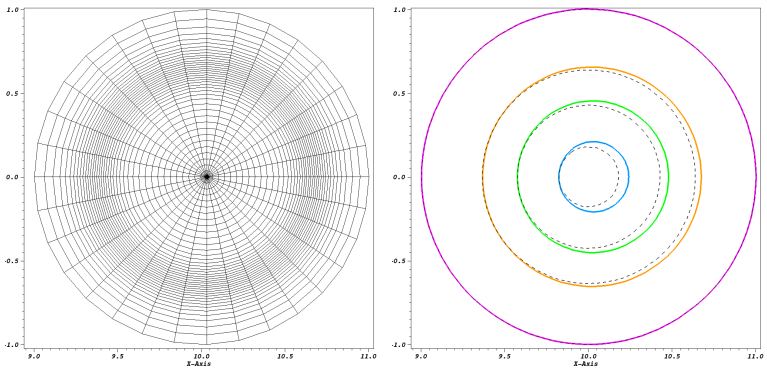

Figure 1: Grad-Shafranov equilibrium : Mesh aligned on magnetic flux surfaces (left) and Shifting of the Magnetic flux surfaces(right). Dotted lines are isolines of the radius to the center of the geometrical domain. Solid lines are iso magnetic fluxes. The second isoline from the boundary is where the safety factor is nearly one. Magnetic flux isolines are for : $\psi = -10^{-3}$, $\psi = -0.229$, $\psi = -0.35$ and $\psi = -0.45$.

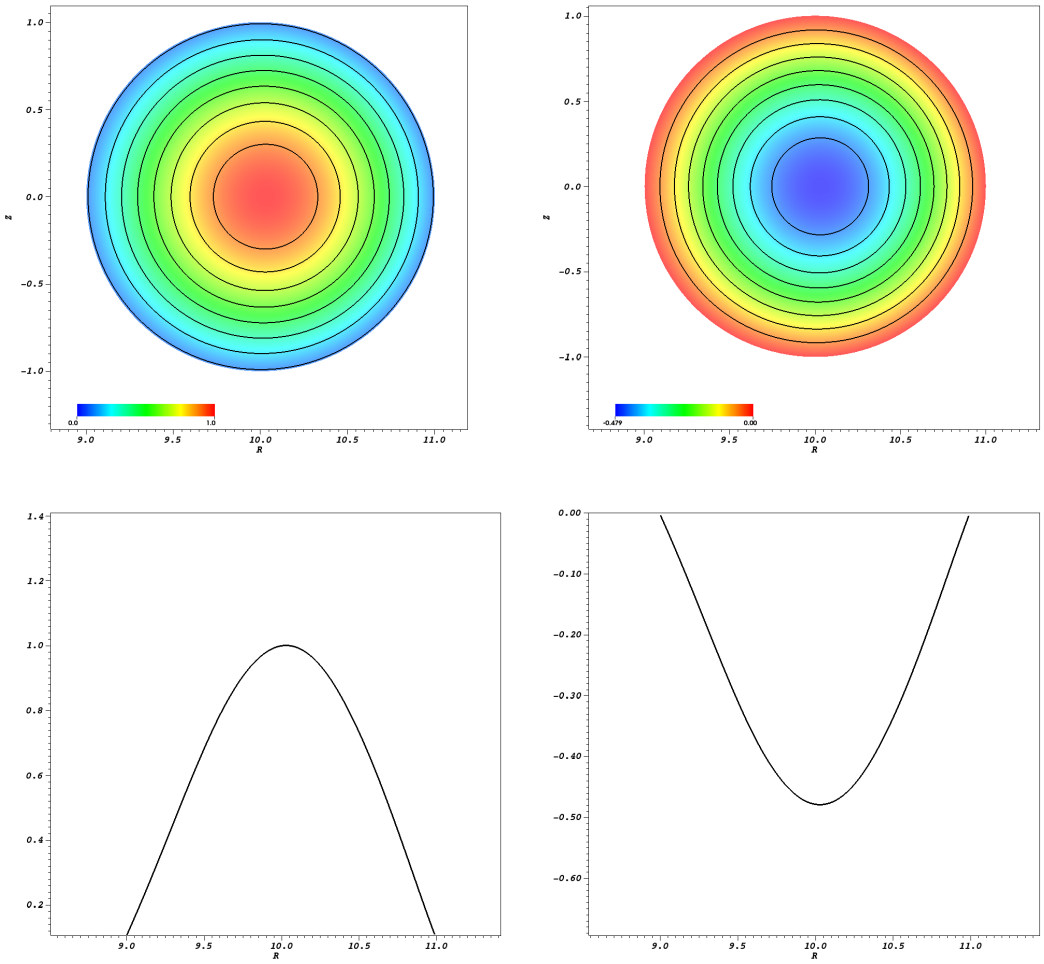

Figure 2: Grad-Shafranov equilibrium. 2D plots and profiles for the density (left) and magnetic flux (right).

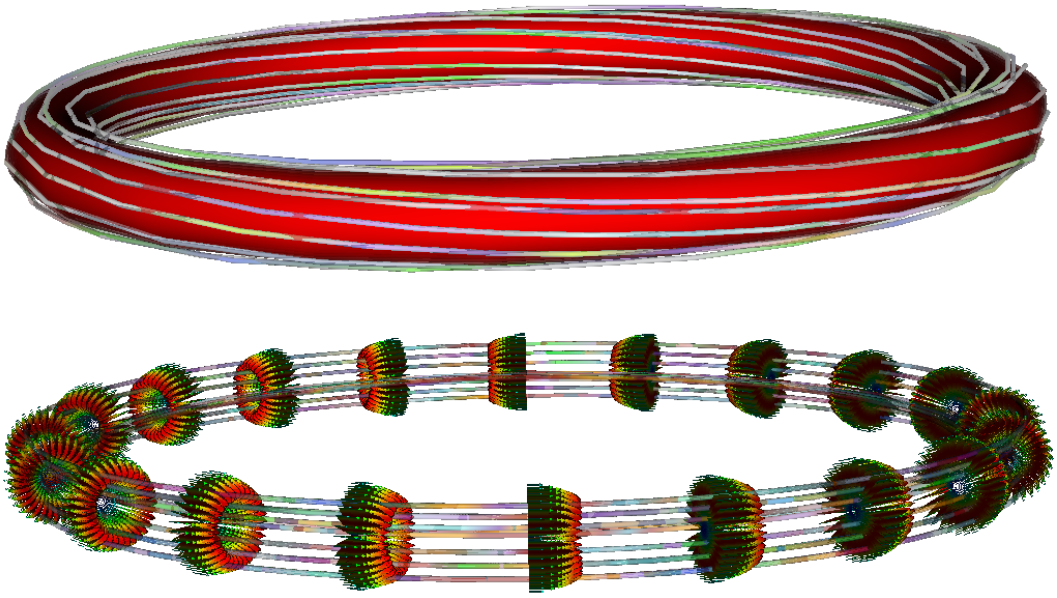

Figure 3: Initial data for the 3D computations, Density and magnetic streamlines (top), initial perturbation of the first mode for velocity (bottom) of order 10^{-12}

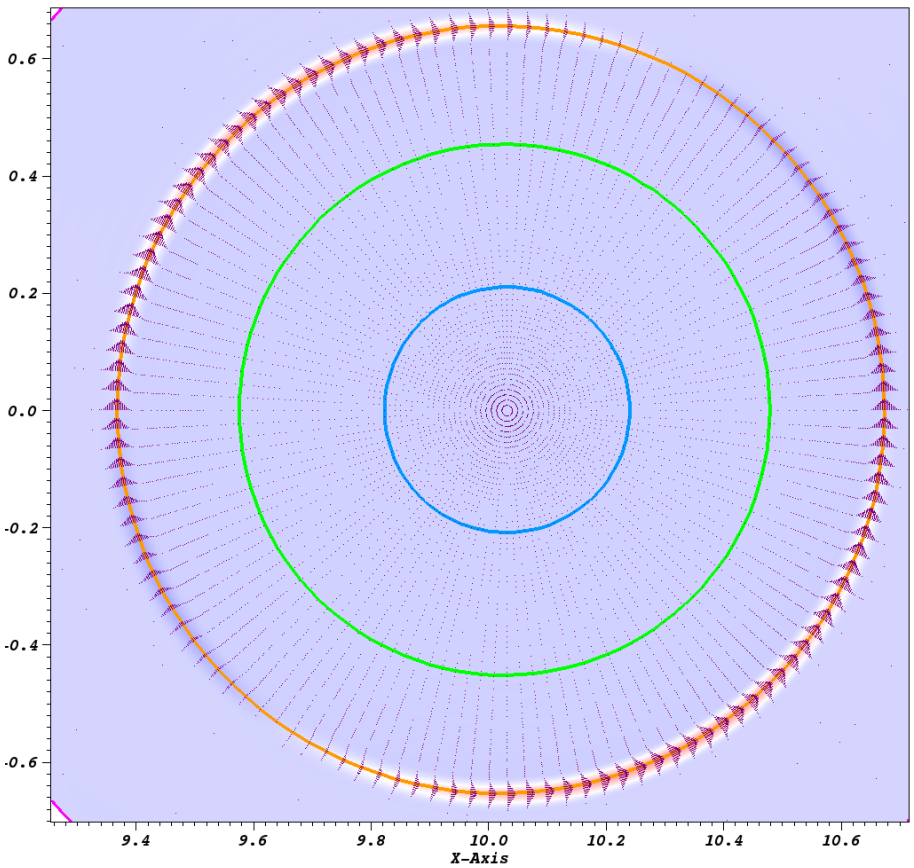

Figure 4: Internal Kink mode : Velocity field and thin layer around the resonant surface ($q = 1$, $\psi \simeq -0.229$), during the linear growth of the instability. The inertial effects are important in a layer close to the resonant surface. This layer width is around $4\,10^{-2}$ that is of order ε^2 where ε is the inverse aspect ratio. Magnetic flux isolines are given for : $\psi = -10^{-3}$, $\psi = -0.229$, $\psi = -0.35$ and $\psi = -0.45$.

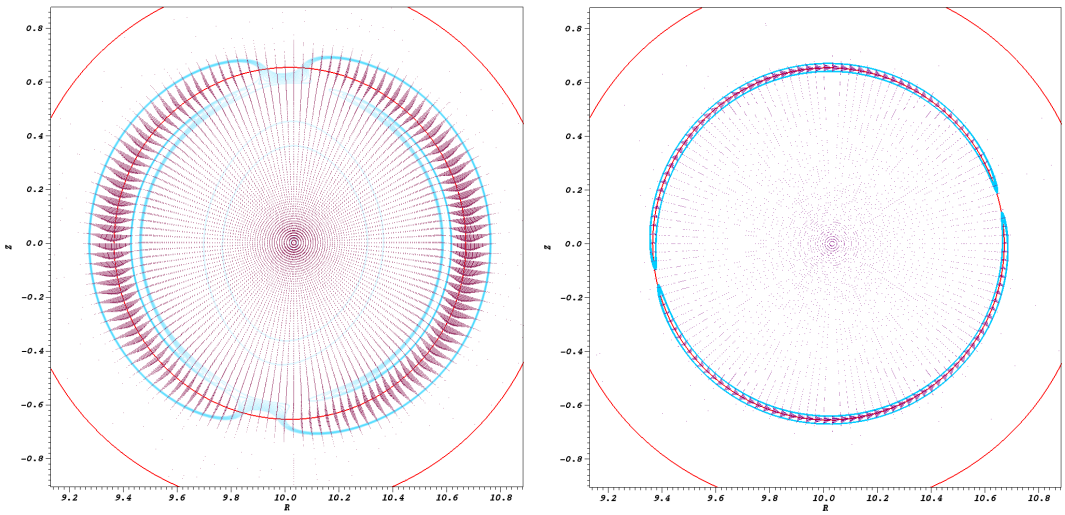

Figure 5: Kink structure comparison for $S = 10^5$ (left) and $S = 10^8$ (right). The width of the structures depends on the Reynolds Magnetic number. Going from 10^{-1} (left) to $3\ 10^{-2}$ (right)

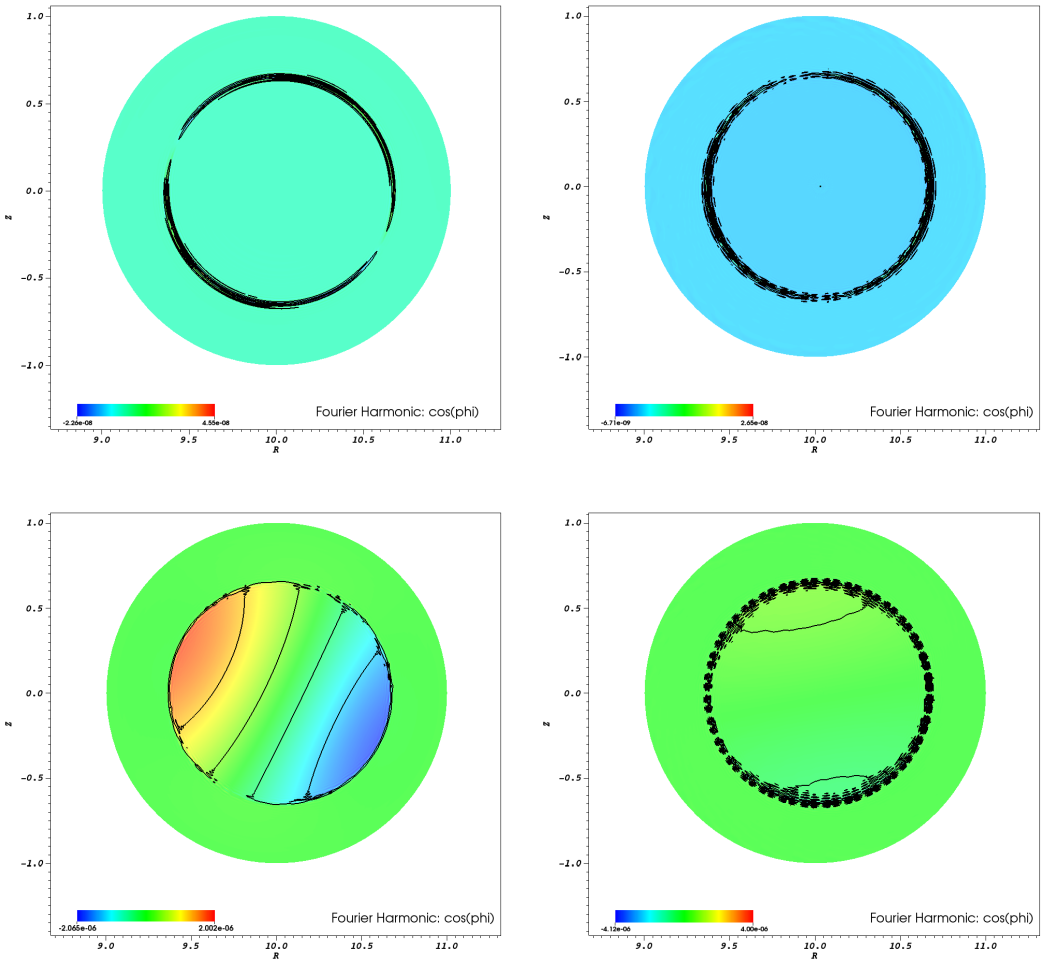

Figure 6: Effect of the VMS-Stabilization on the spurious waves. For the fluctuations of the toroidal velocity (top) and the fluctuations of density (bottom). Left figures are results obtained with VMS-stabilization and right figures are obtained without numerical stabilization. Mesh of 32 poloidal elements, 1280 poloidal vertices and 3 toroidal harmonics. The total number of degrees of freedom is 122880. Implicit Crank-Nicholson scheme a normalized time step of $\delta t = 400$, $S = 10^8$.

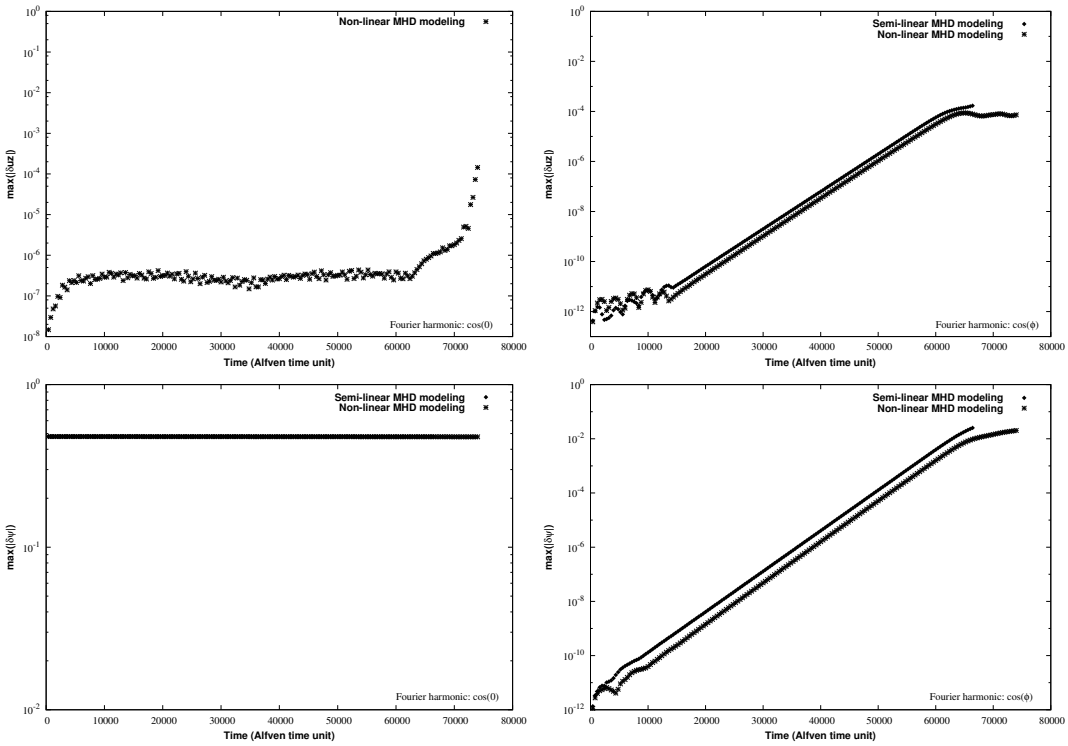

Figure 7: Dynamic of the Kink Mode, for a magnetic Reynolds of $S = 10^8$, using Quasi-linear modeling (where the mode zero is assumed constant) and fully nonlinear modeling. Evolution of z-component of the velocity $\boldsymbol{v}_z$ (top) and ϕ-component of the potential vector ψ (bottom) for the mode zero (left) and the mode one (right).

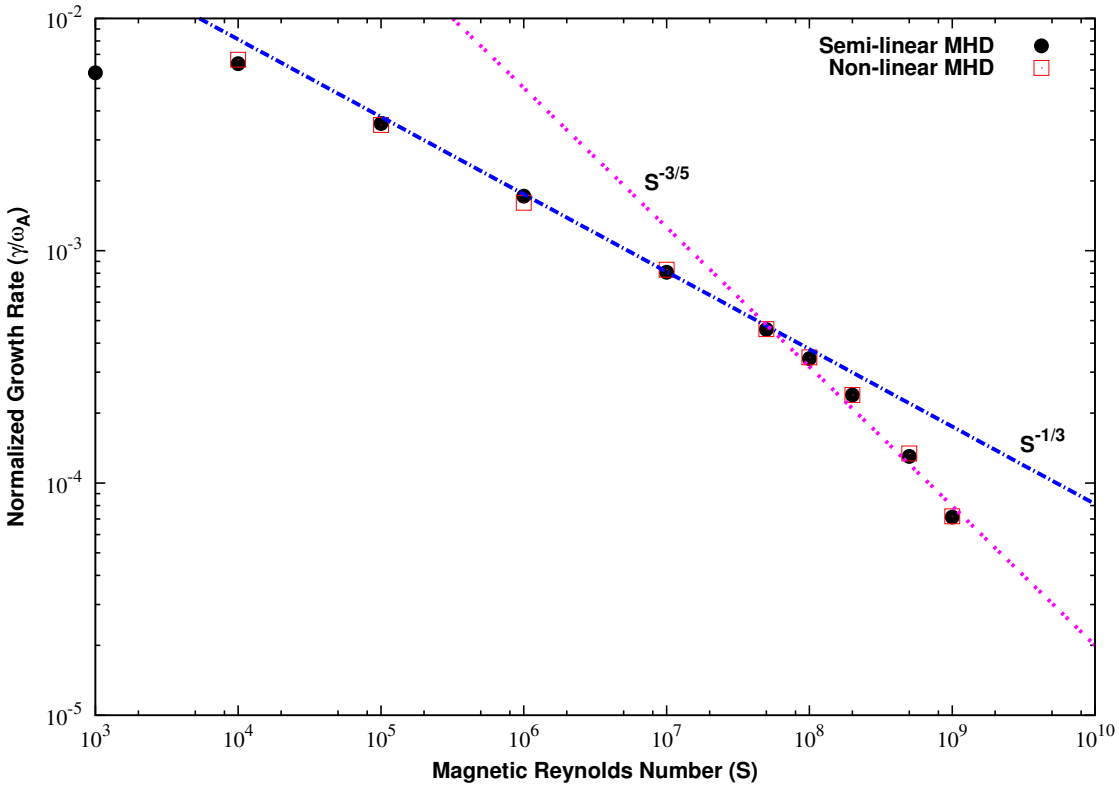

Figure 8: Computed Growth rate for the internal kink mode as function of the magnetic Reynolds number (S). The expected growth rate is [23], asymptotically, $S^{-1/3}$ for S smaller than a threshold and $S^{-3/5}$ for larger S.

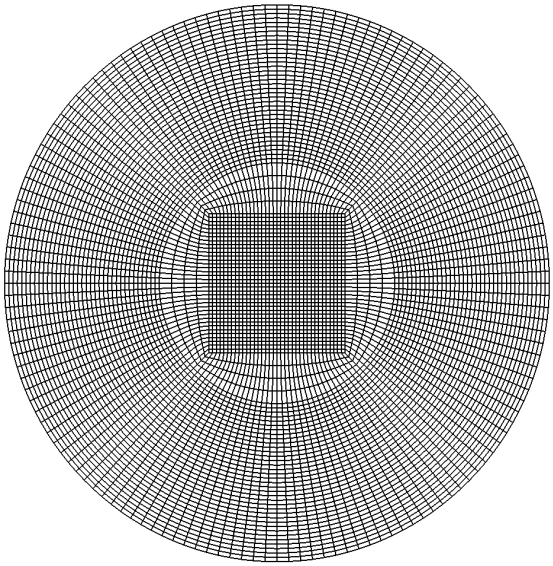

Figure 9: Mesh used for the first test case. The square part is constructed with $n_R = n_Z = 36$ and the external part $n_\vartheta = 144$ and $n_R = 40$ resulting in a total of 7056 elements

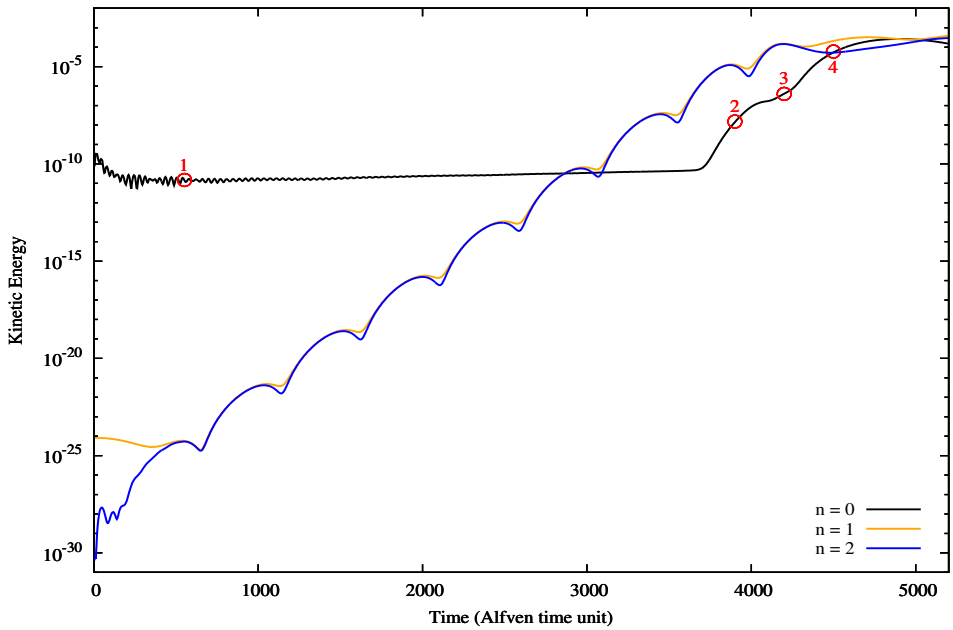

Figure 10: Evolution of the kinetic energy for the velocity associated to the toroidal functions $\cos(0 * \phi)$, $\cos(\phi)$ and $\sin(\phi)$, respectively associated to $(n = 0)$, $(n = 1)$ and $(n = 2)$.

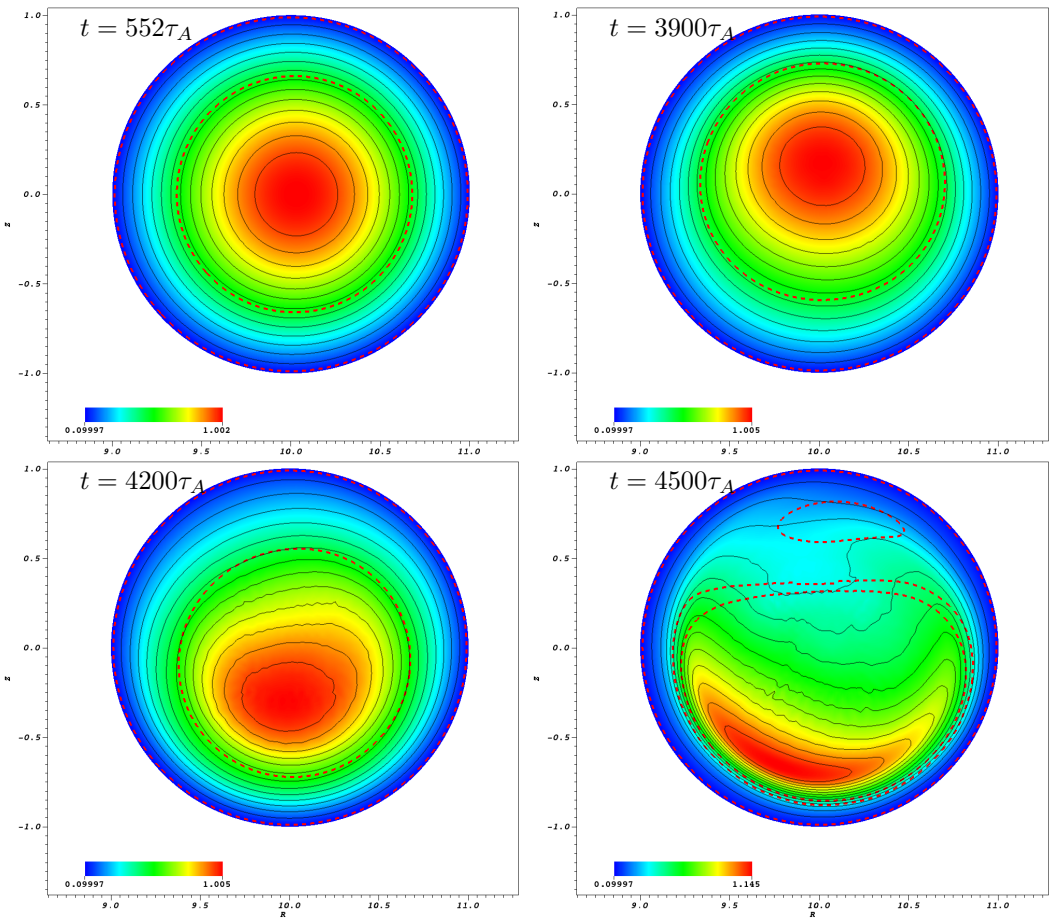

Figure 11: Evolution of the density profiles during the motion of the plasma column. 2D plot of the poloidal plane located at $\phi = 0$ for the times $t = 552\tau_A$ (top-left), $t = 3900\tau_A$ (top-right), $t = 4200\tau_A$ (bottom-left) and $t = 4500\tau_A$ (bottom-right)
, where τ_A is the characteristic Alfvén time. Dotted lines, far from the boundary, are the position of the rational mode surface $q = 1$.

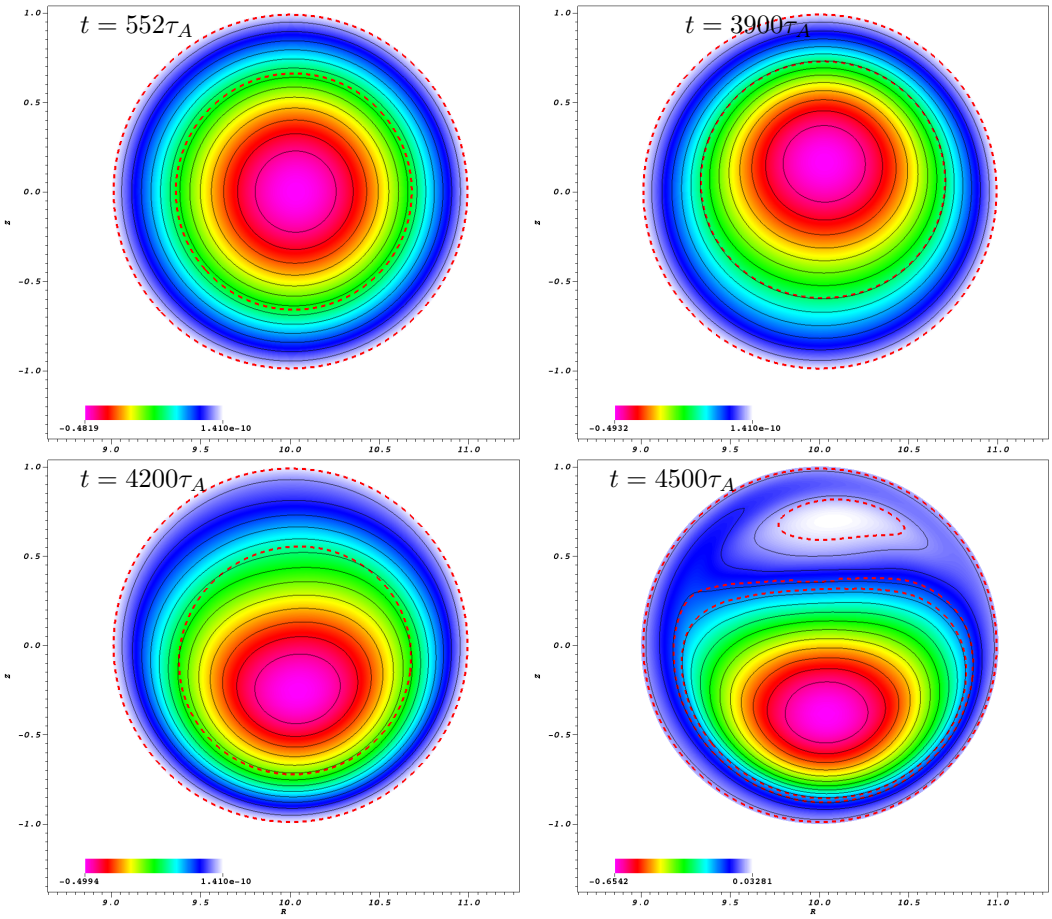

Figure 12: Evolution of the Magnetic flux. Dotted lines, far from the boundary, are the position of the rational mode surface $q = 1$.

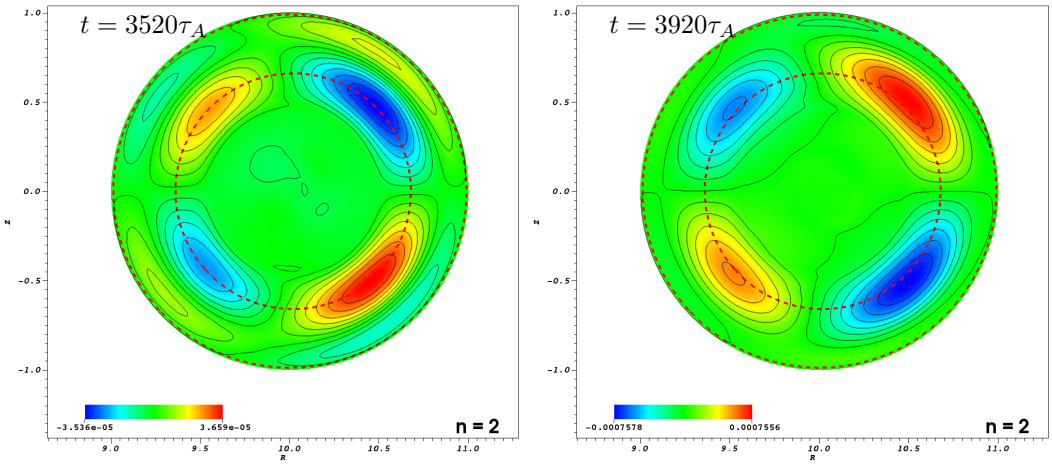

Figure 13: Radial velocity $\boldsymbol{v}_{\mathrm{R}}$ contours associated to the $sin(\phi)$ mode ($n = 2$). Evolution during the linear growth,, on the plane $\phi = 0$: $t = 3520\tau_A$ and $t = 3920\tau_A$.

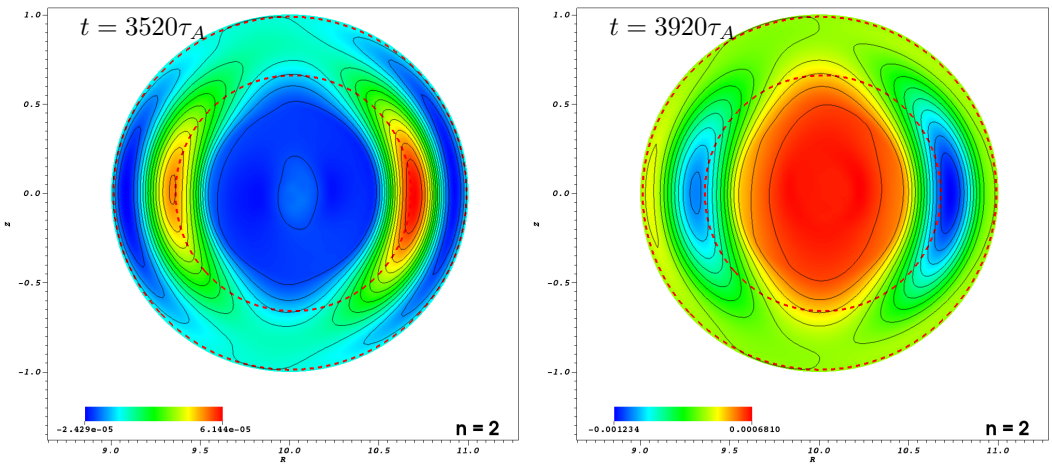

Figure 14: Vertical velocity $\boldsymbol{v}_{\mathrm{Z}}$ contours associated to the $sin(\phi)$ mode ($n = 2$). Evolution during the linear growth, on the plane $\phi = 0$: $t = 3520\tau_A$ and $t = 3920\tau_A$.

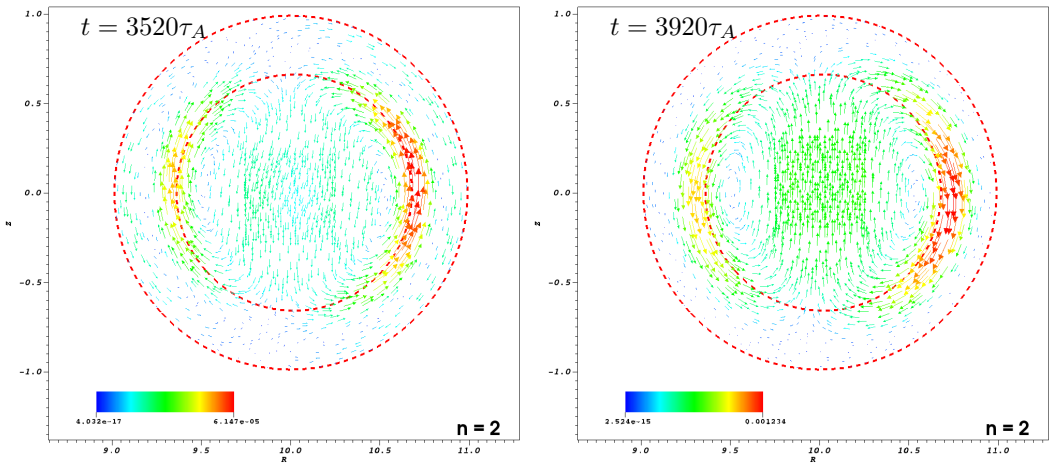

Figure 15: Velocity field associated to the $sin(\phi)$ mode ($n = 2$). Evolution, during the linear growth, on the plane $\phi = 0$: $t = 3520\tau_A$ and $t = 3920\tau_A$.

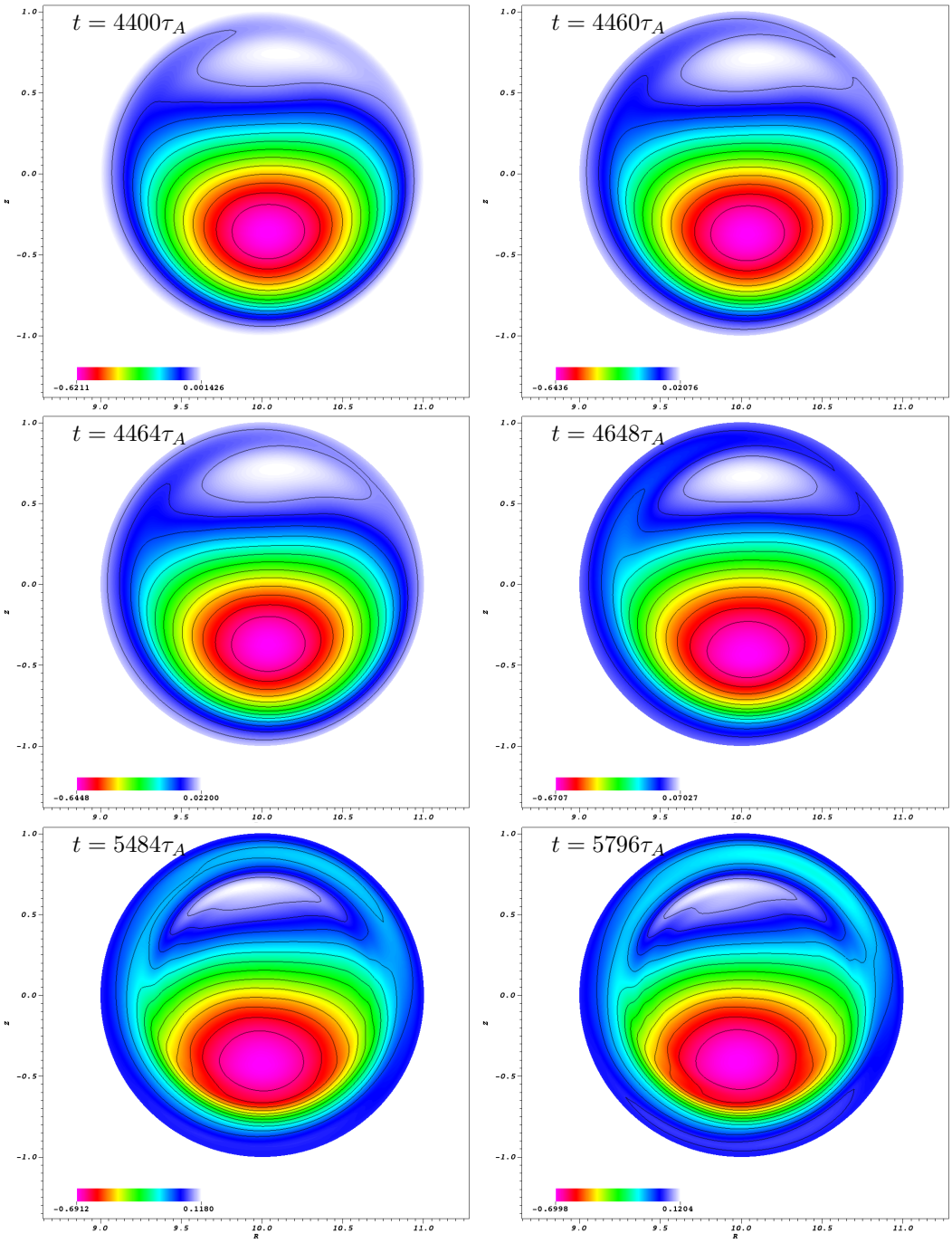

Figure 16: Reconnection of the magnetic flux surfaces ψ

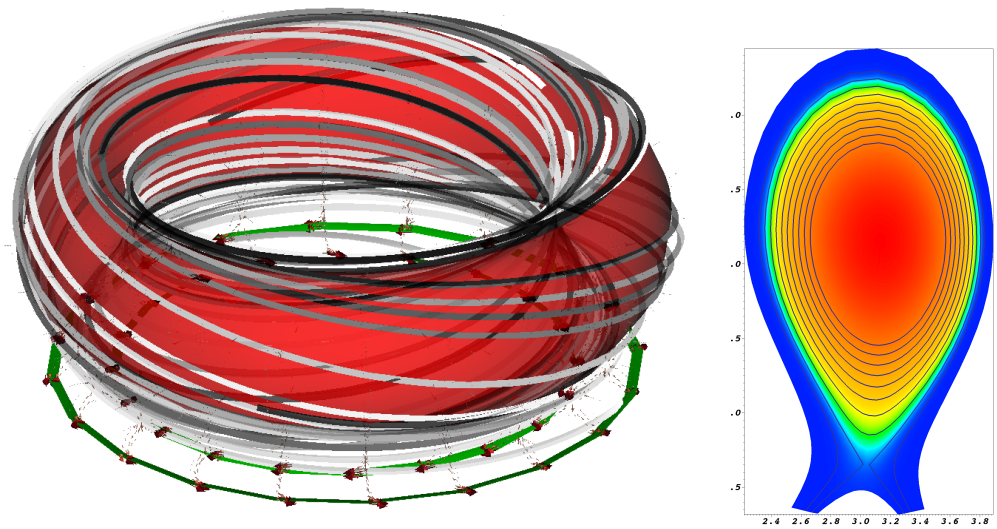

Figure 17: 3D Magnetic field lines, plasma density and poloidal velocity field near the divertor.

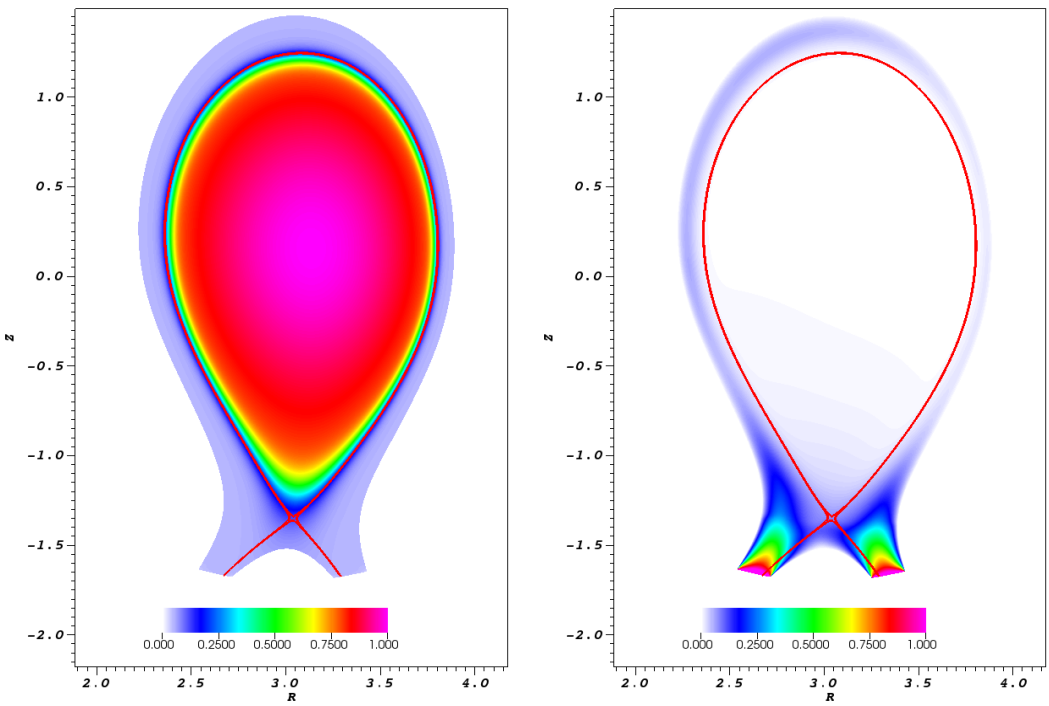

Figure 18: Density (left) and velocity (right) profiles at $t = 10$

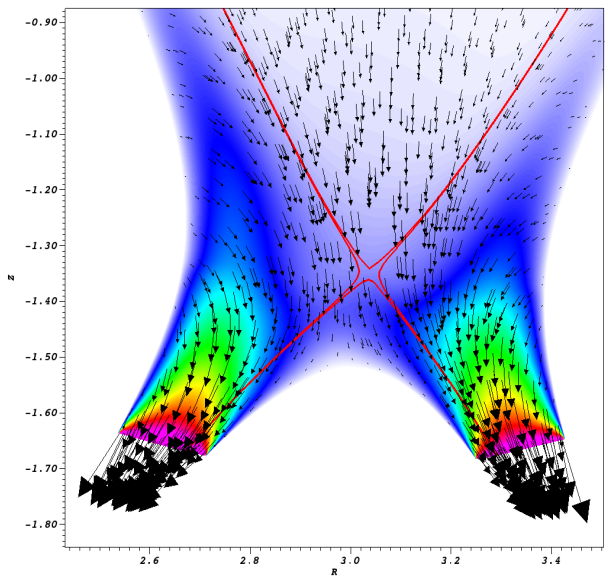

Figure 19: Velocity profile close to the divertor plates at $t = 10$

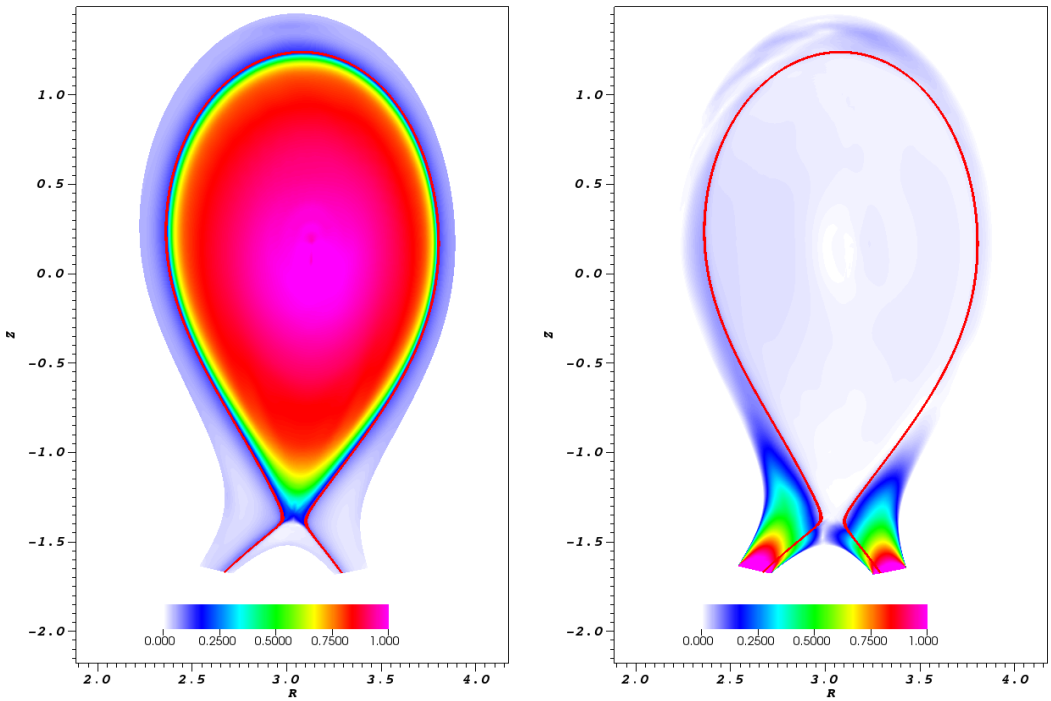

Figure 20: Density (left) and velocity (right) profiles at $t \approx 220$

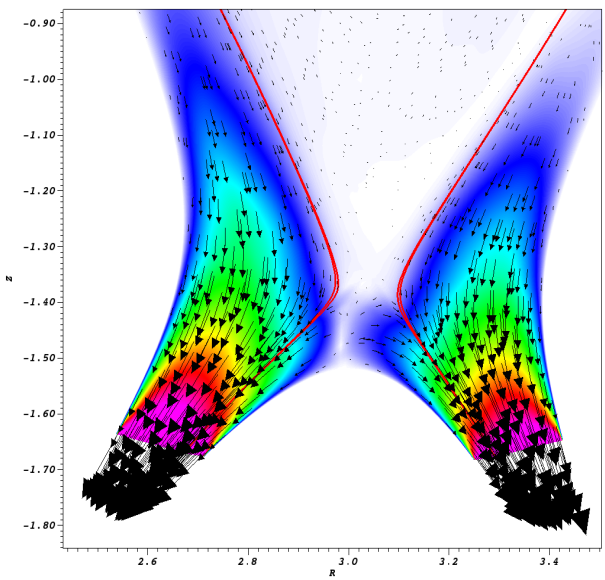

Figure 21: Velocity profile close to the divertor plates at $t \approx 220$

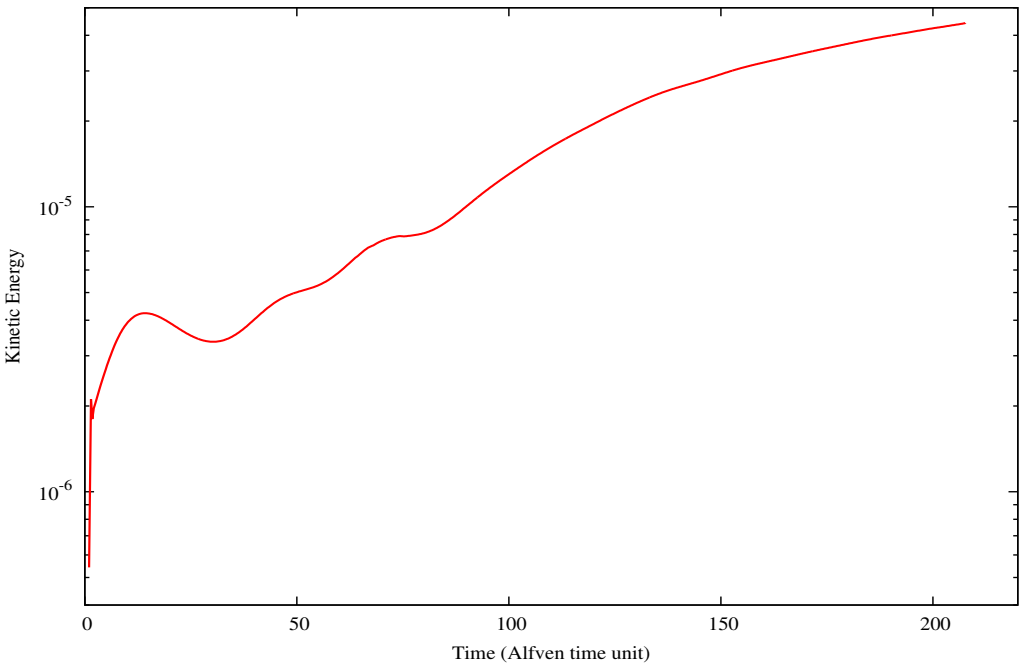

Figure 22: Evolution of the kinetic energy showing that, even though the steady-state has not been reached yet, the energy growth rate is decreasing as the time passes

RESEARCH CENTRE
SOPHIA ANTIPOLIS – MÉDITERRANÉE

2004 route des Lucioles - BP 93
06902 Sophia Antipolis Cedex

Publisher
Inria
Domaine de Voluceau - Rocquencourt
BP 105 - 78153 Le Chesnay Cedex
inria.fr

ISSN 0249-6399